Mechanical Properties of Small-Scale Sputtered Metallic Glasses

Thesis by

Anthony Herman Fu-Hao Kwong

In Partial Fulfillment of the Requirements
for the Degree of
Doctor of Philosophy

California Institute of Technology
Pasadena, California

Defended May 28, 2020

Anthony Herman Fu-Hao Kwong

ORCID: 0000-0001-6389-1443

Acknowledgements

I am very humbled and grateful to have had such a wonderful opportunity to pursue my PhD degree at Caltech. Throughout this journey, I have been very fortunate to have the support and guidance from my adviser Professor Julia Greer. I am sincerely grateful for all the knowledge, advice, encouragement and patience she has given me. She is an inspiring, caring and empathetic mentor whose energetic personality makes our group a fun and supportive environment to be in. I also admire her passion for outreach and giving back to the community even though she juggles a busy work and family life. Overall, I am honored that I could be a part of the Greer group and I am lucky to be able to work with such an amazing adviser.

I am also appreciative to all of the Caltech faculty who I have had the pleasure of taking courses with. Thank you to all the committee members who were on my candidacy exam and gave me many insightful comments that guided my research. Finally, many thanks to my thesis defense committee Professor Faber, Professor Johnson, and Professor Falson for your time and commitment.

To the Greer group family past and present, thanks for all the happy memories and the personal and academic support. Thanks to Rachel Liontas and David Chen for introducing me to the amazing world of metallic glasses. Thanks to Zachary Aitken for his mentorship and for his help with MD simulations. Thanks to the nanomechanics subgroup (Jane Zhang, Rebecca Gallivan, Amanda Mattson, Miranda Schwacke, Adenike Giwa, Brage Snartland, and Anette Hagan) for all the advice and thoughtful discussions. Thanks to my officemates (Kai Narita, Luiza Elliot, and Jane Zhang) for all the fun and laughter. You have rekindled my interest in playing board games and escape rooms! To all the KNI staff (Matthew Sullivan Hunt, Guy DeRose, Melissa Melendes, Bert Mendoza, Nathan Lee, Alex Wertheim, Tiffany Kimoto, Jennifer Palmer), thanks for being an amazing resource and

teaching me all the lithography, wet/dry etching, deposition, microscopy and characterization techniques.

To the SMHS students (Alex Ko, Wesley Huang, Anna Zhao, Jia Hu, Nathaniel Woo, Zhuoxi Chen, and John Chon) that I mentored, I hope you enjoyed the STEM program as much as I did. I admire your dedication to join me at lab at odd hours and to work with me through all the experimental troubleshooting. It was really rewarding for me to see your excited expressions whenever I introduced a new tool or technique. I wish you all the best in your undergraduate careers. I know you will all go on to achieve amazing things!

Finally, I am very lucky to have the support and encouragement from my family. My parents have been through ups and downs and they have inspired me with their resilience and persistence to never give up. Thank you to my girlfriend Kewei for all the happy and fun times together. Your positive and cheerful attitude always brightens my day. Thank you for believing in me and encouraging me through this amazing journey!

Abstract

Sputtered metallic glasses (MGs) represent a unique class of materials because their nonperiodic arrangements are far from equilibrium. This microstructure gives rise to their exceptional mechanical properties; for example, experiments and simulations on the deformation of small-scale sputtered Zr-based MGs demonstrate their exceptional compressive and tensile strengths in excess of 1 GPa and exceptional tensile ductility of ~150%[1].

We report a new property that emerges in sputtered MGs: age-induced strengthening. We measured the compressive strengths of cylindrical pillars with diameters between 300 nm to 1.1 μm, which were carved from a 5 μm-thick sputtered Zr–Ni–Al thin film that was aged in a nitrogen environment for three years. Nanomechanical experiments revealed that the aged samples had a stiffness of 91 ± 4 GPa and a yield strength of 2.7 ± 0.2 GPa for all cylinder sizes, which represents a nearly 43% increase in yield strength and a 31% increase in the elastic modulus compared to equivalently sized as-sputtered samples. We also observed nano-sized induced failure suppression: samples with diameters below 600 nm deformed smoothly and noncatastrophically. Those with larger diameters deformed via a series of observable and detectable shear bands that propagated to the surfaces. Molecular dynamics (MD) simulations of uniaxial compression of chemically equivalent Zr–Ni–Al MG nanowires revealed that the underlying physics of enhanced strengths involves the evolution of local disorder that can be quantified in the number of fivefold atomic bonds. The average amount of fivefold bonding increased systematically with energetic relaxation and the maximum compressive stress. Dynamic mechanical analysis (DMA) revealed the presence of hydrides within the MG. Hydrogen diffusion into the host matrix resulted in an increase in the local volume such that more–mobile atoms (i.e., Ni and Al) can redistribute and relax into a more–energetically favorable configuration.

Experiments and simulations in this work demonstrate that sputtered MGs strength by 43% when solely aged for three years, i.e., without any accompanying annealing or mechanical treatment, which originates from atomic-level microstructural relaxation in these materials. This provides a useful foundation for simple design of advanced materials whose mechanical properties can be predicted and prescribed a priori using physical principles of atomic-level relaxation.

Published Content

(1) Q. Li, S. Xue, J. Wang, S. Shao, **A. Kwong**, A. Giwa, Z. Fan, Y. Liu, Z. Qi, J. Ding, H. Wang, J.R. Greer, H. Wang, X. Zhang. "High-Strength Nanotwinned Al Alloys with 9R Phase" *Advanced Materials* 30, 1704629 (2018). DOI: 10.1002/adma.201704629
Contributions: fabricated cylindrical pillars via SEM/FIB, performed uniaxial compression experiments and analyzed data.

(2) **A. Kwong**, Z. Aitken, M. Schwacke, Y.W. Zhang, J.R. Greer. 'Aging is not just for wine: Substantial strength enhancement and relaxation in sputtered Zr–Ni–Al metallic glasses through room–temperature aging'. *(Manuscript in Preparation)*

Contributions: A.K. sputtered the metallic glass, fabricated pillars via SEM/FIB, characterized samples using SEM, FIB, EDS, performed uniaxial compression experiments, analyzed data and participated in the writing of the manuscript.

Table of Contents

List of Figures

List of Tables

Chapter 1. Introduction and Background

1.1. What is a metallic glass?

Metallic glasses (MGs) consist of atoms which are metallically bonded, like metals, but have an amorphous structure similar to that of oxide glasses. They were first developed by Pol Duwez in 1960 at the California Institute of Technology where a glassy ribbon of Au-25 at.% Si alloy was fabricated by rapidly cooling the molten metal at rates approaching a million degrees per second[2]. Unlike crystalline metals, they lack long range systematic atomic arrangements, crystal defects, grain boundaries, and phase changes[3–6].

As a result, this class of material has very unique and advantageous physical, chemical and mechanical properties. For example, the lack of long range systematic atomic arrangements results in a material that exhibits low mechanical dissipation and high elastic strain limits[3,7]. Under mechanical deformation, the material absorbs less energy from damping and responds more elastically. Typically, MGs can yield at ~2% strains[7], while crystalline metals yield at an order of magnitude lower ~ 0.2% strain[3] (as shown in figure 1.1). The absence of crystal defects allows MGs to have exceptional mechanical properties such as high hardness and strength in tension and compression[8,9]. For example, Co-based MGs can reach up to 6 GPa in yield strengths[10]. MGs also do not exhibit grain boundaries and thus, have soft magnetic properties and excellent corrosion and wear resistance[11–13]. Studies on iron-based MGs have demonstrated low magnetic permeability, low loss and high saturation induction[14–16].

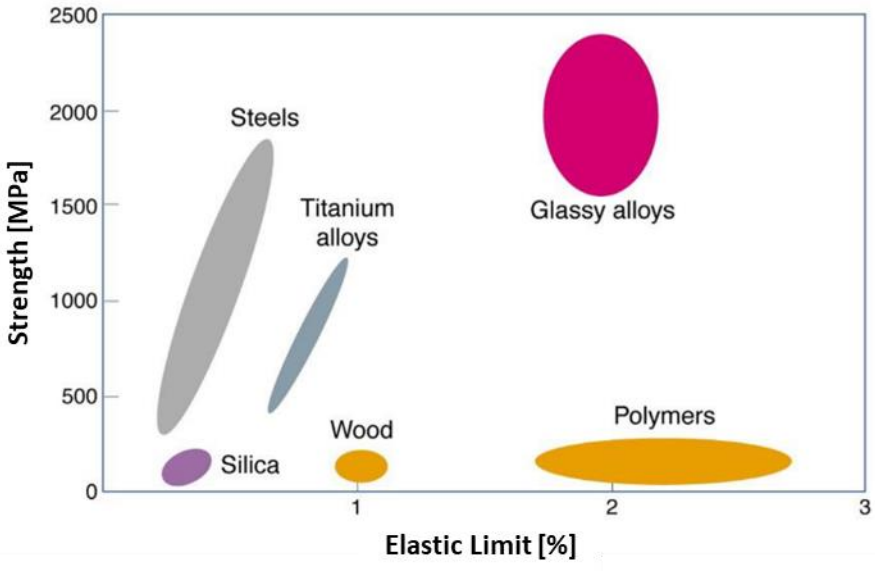

Figure 1.1. The strength versus elastic limit for various engineering materials. Comparatively, MGs exhibit one of the highest strengths and elastic strain limits [6]

With all of these exceptional properties, MGs are an attractive material for a variety of applications (i.e., structural, biomedical, etc.). The development of bulk glass formers and processing techniques such as thermoplastic molding (shown in figure 1.2(a)) has increased the feasibility of utilizing MGs in structural applications[17,18]. In thermoplastic molding, the MG is heated to a processing temperature ($T_{process}$) that is between the glass transition temperature (T_g) and the crystallization temperature (T_x). Then, it is forced into a mold and immediately quenched down to a temperature that is below T_g. The quenching rate has to be fast enough such that the processing time ($t_{process}$) is less than the time for crystallization (t_{cryst}). Applications of MGs include springs (shown in figure 1.2 (b)), cutting blades, gears, sports equipment (shown in figure 1.2 (c)), jewelry, and watch cases[3,6,17–20]. Besides macro–scale applications, MGs can be integrated into micro and nanoelectromechanical systems (MEMs/NEMs) devices (i.e., resonators and actuators)[21–23]. These devices can benefit from MG's isotropic properties, low internal friction[24,25], and lack of internal length scales. Biomedical applications can utilize MG's high mechanical property, excellent corrosion and wear resistance for

high quality biocompatible implants. Extensive research has been focused on Ti–based, Zr–based, and Fe–based MG alloys due to their biocompatibility[26–28].

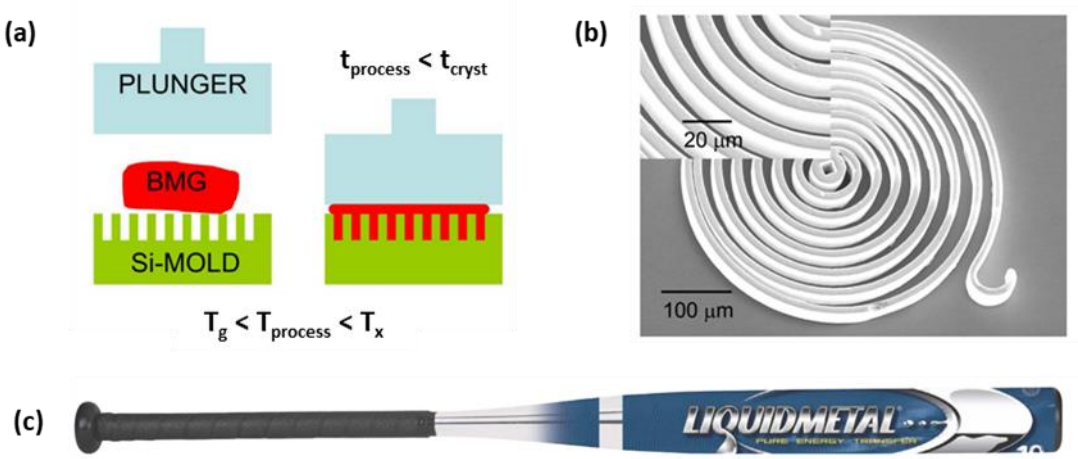

Figure 1.2. (a) Schematic of thermoplastic molding of bulk MG [23]; (b) SEM image of a coil-shaped spring made from bulk MGs; [23] (c) Baseball bat featuring Liquidmetal Technology's metallic glass[6]

1.2. Processing metallic glass

1.2.1 Bulk metallic glass

Bulk MGs are formed by cooling the liquid phase faster than the critical cooling rate (R_c) to prevent crystallization. Below the liquidus temperature, the cooling path bypasses the crystallization nose in the time-temperature-transition (TTT) diagram and dynamic equilibrium is achieved within the supercooled liquid where the atomic relaxations are fast enough to accommodate the decrease in temperature (i.e., path A in figure 1.3 (a)). This continues until the T_g is reached where the supercooled liquid becomes a solid glass. On the other hand, crystallization will occur if the cooling rate is less than R_c. In this case, the supercooled liquid crosses over into the crystallization nose in the TTT diagram, as shown in path B of figure 1.3 (a), where the driving force for nucleation and the growth of crystallites dominates.

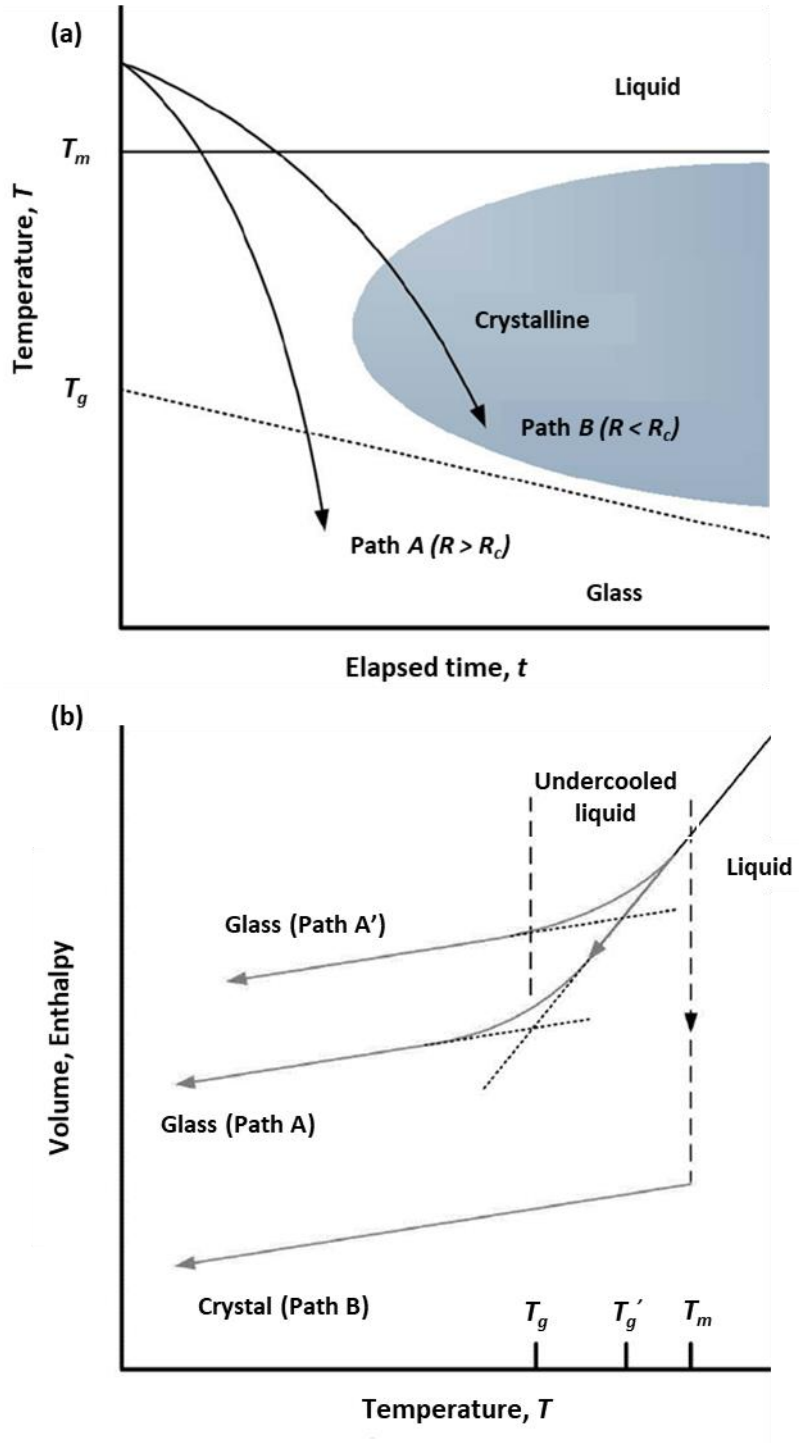

Figure 1.3. Dependence of cooling rate on the solidification paths. (a) Schematic TTT diagram with two solidification paths: path A-glass formation where the cooling rate (R) > critical cooling rate (R_c); and path B-crystallization where $R < R_c$. (b) Volume and enthalpy vs. temperature for glass formation (path A) and crystallization (path B). The higher cooling rate (path A') results in a glassy solid with higher T_g, volume and enthalpy compared to a glassy solid formed at a lower cooling rate (path A).

In figure 1.3 (b), a plot of the volume and enthalpy versus temperature shows that the transition from the liquid to solid phase varies substantially based on the cooling rates. For crystalline solids, there is a sharp drop from the high-energy liquid to the low-energy ordered phase. While for glassy solids, the transition from the liquid to the glassy phase is much smoother. Furthermore, the enthalpy of the glassy state is dependent on the respective cooling rates. Conventional melt or solid quenching techniques utilize cooling rates from 10^3 to 10^8 K/s [6]. A faster cooled glass exhibits higher enthalpy, more "liquid-like" microstructures and have higher T_g. In contrast, a slower cooled glass exhibits lower enthalpy, more "solid-like" microstructures and have lower T_g.

The high cooling rates limit the critical casting thickness of bulk MGs. Thus, substantial efforts have been focused on minimizing the critical cooling rate so that larger casting thicknesses can be achieved. Inoue proposed three empirical rules to improve the glass-forming ability of bulk MG[29]:

1. Selecting a MG composition with at least three elements that lies near a deep eutectic;
2. Large atomic size mismatches (> 12%);
3. Large negative enthalpies of mixing.

For example, the thermodynamics and glass forming ability of Zr-Ni-Al MG have been widely studied. Experimentally, the eutectic composition can be determined by performing differential thermal analysis (DTA) experiments to understand the alloy's melting and solidification behaviors. Figure 1.4 is a ternary plot of the liquidus temperature as a function of composition. Jing et al. showed that compositions around $Zr_{60}Ni_{21}Al_{19}$ exhibited the best glass forming ability due to their large critical casting diameter[30]. The empirical atomic radii of Zr, Ni and Al have been determined to be 155 pm, 135 pm, and 125 pm, respectively[31]. Thus, the ratio of the radii R_{Zr}/R_{Ni}, R_{Zr}/R_{Al}, R_{Ni}/R_{Al} are 1.15, 1.24, and 1.08, respectively. These elements have large atomic size mismatches, which destabilize the

competing solid solution phase and enhance the glass forming ability[32]. The calculated enthalpy of mixing for $Zr_{60}Ni_{25}Al_{15}$ is -6.6 kJ/mol, which is considered to be one of the most negative enthalpies for Zr-based compositions. Comparatively, $Zr_{10}Ni_{25}Al_{65}$ has an enthalpy of mixing of -1.3 kJ/mol. Therefore, compositions around $Zr_{60}Ni_{25}Al_{15}$ are suitable for the formation of a stable MG.

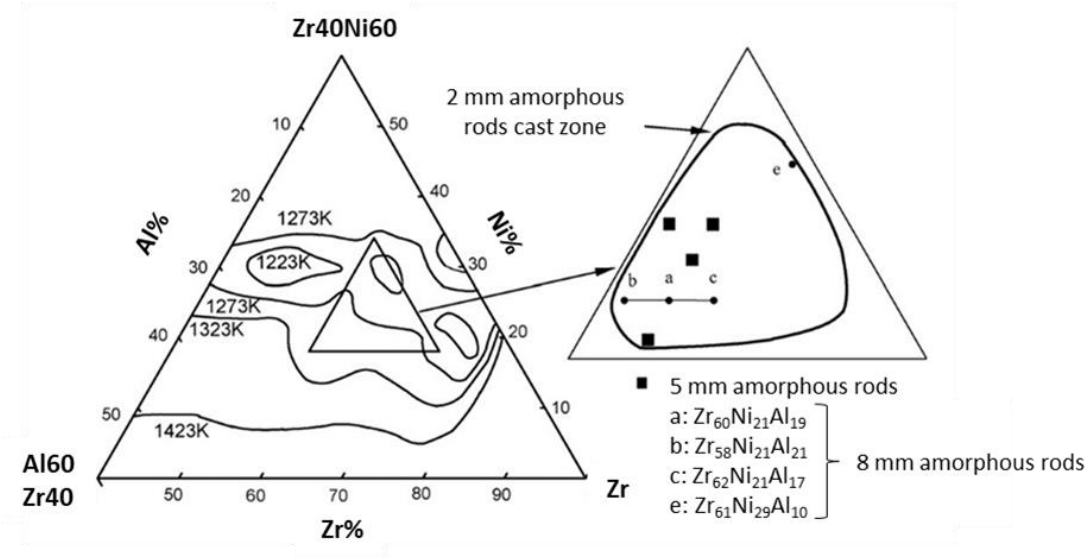

Figure 1.4. Ternary plot of the liquidus temperature for Zr-Ni-Al as a function of composition. Compositions near $Zr_{60}Ni_{21}Al_{19}$ exhibit the best glass forming ability and have the largest critical casting diameters[30].

1.2.2. Thin-film metallic glass (TFMG)

Besides rapid quenching, MGs can also be fabricated into thin films via evaporation, electrodeposition or sputtering. In particular, sputtering is a physical vapor deposition technique that has been shown to produce glassy metals with analogous microstructure to that of a fast cooled bulk MG with cooling rates on the order of 10^{12} K/s [33]. Sputtered TFMGs retain all the exceptional properties of bulk MGs. Compared to bulk MGs, sputtered TFMGs can use cheaper elements because the fabrication process is less dependent on the thermodynamics of the materials (i.e., cooling rate is not an issue)[33]. Furthermore, the sample size (i.e., thickness) can be easily and accurately controlled by adjusting the deposition time.

The development of TFMGs has opened up many new applications that were previously unachievable by bulk MGs. The high elastic strain limit and low mechanical dissipation, as well as the emergence of room-temperature ductility when reduced to nano-sized dimensions render them particularly useful in micro- and nano-scale devices, such as MEMs/NEMs devices[21,22,34,35].

1.2.3. Effects of processing on microstructure

Fabrication processing parameters have significant impact on the MG's microstructure. Increasing the quench rate in bulk MG results in a MG with higher enthalpy and more-disorder/"liquid-like" microstructure[36]. Synchrotron XRD experiments on Zr-Cu-Ni-Al MG revealed that faster quench rates increased the number of Zr-Zr bonding, while the number of Zr-Cu bonding was reduced[37]. Pair distribution functions for the bulk (i.e., 10^6 K/s quench rate) and ultra–quenched (i.e., sputtered MG with an analogous quench rate of 10^9 K/s) samples are shown in figure 1.5. The first peak splits into two sub-peaks located at 2.80 Å and 3.15 Å and correspond to the Zr-Cu pairs and Zr-Zr pairs, respectively. The ultra-quenched sample exhibits the widest first peak, which suggests that the nearest–neighbor (NN) atomic packing is looser than in the bulk sample and is consistent with the higher fraction of longer Zr-Zr pairs.

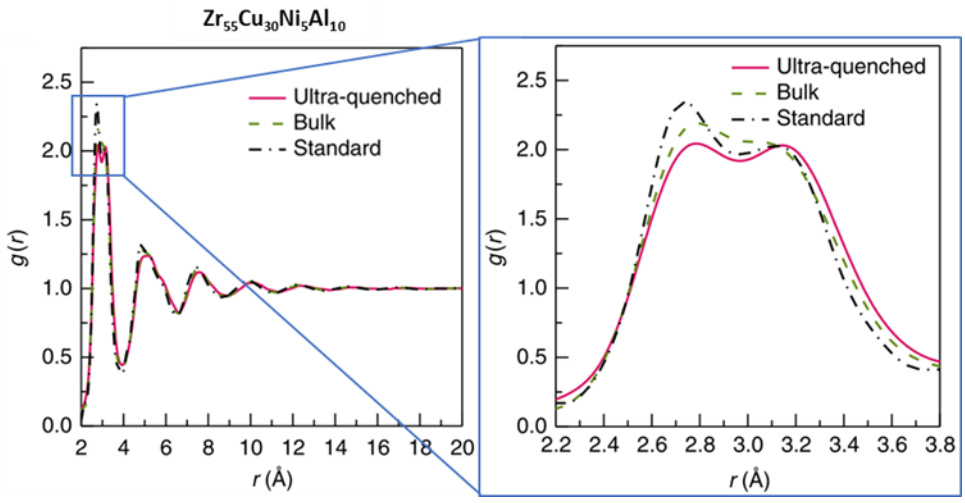

Figure 1.5. Pair distribution functions derived from synchrotron XRD experiments for Zr–Cu–Ni–Al. Zoomed-in view of the first peak reveals two sub-peaks that correspond to the Zr-Cu (2.80 Å) and Zr-Zr bonding (3.15 Å)[37].

In sputtering, varying the deposition power is another method of altering the MG microstructure [38]. Wei et al. sputtered Cu–Zr–Al thin films with powers ranging from 36–96 W [39]. The thickness of the thin film ranged from 0.584 μm (for the 36 W sample) to 1.282 μm (for the 96 W sample). XRD results, shown in figure 1.6, reveal that there are two broad peaks, which suggest a phase separation phenomenon. As the deposition power increases, the first peak (~32° for the 36 W sample) shifts towards larger angles while the second peak (~44° for the 36 W sample) shifts towards smaller angles. The shifting of the peaks could be caused by slight composition variations in the MG, which affects the short range order (SRO).

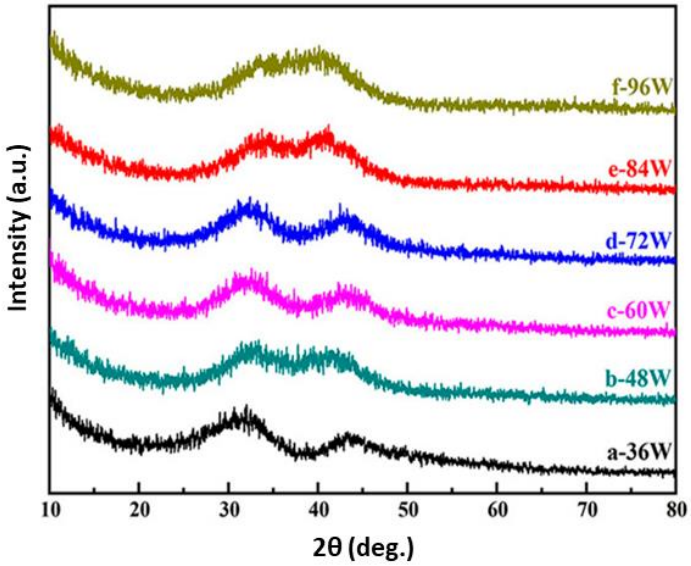

Figure 1.6. Grazing incidence XRD results for a Cu–Zr–Al TFMG deposited at various sputtering powers[39].

1.2.4. Effects of processing on mechanical properties

The relationships between processing–structure–properties are very connected. Studies on the effect of varying cooling rates on the mechanical properties (shown in figure 1.7 (a)) of Pd-based MGs reveal that as the cooling rate decreases, the hardness decreases, while ductility increases[40]. This is due to the lower density and SRO of the fast cooled glass. In sputtered Cu–Zr–Al thin films, increasing

the deposition power increased the hardness from 7.77 to 8.17 GPa (shown in figure 1.7 (b)) and is attributed to the more–homogenous and densely packed microstructure in the sample that was deposited using higher power[39]. The Young's modulus is independent of deposition power and remained uniform at around 140 GPa.

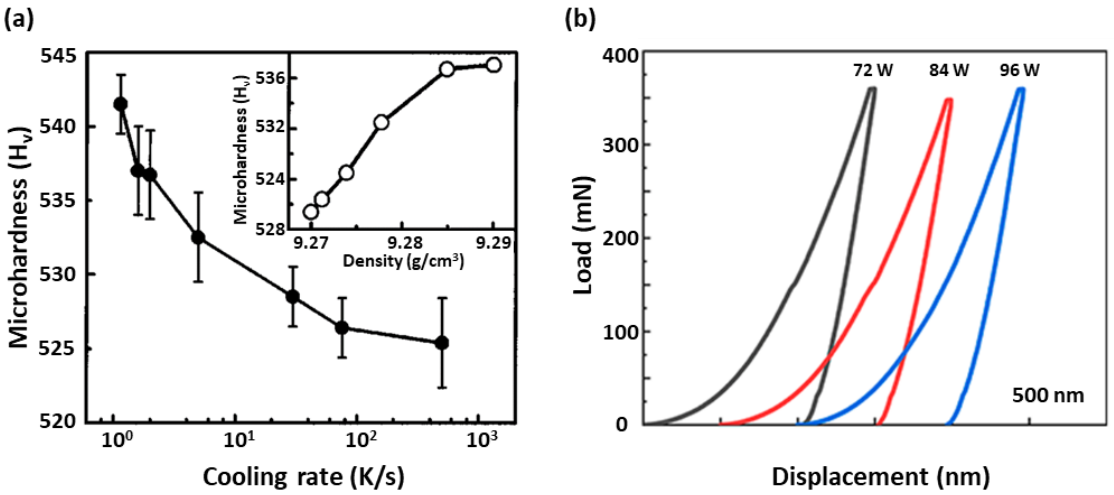

Figure 1.7. Effect of processing on the mechanical properties of MGs. (a) Effect of varying cooling rates on the microhardness and density of Pd-based metallic glass. Higher cooling rates results in lower microhardness and density[40]. (b) Nanoindentation load-displacement curves for sputtered Cu-Zr-Al at various deposition power[39].

1.3. Post-processing techniques

1.3.1. Relaxation

Besides varying the fabrication methods and parameters, there are numerous post–processing techniques that can tune the microstructure and affect the mechanical properties of MGs. All of these post–processing techniques can be categorized into two main effects on the microstructure: (1) relaxation, and (2) rejuvenation. Relaxation occurs when the stored enthalpy is reduced and the material densifies. As a result, the Young's modulus and yield strength increase; however, the ductility

decreases. Relaxation can be achieved through post–processing techniques such as thermal annealing below the glass transition temperature[36,41,42], cyclic loading[43–47] and hydrostatic pressure[48–51].

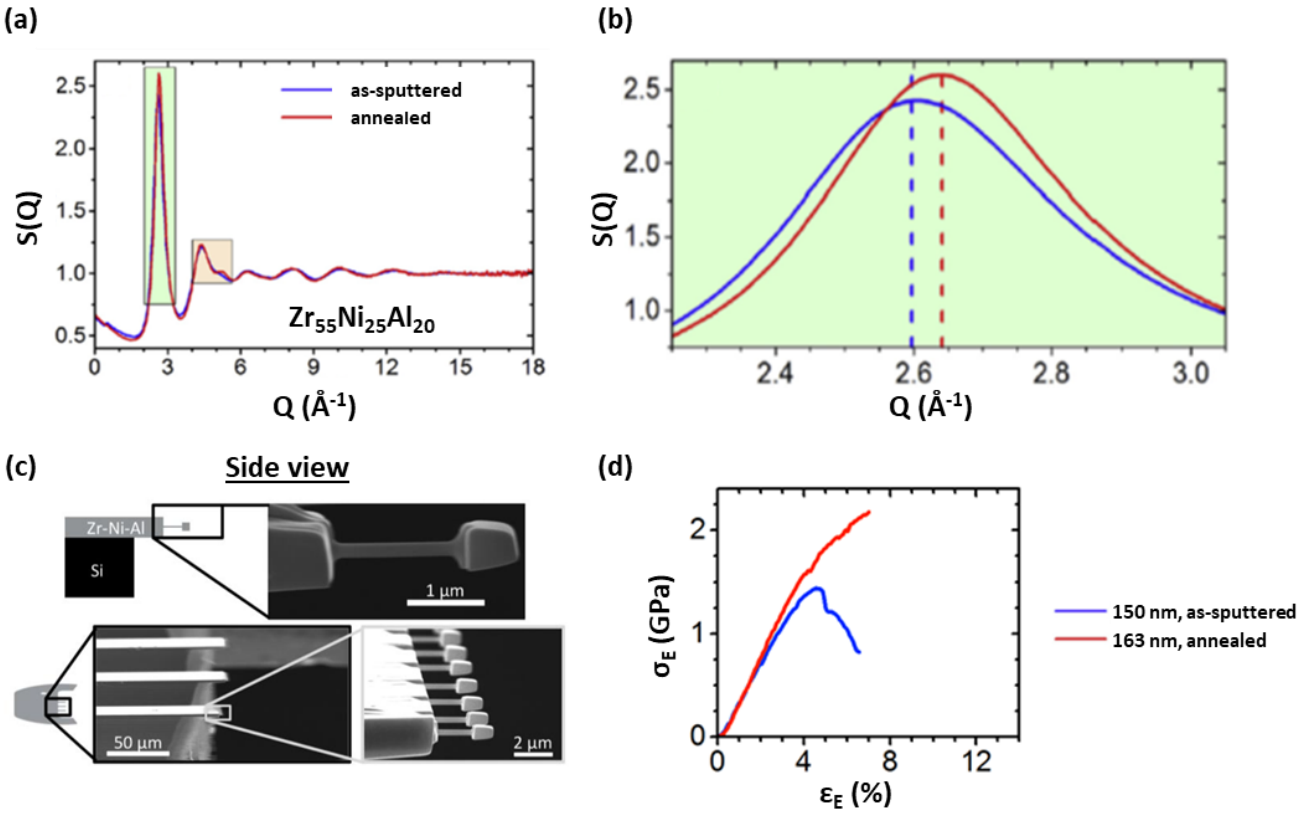

Figure 1.8. Effect of thermal annealing below T_g on the structure factor and mechanical properties. (a) Synchrotron XRD results for as-sputtered (blue) and annealed (red) Zr–Ni–Al metallic glass. (b) Zoomed–in region of the principle peak demonstrates that annealed state has a denser atomic packing compared to the as-sputtered state. (c) Side view of the nano-tensile specimens. (d) Uniaxial tensile experiments reveal that annealing increased both Young's modulus and yield strength.[1]

Liontas et al. performed synchrotron XRD and nano-tensile experiments to determine the structure factor and mechanical properties of sputtered Zr–Ni–Al in its as–sputtered state and after thermal annealing at 625 K for 24 hours[1]. XRD and TEM revealed that annealing did not result in any crystalline ordering within the sample[1]. From the synchrotron XRD experiments, a plot of the structure function, S(Q), as a function of the scattering vector, Q, is shown in figure 1.8 (a) and (b). Q is inversely proportional to the average atomic spacing. Thus, larger values of Q would

correspond to smaller average atomic spacing. For the first peak, Q increased from 2.597 Å, in the as-sputtered sample, to 2.641 Å, in the annealed sample[1]. This demonstrates that the annealed state has a denser atomic packing compared to the as-sputtered state. Uniaxial nano-tensile experiments were performed to understand the mechanical properties and behavior as a result of thermal annealing. A side view of the nano-tensile specimen is shown in figure 1.8 (c). Stress-strain curves of the as-sputtered (blue) and the annealed (red) reveal that the Young's modulus and yield strength increased by 17% (from as-sputtered: 38 GPa to annealed: 44 GPa) and 20% (from as-sputtered: 1.26 GPa to annealed: 1.51 GPa), respectively. For the same nano-tensile diameter, annealing reduced the ductility of the sample and changed the deformation mechanism from necking to shear banding.

1.3.2. Rejuvenation

Rejuvenation is the inverse process of relaxation where both the stored enthalpy and the free volume of the MG increases[52–54]. As a result, the Young's modulus and yield strength decrease; however, the ductility improves. Rejuvenation can be achieved via various post–processing techniques such as irradiation by high–energy ions or neutrons[55–61], surface peening[62–69], cryogenic cycling[70], or high temperature annealing followed by rapid quenching[71,72].

1.4. Nanomechanical testing

1.4.1. Mechanical properties of small–scale metallic glass

Over the past decades, developments in fabrication, characterization and mechanical testing at the micro- and nano-scale have facilitated the growth of research in nanomechanics. At these small length scales, mechanical properties such as hardness, Young's modulus and yield strength can be measured via three main techniques: nanoindentation of thin films, compression and tension

experiments of micro- and nanopillars. Nanoindentation is relatively the simplest technique to quickly determine the hardness and Young's modulus of a material. However, the data is heavily influenced by large strain gradients and underlying substrate effects. Uniaxial pillar compression and tensile experiments can reveal the Young's modulus and yield strength of the material. It does not suffer from large strain gradients or underlying substrate effects. When performed in a scanning electron microscope (SEM), we can observe the deformation mechanism as the experiment occurs.

Mechanical properties at the micro– and nano–scale have demonstrated that the sample size can dramatically affect the material's mechanical properties and behavior. In crystalline metals, the "smaller is stronger" effect results in an order of magnitude increase in strength for samples with sub-micron dimensions. In MG, reducing sample sizes to nano-length scales can induce a brittle-to-ductile transition[73–78].

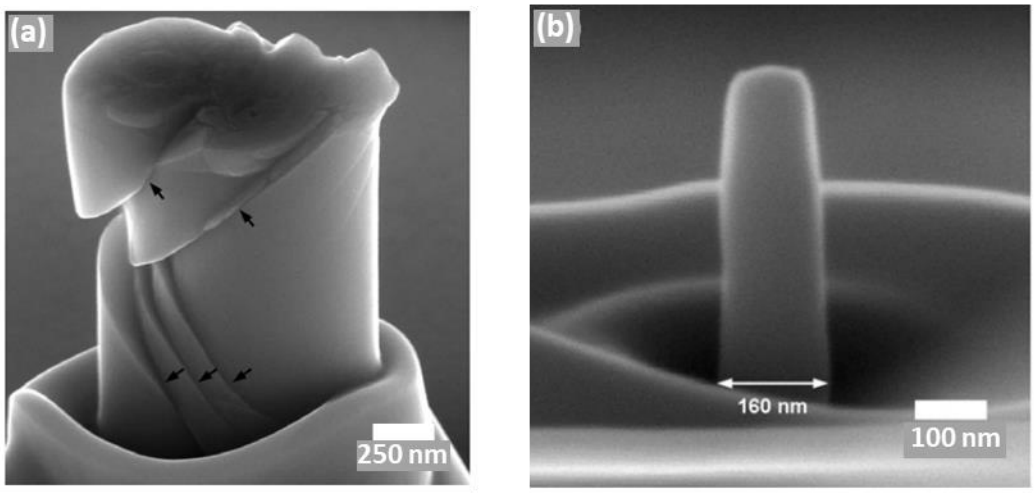

Figure 1.9. SEM images of Zr-Ti-Co-Be metallic glass pillars after compression. (a) 400 nm diameter pillar deforming by shear banding (arrows point toward the shear bands) and (b) a 100 nm diameter that deformed homogenously[79].

Jang et al. performed uniaxial pillar compressions on Zr-Ti-Co-Be MG with diameters ranging from 100 nm to 1.6μm[79]. They observed a transition in deformation mechanism from highly localized to homogeneous deformation at length scales of 100 nm (shown in figure 1.9). Furthermore, the yield

strength was size dependent down to 800 nm. Below 800 nm, the yield strength remained at its maximum value of 2.6 GPa. The increase in strength is due to a lower probability of having weak flaws in the smaller samples combined with the plastic deformation that occurred at these small length scales.

1.5. Overview of thesis

The objective of this thesis is to elucidate the effect of physical aging at room temperature on the atomic–level microstructure and mechanical properties of sputtered Zr–Ni–Al MG. In Chapter 2, the experimental methods will be discussed. In particular, the fabrication of micro- and nano-pillars, characterization techniques and the nanomechanical testing methods will be described in detail. Subsequently in Chapter 3, quasi-static uniaxial pillar compression experiments were performed on aged Zr-Ni-Al MG. The stress-strain curves of the aged and as-sputtered samples are analyzed to determine the Young's modulus and yield strength. Substantial enhancements in both mechanical properties are discovered. From these experimental observations, we employ MD simulations in Chapter 4 to reveal the atomistic mechanisms behind the improved mechanical properties. To understand the effect of aging on the viscoelastic properties, dynamic mechanical analysis (DMA) was performed and is described in Chapter 5. In addition, Chapter 6 examines the effect of cryogenic temperatures on the mechanical behavior and properties of aged Zr–Ni–Al MG. Finally, we conclude by summarizing the major findings from this thesis and present an outlook for future experimental directions.

Chapter 2. Experimental Methods

2.1. Sputtering and aging of metallic glass thin films

A DC magnetron sputter deposition system (ATC Orion, AJA International, Inc.) was utilized to deposit $Zr_{56}Ni_{22}Al_{22}$ (ACI Alloys, Inc.) from a single alloyed sputtering target, as shown in figure 2.1. The target was produced from elemental sources with 99.99% purity. We chose to sputter and investigate Zr-Ni-Al MG because the properties of sputtered MGs remain largely uncharacterized, and this material possess a suite of beneficial properties such as: high T_g[30], oxidation resistance[80,81], good glass-forming ability[82,83], and fully metallic composition. The latter lends itself to conducting MD simulations to reveal atomic-level detail and physical processes that facilitate their deformation.

Prior to sputtering, the chamber was pumped down using a turbo and cryo pump system to a base pressure less than 10^{-6} Torr to ensure minimal contamination. The residual pressure most likely contained trace amounts of H_2O, CO, N_2 and H_2 [84]. However, at such low pressures, most of the gas resided on the walls of the sputtering chamber. For every gas molecule moving around in the chamber, there are approximately 500 gas molecules attached to the chamber walls[84]. Thus, gas adsorption onto our sample surface should be minimal.

Deposition occurred under 3 mTorr argon at 100 W DC power for 20 hours, which produced a 5 μm-thick Zr-Ni-Al MGTF. We used a 1 cm x 1 cm silicon (<100> orientation, P-type boron doped, 525 μm thickness) chip as our substrate. The silicon substrate was cleaned with acetone and isopropyl alcohol, followed by drying with compressed nitrogen gas. The native oxide layer was not chemically removed since the silicon substrate would still be exposed to air right before loading into

the sputtering chamber. Thus, allowing for the reformation of the native oxide layer. The deposition time was varied to achieve various thin–film thickness.

Room–temperature aging was achieved by placing the as-sputtered thin film in a nitrogen flow box for three years. The nitrogen flow box minimized the humidity and the possibility of surface contamination and oxidation. Access into the nitrogen flow box was minimal over the course of the three years aging process.

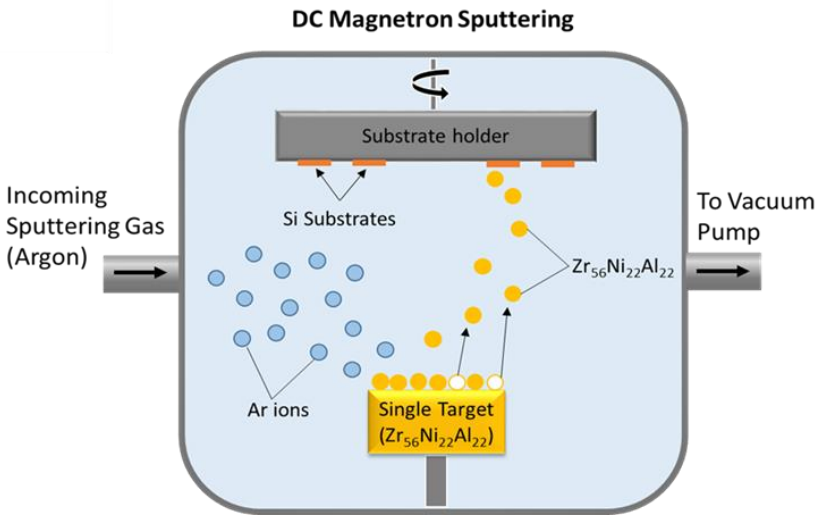

Figure 2.1. Schematic of DC magnetron sputter deposition system. A single alloyed sputtering target was utilized to deposit $Zr_{56}Ni_{22}Al_{22}$

2.2 Fabrication of micro- and nano-sized cylindrical pillars

Focused Ion Beam (FIB) milling was utilized to fabricate micro- and nano-cylindrical pillars on the as-sputtered and aged Zr-Ni-Al MGTF. First, a 40 μm diameter keyhole was milled using a Ga–ion FIB current of 5 nA and a voltage of 30 keV. The keyhole design allowed the pillar to be observed in the SEM during compression experiments and the wide 40 μm diameter was determined such that the indenter tip would only contact the pillar and not the surrounding substrate. Since the resolution and precision of this initial step was not crucial, higher ion beam currents (i.e., 5 nA) were

utilized to increase the material removal rate. After the 40 μm diameter circle, progressively smaller concentric circles were milled away at decreasingly lower currents until the pillar reached the desired dimensions. Lower ion beam current resulted in a smaller beam diameter, which improved the resolution and precision of the patterning. The final cleaning cut was performed at the lowest current of 10 pA. The pillars we fabricated had diameters between 300 nm to 1.1 μm and heights between 900 nm to 3.3 μm, respectively. To minimize buckling during compression experiments, the target height of each pillar was three times its diameter.

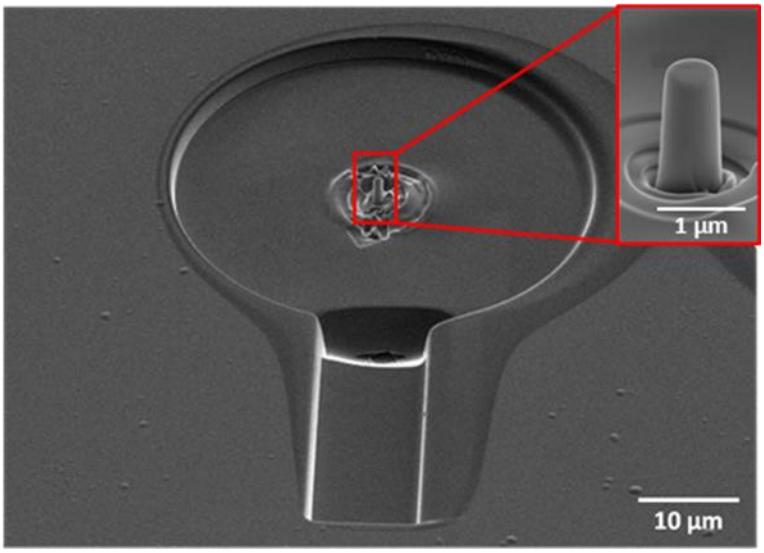

Figure 2.2. SEM image of representative FIB-milled pillar. Inset: zoomed–in view of the 900 nm diameter Zr–Ni–Al pillar

A representative FIB–milled pillar with the 40 μm keyhole is shown in figure 2.2. The darker shadow around the keyhole corresponds to the re–deposition that occurred from the Ga–ion bombardment of the MG sample. The inset is a zoomed-in view of the 900 nm diameter pillar. Substantial efforts were dedicated to minimize the tapering angle along the pillar axis to be $< 2^{o}$ so that uniform loading during uniaxial pillar compression experiments was achieved. For the as–sputtered pillar compression experiments, the pillars were freshly fabricated right after sputtering. For

the aged pillar compression experiments, the film was first aged at room temperature and then, pillars were freshly fabricated right before compression.

2.3 Microstructural characterization

2.3.1. X-ray diffraction (XRD)

Preliminary microstructural characterization of both the as-sputtered and aged Zr–Ni–Al MG thin films was conducted using XRD (Panalytical X'pert Pro, with Cu Kα wavelength). The diffractometer was operated in room temperature at a voltage of 45 kV and a current of 20 mA. The diffracted intensities were recorded between 20 to 65 degrees (2θ) with a step size of $2\theta = 0.03^{o}$. The MG sample was mounted into the XRD sample holder using modelling clay. A glass disk was pressed onto the MG to ensure that the sample's surface was flush with the surface of the sample holder.

2.3.2. Transmission electron microscopy (TEM)

Besides XRD, TEM is another method used to characterize the microstructure of the Zr-Ni-Al MG. A JOEL Grand ARM 300CF TEM microscope was operated at 200 keV to obtain the diffraction patterns and high-resolution TEM images. TEM samples, which consisted of 50 nm thick lamella cross-sections of the sputtered Zr-Ni-AL MG, were prepared using the FIB "lift-out" method. This method can be summarized in the following steps:

1. FIB is used to mill away the surrounding area of the targeted site
2. The targeted site is lifted out of the bulk sample using a micromanipulator and attached to a Cu TEM grid (PELCO FIB Lift-Out TEM grid, Ted Pella) by depositing Pt using the gas injection system
3. The targeted site is further thinned down until it is electron transparent (< 100 nm thick)

This method is advantageous because it can allow for very accurate (up to ~20 nm) selection of the targeted site, requires virtually no sample or surface preparation and is a relatively fast procedure (~3–4 hours)[85]. An SEM image of the Zr–Ni–Al lamella sample attached to a Cu TEM grid is shown in figure 2.3. The inset is a zoomed–in view of the 50 nm thick TEM lamella.

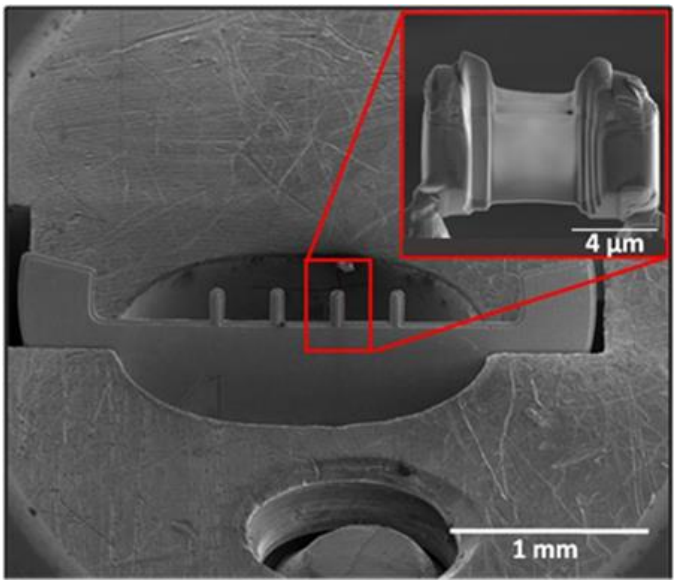

Figure 2.3. SEM image of a Cu TEM grid with a 50 nm thick Zr–Ni–Al lamella sample. Inset: zoomed–in view of the TEM lamella prepared via FIB lift–out technique.

2.4 Compositional characterization: Energy-dispersive spectroscopy (EDS)

EDS (EDAX Genesis 7000), coupled with a SEM (Nova 200, FEI Co.), was utilized to characterize the composition of the Zr-Ni-Al MG. From the SEM, an incident beam of high energy electrons can excite an inner shell electron in the atom of the target sample and eject it from its shell. An electron from an outer, higher energy shell drops down to fill the hole and the difference in energy is released in the form of an x-ray. These characteristic x-ray signals are unique to individual elements and can be used to determine a material's elemental composition.

In order to get an x-ray signal, the kinetic energy (i.e., accelerating voltage) of the impinging electrons needs to be at least two to three times the energy of the highest characteristic x–rays (Zr L–α x–rays are produced at 1.9 keV, Ni L–α x–rays are produced at 0.851 keV, and Al K–α x–rays are produced at 1.486 keV)[86]. Thus, any electron accelerating voltage over 6 keV should be able to generate characteristic x–ray signals from all three elements. However, using higher electron accelerating voltage would result in deeper penetration of the electrons into the sample. If the penetration depth exceeds the thickness of the TFMG, we would inadvertently probe the substrate.

Thus to determine the optimal accelerating voltage, we employed the Monte Carlo Simulation of Electron Trajectory in Solids to simulate the interaction of electrons with varying accelerating voltage on our TFMG. In particular, the simulation predicts the trajectories of these impinging electrons and records the resulting amount of backscattered electrons and x–rays from the sample. Figure 2.4 is a plot of the trajectories of two hundred 10 keV electrons irradiating a 5 μm thick $Zr_{56}Ni_{22}Al_{22}$ sample on an infinitely thick silicon substrate. The red lines correspond to backscattered electrons that elastically scatter and emerge from the surface of the material. Blue lines correspond to the electrons that are in-elastically scattered and reabsorbed. Electrons are simulated as coming down (perpendicular) into the sample at (0 nm, 0 nm) where the y–axis of the plot corresponds to the depth in the sample. For 10 keV electrons, the penetration depth is about 430 nm. Since our TFMG is 5 μm thick, there are no concerns that the electron beam will reach our substrate.

Another important parameter to adjust is the current of the electron beam. The current is directly related to the amount of electrons and the number of x-rays (i.e., the signal) that is produced. The higher the current, the more signal we get. However, too high of a current will result in large

beam size which decreases the spatial resolution. For our sample, a beam current of 1 nA was able to provide enough signal while maintaining high resolution.

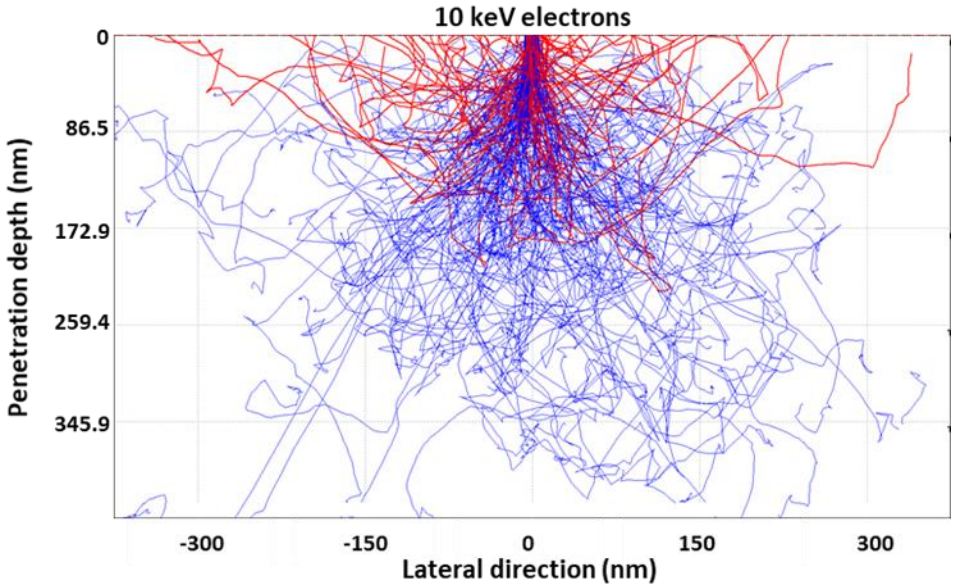

Figure 2.4. Monte Carlo Simulation of Electron Trajectory in Solids for two hundred 10 keV electrons impinging on a 5 μm thick Zr-Ni-Al MGTF. The red lines correspond to backscattered electrons that elastically scatter and emerge from the surface of the material. Blue lines correspond to electrons that are in-elastically scattered and reabsorbed.

2.5 Quasi–static uniaxial pillar compression

2.5.1 Room temperature

In-situ uniaxial pillar compression experiments on individual pillars were performed quasi–statically using a Hysitron PI–85 pico–indenter in a SEM (Versa SEM, FEI Co.). Figure 2.5 (a) is an image of the pico-indenter where the Zr-Ni-Al MG sample (on the left) is loaded perpendicular to the FIB–milled flat punch (on the right). A SEM image of the indenter almost in contact with the pillar is shown in figure 2.5 (b). As the indenter applies a load to the pillar, the deformation can be observed in SEM (as seen in figure 2.5 (c)).

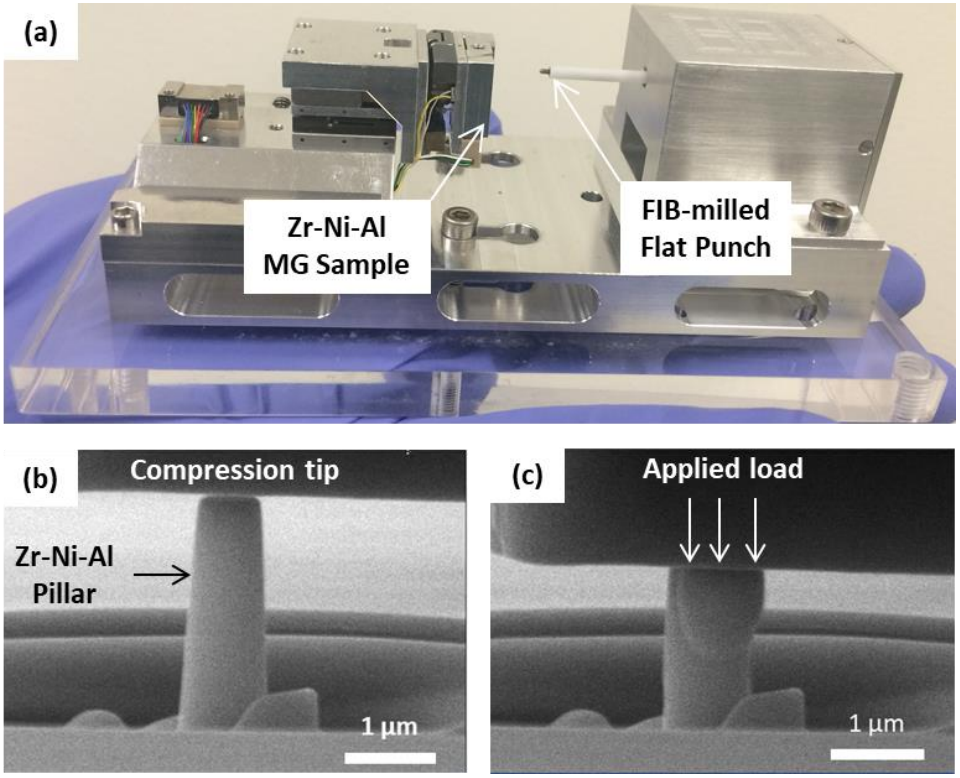

Figure 2.5. In-situ nanomechanical testing. (a) Hysitron PI-85 pico–indenter with the Zr-Ni-Al MG sample (on the left) loaded perpendicular to the FIB–milled flat punch (on the right). (b) SEM image of the indenter (compression tip) almost in contact with the Zr-Ni-Al pillar. (c) SEM image of the indenter applying a load to the pillar and forming a shear band.

A constant strain rate of 10^{-3} s^{-1} was applied using a 5 µm-diameter boron–doped diamond flat punch. Care was taken to ensure that the bottom of the flat punch was parallel with the top of the pillar so that the compression was uniaxial. The raw load (P) and displacement (Δl) was recorded at an acquisition rate of 100 Hz. Using this load and displacement data, the engineering stress and strain were calculated using the initial pillar height (h_0) and diameter (d_0), which were measured from SEM images prior to compression. Fabricating the pillars using FIB resulted in a tapered pillar with nonuniform diameter. We minimized the tapering angle along the pillar axis to be below 2°. The initial pillar diameter is defined as the diameter at half of the pillar height.

The equations for calculating engineering stress and strain are listed below:

$$\sigma_{eng} = \frac{P}{\pi\left(\frac{d_0}{2}\right)^2} \tag{2.1}$$

$$\varepsilon_{eng} = \frac{\Delta l}{h_0} \tag{2.2}$$

The Young's modulus was calculated from the slope of the unloading stress–strain curve, focusing on the linear segment. The yield strength was determined by offsetting the linear fit of the Young's modulus by 0.2% strain and determining the intersection of that offset line with the stress–strain data.

2.5.2 Cryogenic temperature

Our cryo–mechanical experimental setup consisted of a SEM (Quanta SEM, FEI Co.) combined with a nano–indenter (InSEM, Nanomechanics, Inc.) and a cryogenic assembly by Janis Research Company. Liquid nitrogen was used to provide cooling for the cryogenic experiments. It was delivered through the vacuum-shielded transfer line and into the cold finger assembly, as shown in figure 2.6. Inside the SEM, the cold finger assembly is connected to both the sample holder and the indenter head via a thermally conductive copper ribbon. This ensured that both the sample and indenter was equilibrated at the same temperature during the compression experiments. Temperature was measured by two thermocouples: (1) at the entry of the cold finger to the SEM chamber and (2) directly at the sample holder.

Liquid nitrogen cooled the sample and the indenter tip to a constant temperature of 140 K. Cooling from room temperature to 140 K took three hours, after which the sample was equilibrated for another two hours before compression experiments were performed. The cooling rate is dependent on the flow rate of liquid nitrogen into the cold finger assembly. Even though our cryo–mechanical experimental setup was situated on a vibration isolation table, flowing liquid nitrogen at

high rates introduced vibrations that were observable in the SEM. Thus, the optimal flow rate was determined by minimizing the vibrations while maintaining a reasonable cooling rate (i.e., cooling from room temperature to 140 K in three hours). Even though the temperature of liquid nitrogen is 77 K, we were limited to the base temperature of 140 K due to the thermal losses from the cold finger assembly to our sample. Increasing the flow rate can overcome these thermal losses; however, higher flow rates resulted in greater vibrations.

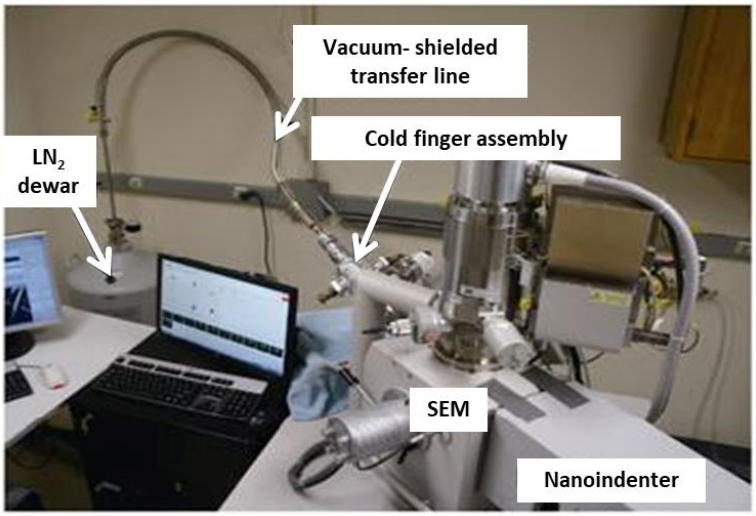

Figure 2.6. Cryo–mechanical experimental setup: SEM (Quanta SEM, FEI Co.) combined with a nano–indenter (InSEM, Nanomechanics, Inc.) and a cryogenic assembly by Janis Research Company

Quasi–static uniaxial pillar compression at cryogenic temperatures was performed using a 5 μm tungsten carbide flat punch indenter that was coated with 5 nm-thick gold (Au) by e-beam evaporation. Au was chosen for its excellent conductive and corrosion-resistant properties. The conductive Au coating was essential towards minimizing charging artifacts when the tip was observed under SEM. Although Au is a relatively soft material, it's effect on the mechanical properties is negligible due to the thinness of the layer. Zr–Ni–Al pillars were compressed to a maximum strain of 10% and at a strain rate of 10^{-3} s^{-1}. The nanoindenter was operated under displacement–rate–controlled mode.

2.6 Dynamic mechanical analysis experiments

2.6.1 Room temperature

In–situ DMA experiments were performed on Zr–Ni–Al pillars using SEMentor, a combined SEM (Quanta SEM, FEI Co.) with a nano–indenter (InSEM, Nanomechanics, Inc.). For consistency with the quasi–static uniaxial pillar compression experiments, the same pillar diameter ranges (i.e., between 300–1100 nm) were investigated. Figure 2.7 (a) is a schematic plot of the loading curve as a function of time where each pillar was initially compressed to a static load that corresponded to an initial stress (σ_o) and strain (ε_o). The initial stress was kept below the yield stress (σ_y) so that the MG stayed within its elastic regime. Then, an additional dynamic force was applied to create a dynamic displacement such that both the stress (σ) and strain (ε) on the pillar were sinusoidal with time.

$$\sigma = \sigma_0 sin(\omega t) \tag{2.3}$$

$$\varepsilon = \varepsilon_0 sin(\omega t + \delta) \tag{2.4}$$

The phase difference between the applied stress and strain response is defined as the phase lag (δ) and is shown in figure 2.7 (b). The blue curve corresponds to the sine wave generated by the force motor, while the orange curve corresponds to the sine wave for the sample's response to the applied force. As expected, the signal precedes the response. If a material is purely elastic, then there is no phase difference between the stress and strain. On the other hand, if the material is purely viscous, then the phase difference is $\pi/2$. The storage (E') and loss modulus (E'') can be calculated using the phase lag and the initial stress and strain values (equations 2.6 and 2.7). The storage modulus represents the stored elastic energy while, the loss modulus represents the internal friction and quantifies the energy dissipation within the material.

$$\tan\delta = \frac{E''}{E'} \tag{2.5}$$

$$E' = \frac{\sigma_0}{\varepsilon_{0\,0}}\ cos(\delta) \tag{2.6}$$

$$E'' = \frac{\sigma_0}{\varepsilon_{0\,0}}\ sin(\delta) \tag{2.7}$$

The frequency (ω) of the dynamic force was varied between 2 to 600 Hz. As shown in the schematic plot of load vs. time in figure 2.7 (a), the total stress on each pillar was maintained below the pillar's yield strength. Similar to the cryogenic compression experiments, a 5 µm tungsten carbide flat punch indenter that was coated with 5 nm thick gold (Au) was utilized. To ensure that the MG remained within the elastic regime during DMA, the dynamic force was adjusted to remain below the static load and the dynamic displacement was less than the initial loading displacement.

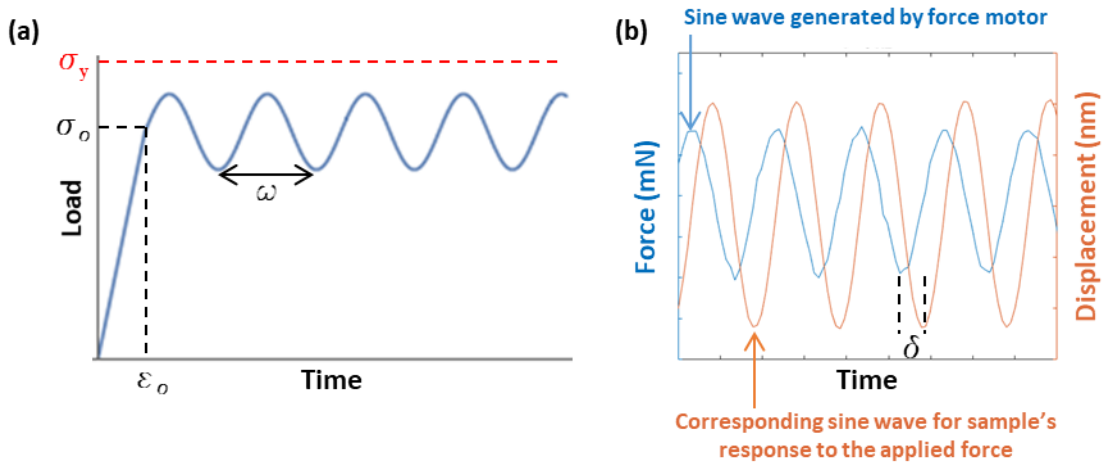

Figure 2.7. Schematic plots of (a) the loading curve as a function of time and (b) the sinusoidal applied force and the material's response signature as a function of time.

Determining the target dynamic displacement such that the indenter always remained in contact with the pillar is very crucial. There are various techniques to verify that contact is maintained. For example, since our indenter tip and sample are both electrically conductive, we could measure the resistivity between the indenter tip and our Zr-Ni-Al sample. Another method involves applying a dynamic displacement while monitoring the loss modulus. We chose to use the later method due to its feasibility. Figure 2.8. is an example of a DMA calibration experiment where the target dynamic

displacement was varied from 5 to 65 nm. This target dynamic displacement was applied in addition to the initial loading displacement of 0.5% strain, which corresponded to a static load of 300 μN. From the plot of the loss modulus as a function of target dynamic displacement, we observed a sudden increase in loss modulus at a dynamic displacement of 20 nm. This signature implies that the indenter tip is beginning to lose contact with the pillar. These observations were confirmed by SEM imaging where we noticed a slight change in contrast of the indenter once contact was lost. For each sample and pillar size, we experimentally determined the maximum dynamic displacement and remained below this maximum during our DMA experiments.

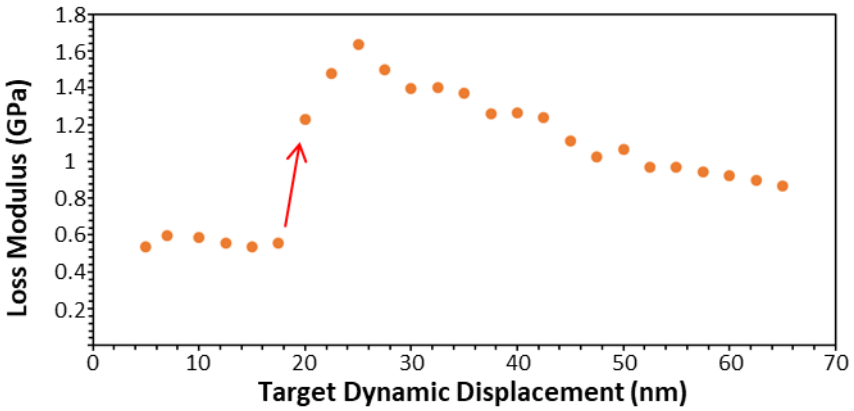

Figure 2.8. Loss modulus as a function of target dynamic displacement. The sudden increase in loss modulus at 20 nm (denoted by red arrow) suggests that the indenter tip is beginning to lose contact with the pillar.

2.6.2 High temperature

High temperature DMA, up to 360 K, was performed to understand how the viscoelastic properties of Zr-Ni-Al MG varied as a function of temperature. Using the same setup as the room temperature DMA, the sample holder and the indenter tip were both connected to a thermally conductive copper ribbon, which was attached to a resistive heater. This ensured that both the sample and indenter were equilibrated at the same temperature during the high temperature DMA experiments. A thermocouple was placed directly at the sample holder to measure the temperature. A

temperature controller was used to adjust the amount of heating required to reach the temperature set point. It operated on the principles of a proportional-integral-derivative (PID) feedback loop and was calibrated such that the heating from room temperature to 360 K occurred smoothly without temperature overshoots or oscillations.

Chapter 3. Substantial Strength Enhancement through Room–Temperature Aging

3.1. Characterization of aged metallic glass

3.1.1. SEM and EDS results

Cross–sectional SEM images of the same as-sputtered and aged 5 μm–thick Zr–Ni–Al MG on a silicon substrate are shown in figure 3.1(a) and (b), respectively. The bottom interface corresponds to the boundary between the Zr-Ni-Al MG and the silicon substrate. The difference in brightness and contrast is due to the sample's tilting angle. The as-sputtered sample is tilted to 90°, while the aged sample is tilted to 52°. Thus, in the as-sputtered sample, the black region above the Zr-Ni-Al MG corresponds to the background from the SEM chamber. In the aged sample, the top interface corresponds to the boundary between the cross-sectional view and top-view of the Zr-Ni-Al MG. Both of these images reveal that the Zr-Ni-Al MG surface is smooth (without any holes or cracks) and delamination did not occur between the MG and the substrate.

Chemical compositions obtained via energy-dispersive x-ray spectroscopy (EDS), shown in color below their respective SEM images, convey that the glass was predominantly composed of zirconium (55 ± 3%) with lower amounts of nickel (28.6 ± 0.1%) and aluminum (16.4 ± 1.6%). This composition remained within experimental uncertainty after aging.

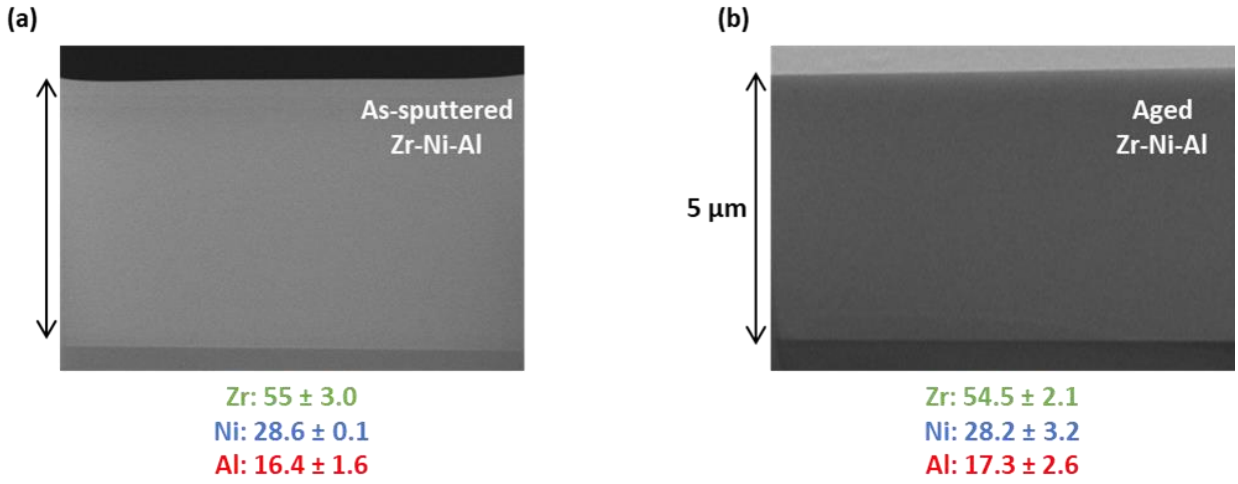

Figure 3.1. Cross-sectional SEM images of 5 µm-thick Zr–Ni–Al MG in the (a) as–sputtered and (b) room–temperature aged state. EDS compositions for each state are denoted below their respective SEM image.

3.1.2. XRD and TEM results

Figure 3.2 (a) shows the XRD data for the as-sputtered 300 nm-thick Zr–Ni–Al on Si (yellow), Si substrate (blue), and 5µm-thick aged Zr–Ni–Al on Si (orange). Since Zr–Ni–Al was sputtered onto a silicon substrate, we can noticeably discern the contributions from silicon in both XRD curves. The 5 µm aged Zr–Ni–Al sample exhibits a jump in intensity at 29.5°. This is attributed to the strong diffraction of the x-rays at the interface between the silicon substrate and the Zr-Ni-Al thin film. This diffraction does not occur for the 300 nm-thick as–sputtered sample because it is too thin for the measured 2θ angles to detect. The measured 2θ angles ranged from 20° to 65°. All peaks that are observed in both Zr-Ni-Al samples are also present in the Si substrate. The overall broad background spectra suggests that both samples are amorphous. However, the aged Zr–Ni–Al has a broad diffuse hump that is centered around 36.8°, which is not observed in the as-sputtered sample. Microstructural relaxations over three years may have occurred and resulted in an increase in SRO. However, XRD is not suitable to conclusively determine that microstructural relaxation occurred.

The diffraction pattern and high-resolution TEM micrograph of a representative cross-section extracted from the aged MG are shown in figure 3.2 (b) and (c), respectively. The diffuse rings in the diffraction pattern combined with the lack of any crystallization or observable ordering in the high resolution TEM image unambiguously prove that the aged Zr–Ni–Al is amorphous. However, aging could have resulted in small changes to the short– and medium–range atomic order, but these changes are not detectable by TEM. In the upcoming chapter, we will turn to MD simulations to reveal the microstructural changes.

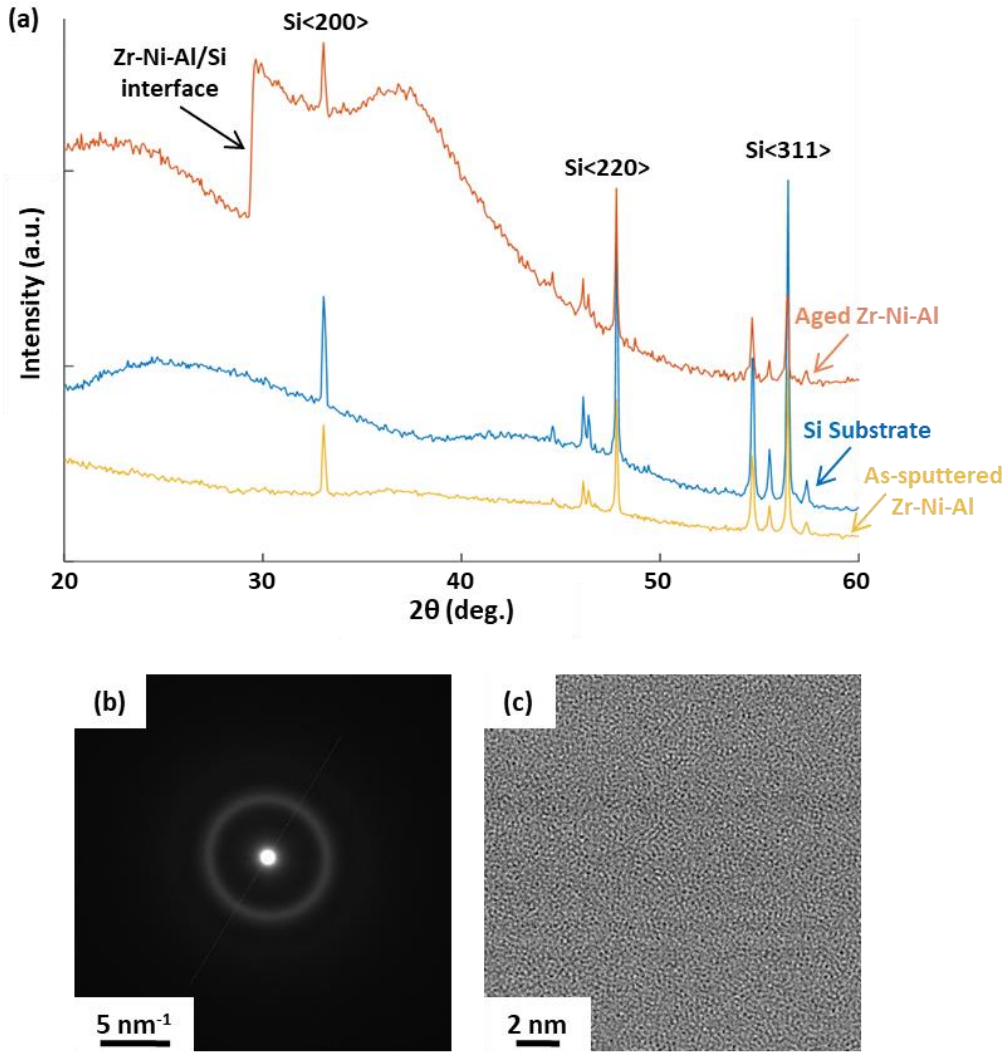

Figure 3.2. Microstructural characterization of Zr-Ni-Al. (a) XRD spectra for the as-sputtered 300 nm-thick Zr–Ni–Al on Si (yellow), Si substrate (blue), and 5µm-thick aged Zr–Ni–Al on Si (red). (b) Diffraction pattern and (c) high resolution TEM confirm amorphous microstructure of aged Zr–Ni–Al.

3.2. Nanomechanical compression results

3.2.1. Pillar diameter < 600 nm

Representative SEM images and stress-strain data for aged samples with diameters between 300 to 600 nm are shown in figure 3.3. SEM images of a 300 nm diameter pillar before (figure 3.3 (b)) and after (figure 3.3 (c)) compression reveal homogeneous–like deformation after loading to 15% strain, with localized failure events. This deformation signature is consistent with the relatively smooth post-elastic regime of the stress–strain data shown in figure 3.3 (a). Deformation in these pillars was predominantly isolated to the top section of the pillar, where the initial diameter was narrowest and resulted in the highest local stresses. Compression data from Liontas et al. on equivalently sized pillars fabricated from the same MGTF three years earlier (i.e., immediately following sputtering) is provided for comparison[1].

All aged pillars exhibit the characteristic linear elastic loading up to a stress of approximately 2.6 ± 0.2 GPa followed by a relatively smooth post-elastic regime with the characteristic serrated flow signature. The serrated flow is caused by minor deformations of the STZs. From the post-elastic regime of the stress-strain curve, we observe the serrated flow signature in the minor load drops where the neighboring atoms recover elastically and prevent further deformation. As loading continues, this process repeats and serrated flow is obtained[87]. The yield stress of as–sputtered samples of the same sizes was 1.81 ± 0.4 GPa. The as-sputtered samples also exhibited the same deformation signature. Marginal deviations from linearity in the early stages of loading likely stem from a slight initial misalignment and imperfect contact between the indenter and pillar.

The first 5% of the unloading curve (i.e., the linear regime) is used to calculate the Young's modulus of 90 ± 5 GPa for the aged samples. The as-sputtered samples had a Young's modulus of 69 ± 3 GPa, which is 23% lower than the aged samples. Although three curves are shown, the self-

consistency of all mechanical data was verified over 17 samples. This demonstrates their high reproducibility and the deterministic nature of their deformation. Hardening is observed in both the as-sputtered and aged samples. The hardening slope ranged from 9–11.2 GPa for the aged samples and 6.5–8 GPa for the as-sputtered samples.

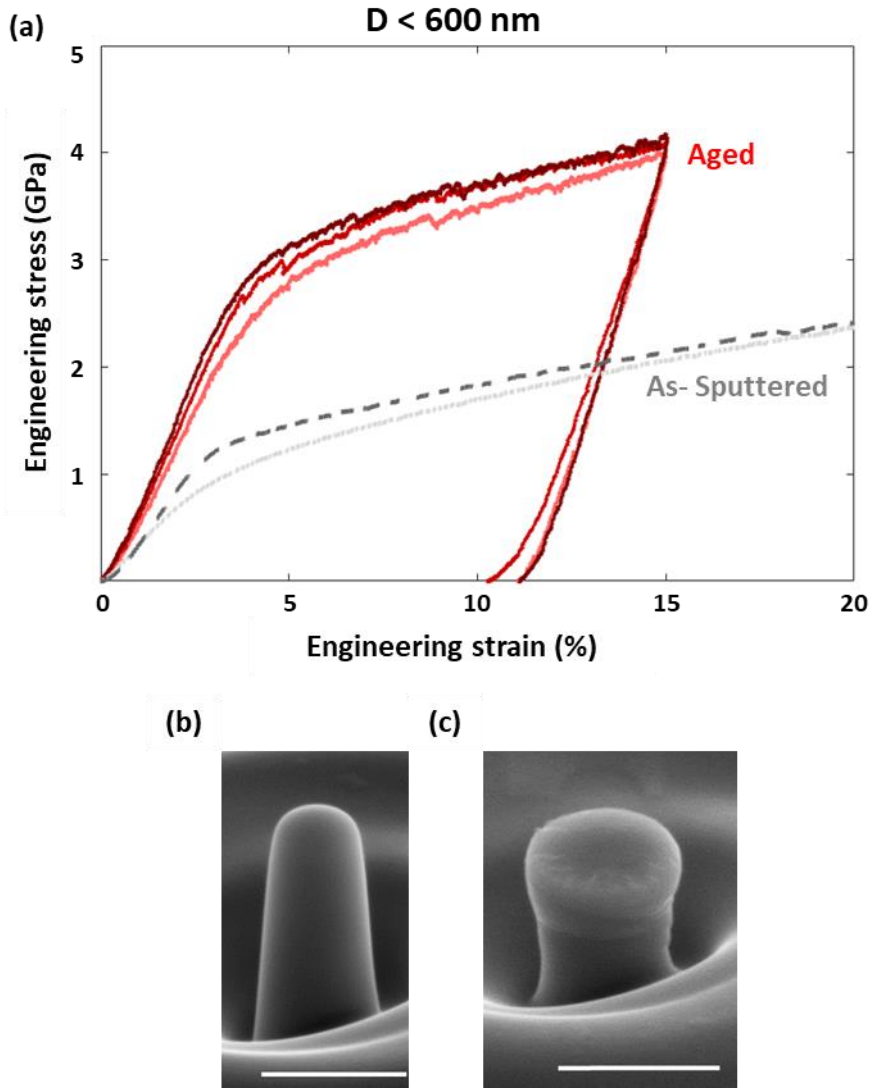

Figure 3.3. Uniaxial compression of pillars with diameters between 300–600nm. (a) Engineering stress–strain data for aged (denoted in red) and as-sputtered (denoted in gray) Zr-Ni-Al MG. SEM images (b) before compression and (c) after compression. All scale bars in the SEM images correspond to 500 nm.

3.2.2. Pillar diameter > 600 nm

Fig 3.4 contains representative SEM images and stress-strain data for aged samples with diameters between 600 to 1100 nm. Stress- strain data (shown in figure 3.4 (a)) and SEM image of a compressed 1 μm diameter pillar (figure 3.4 (c)) provide evidence that the deformation mechanism in the larger samples is dominated by shear banding and localized failure.

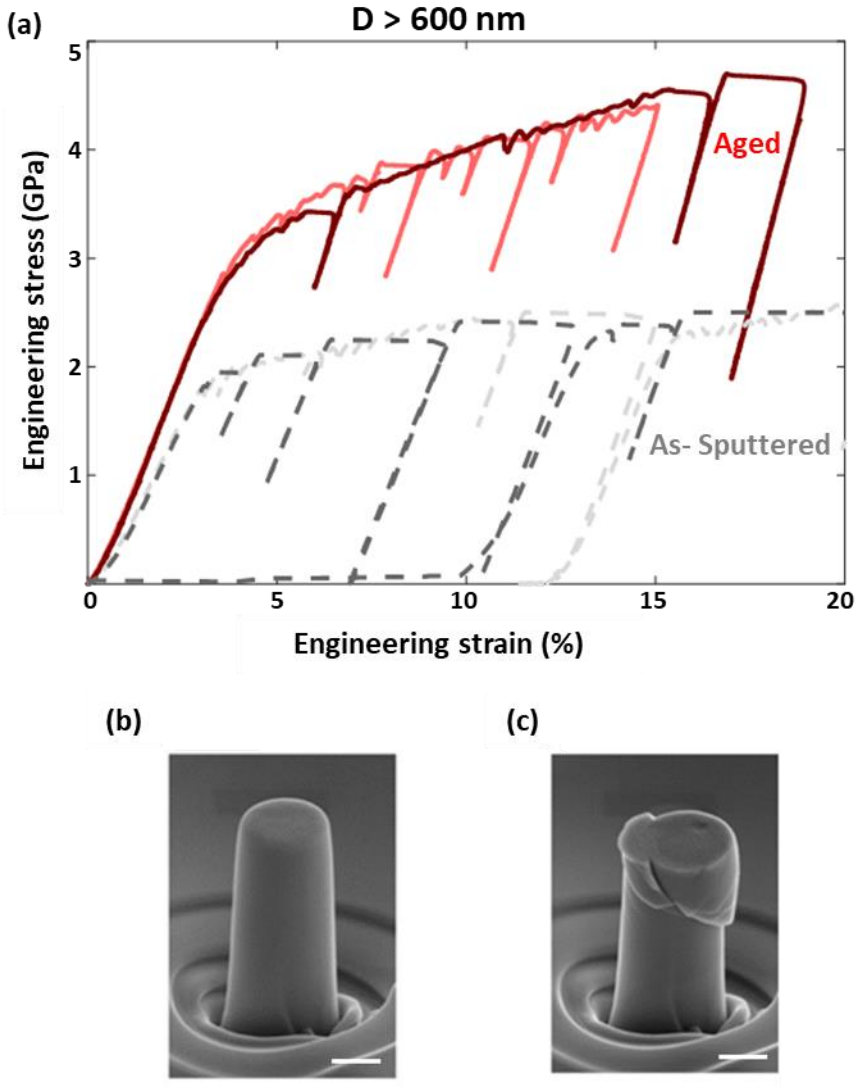

Figure 3.4. Uniaxial compression of pillars with diameters between 600–1100nm. (a) Engineering stress–strain data for aged (denoted in red) and as-sputtered (denoted in gray) Zr-Ni-Al MG. SEM images (b) before compression and (c) after compression. All scale bars in the SEM images correspond to 500 nm.

The shear bands first initiated near the top of the pillar, and as the loading continued, they propagated along the entire gauge section. Strains larger than 40% caused the shear bands to propagate down to the silicon substrate, at which point, the samples catastrophically failed. Stress-strain plots revealed a Young's modulus of 91 ± 4 GPa and a yield strength of 2.7 ± 0.2 GPa. These values are nearly equivalent to those of the smaller pillars. Since the Young's modulus is an intrinsic property, the lack of size effect is expected. Similarly, hardening is present in the larger pillars for both the as–sputtered and aged samples. The hardening slope is measured to be 3.5–4.8 GPa for the as-sputtered sample and 8.8–11.3 GPa for the aged sample.

A summary of the mechanical properties for sputtered Zr–Ni–Al MGs before and after aging as a function of pillar diameter is shown in figure 3.5. It confirms that the Young's modulus (figure 3.5 (a)) and the yield strength (figure 3.5 (b)) remained constant for all sample diameters. Aging increased the yield strength from 1.81 ± 0.4 GPa to 2.7 ± 0.2 GPa and enhanced the Young's modulus from 69 ± 3 GPa to 91 ± 4 GPa. Uniaxial pillar compressions were also performed after four years of aging. The Young's modulus and yield strength are plotted as open red diamonds in figure 3.5. They matched consistently with those from the three year aged samples. Aging after three and four years yielded the same deformation modes; namely, homogeneous deformation for pillars with diameters less than 600 nm and shear banding for pillars with diameters larger than 600 nm.

Substantial percentage changes in mechanical properties were also observed when the sputtered MG was thermally annealed to sub-T_g temperature of 625 ^oC for 24 hours[1]. Other studies reported 10% to 15% change in mechanical properties for bulk MGs after annealing[88]. Since the sputtered thin films are in a relatively higher potential energy state, the material can relax to a lower energy state after aging or annealing. Thus, we expect post processing treatments to have a greater effect on the mechanical properties of sputtered thin film MGs than bulk MGs. The impact to the

mechanical properties due to aging and annealing is similar; which led us to hypothesize that the physical mechanisms of these two processes may be comparable. We will further explore their similarities in the upcoming chapter.

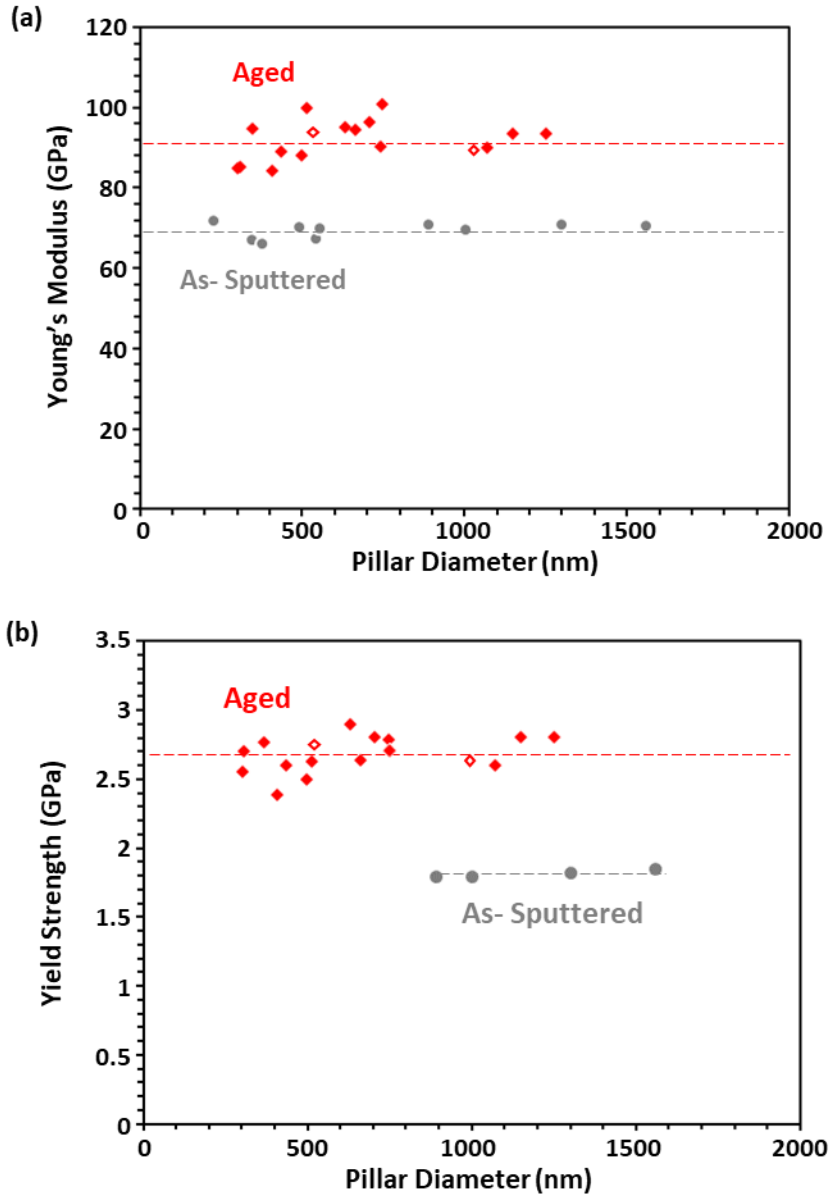

Figure 3.5. Mechanical properties of room–temperature aged (denoted in red; solid and open diamonds correspond to aging for three and four years, respectively) and as-sputtered (gray) Zr–Ni–Al MG. (a) Young's modulus and (b) yield strength as a function of pillar diameter. Horizontal dashed lines correspond to the average value of each property.

3.3 Discussion

Uniaxial pillar compression experiments of aged Zr–Ni–Al MG demonstrated three key results:

1. As-sputtered and aged pillars with diameters less than 600 nm experienced homogeneous deformation, while those with larger diameters deformed via shear banding.
2. The hardening rate increased by ~ 40% to 10 GPa after aging.
3. The aged samples are consistently ~43% stronger and ~30% stiffer than the as-sputtered ones with equivalent diameters.

3.3.1 Size effect on deformation mechanism

To understand the underlying physics of deformation mechanism transition from noncatastrophic to failure via initiation and propagation of multiple shear bands, it is useful to model the expansion of shear bands from an energy approach. A shear band can only expand over an incremental distance if it is an energetically favorable process, i.e., if the strain energy relief associated with its propagation is larger than the energy penalty of its formation. Two criteria are needed to be satisfied for a shear band to propagate:

1. The local stress at its leading edge, which depends on the size of the shear band, the loading geometry and shear-induced disordering, must be sufficiently large to cause local shearing and;
2. The total energy of the system must be reduced as a result of its expansion.

Volkert et al. and Jang et al. proposed that the formation and propagation of a shear band occurs when the decrease in stored elastic strain energy (left-hand side of equation 3.1) offsets the increase in shear band energy (right-hand side of equation 3.1)[74,76]:

$$\frac{\pi\varepsilon\sigma r^2 L}{2} = \sqrt{2}\pi r^2 \Gamma \tag{3.1}$$

where ε is the strain, σ is the applied stress, and $\pi r^2 L$ is the pillar volume. The shear band is assumed to travel at a 45° angle and Γ is the shear band energy per unit area. The critical stress for shear band formation (σ_c) can be solved from equation 3.1 by substituting the elastic modulus, (E) for σ/ε and L for $3d$ (since the length to diameter aspect ratio is 3:1):

$$\sigma_c = \sqrt{\frac{2^{1.5}\Gamma E}{3d}} \tag{3.2}$$

This suggests that as the pillar diameter decreases, there is less stored elastic strain energy available to balance out the increase in energy required to form a shear band and thus, the critical stress increases. Since the Young's modulus and yield strengths are both intrinsic parameters that are independent of size[5], there exists a critical size where the stored elastic strain energy and the shear band formation energy crossover. For larger pillars, shear bands dominant because the critical stress is lower than the driving stress for homogeneous flow. However, for smaller pillars, homogeneous deformation occurs because the critical stress is higher than the driving stress for homogeneous flow, which results in the activation of shear transformation zones (STZs) within the pillar.

In contrast to theory, we define the initial shear band nucleation and propagation event in each stress-strain dataset as the point where the stress drop exceeds 500 MPa. This threshold corresponds to the first observable (via SEM) propagation of shear band during compression. For example, in a typical aged pillar with a diameter of 900 nm, the incipient shear band propagated through the sample at a strain of 3.9% and at an applied stress of 3.3 GPa. Equivalently sized as–sputtered samples exhibited the first drop in stress at a lower global strain of 2% and at a stress of 1.9 GPa. This observation is consistent throughout all pillar sizes, which suggests that the aged samples require greater stresses to initiate shear band propagation. Figure 3.6 summarizes the experimentally

obtained shear band propagation stresses as a function of pillar diameter and reveals that they remain relatively constant for each type of sample: 1.81 ± 0.4 GPa for the as-sputtered samples and 2.6 ± 0.2 GPa for the aged ones. Theoretical critical stresses, calculated using equation 3.2, are also shown as the dashed curves in figure 3.6. Experimentally, the sputtered Zr–Ni–Al exhibited the transition from shear banding to homogeneous deformation at a diameter of 600 nm. For pillars with diameters less than 600 nm, it is evident that the shear band propagation stress is less than the critical stress, thus noncatastrophic deformation occurs. However, for pillars with diameters greater than 600 nm, the shear band propagation stress is larger than the critical stress; thus the deformation is dominated by shear bands.

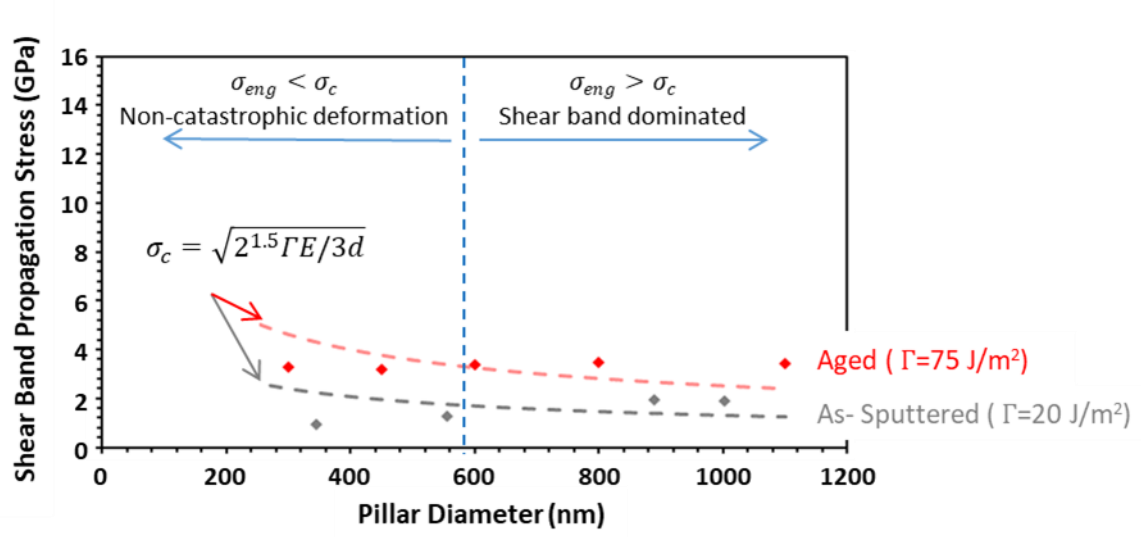

Figure 3.6. Experimentally measured stress for shear band propagation (data points) as well as the calculated critical stress for shear band propagation plotted against pillar diameter for aged (red) and as-sputtered (gray) Zr–Ni–Al metallic glass.

3.3.2. Hardening in aged metallic glass

From figure 3.7, we observed that the hardening rate increased to ~10 GPa after aging. This is ~40% increase in the hardening rate and is independent on the size of the pillars. Since the "as–

sputtered" samples and aged samples were all prepared and tested by the same procedures, we believe that the difference in the hardening rate is due to the spontaneous relaxation of the sputtered film at room temperature over the three– to four–year period of time. Such relaxation reduces the free volume and increases the density of the MG, resulting in a hardening material.

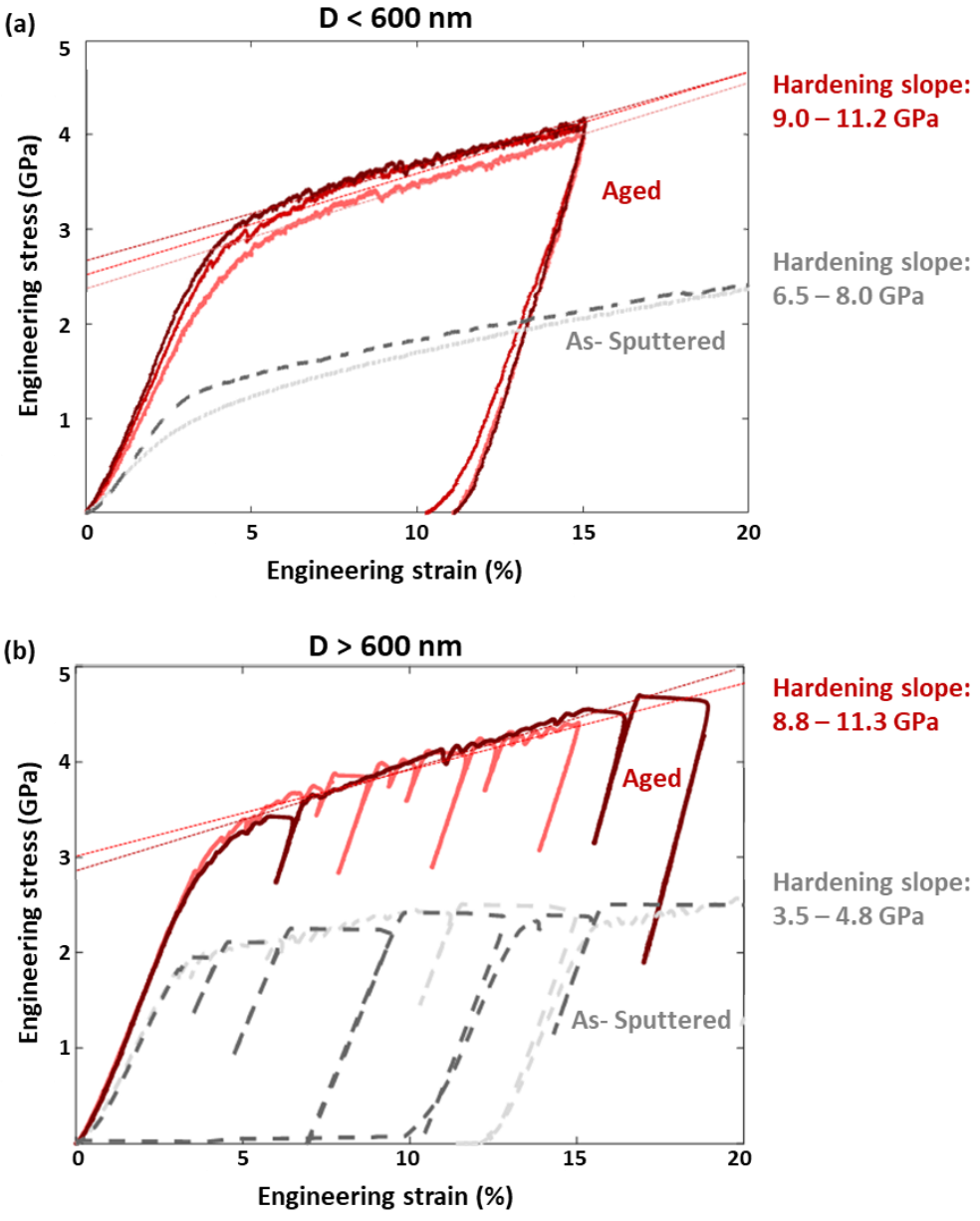

Figure 3.7. Hardening in aged vs. as-sputtered Zr-Ni-Al MG for pillar diameters (a) D < 600 nm and (b) D > 600 nm.

The observed hardening in aged Zr-Ni-Al MG can be explained by the increase of icosahedral SRO and stress-driven densification of the MG due to the applied load. The increase in icosahedral SRO is strongly influenced by microstructural relaxations such as β–relaxations[88–91]. Figure 3.8 schematically describes the β–relaxation process, which consists of small movement or rearrangement of atoms in the MG material due to temperature or stress[92]. It is the phenomenon that dominates below T_g, as opposed to the α-relaxations that dominate near T_g. The temperature range of β–relaxations fit well to our room–temperature aging process. β–relaxations are confined mainly to SRO length scales with no significant atomic rearrangements occurring on medium-range order length scales. Since pillar size does not seem to be a factor in the aging process, we believe this β–relaxation is occurring in both the core and the surface of the MG pillar[93]. Experimental studies show that the activation energy of β–relaxation has an approximately linear relationship to T_g, which is similar to the relationship found in crystalline metals[37,94–98].

$$E_\beta = 26RT_g \tag{3.3}$$

where R is the gas constant. For our Zr-Ni-Al MG, T_g is ~ 757 K and thus, E_β is about 150 kJ/mol or 1.39 eV. Thermal annealing experiments showed that the β–relaxation process was still occurring after 100 hours at 50° C. Based on the calculation of E_β, this condition is equivalent to more than 9 months of room temperature aging and fits well with the time scale in our aging experiments. Thus, we speculate that the observed material hardening is due to the stress–driven densification of the MG through the β–relaxation process.

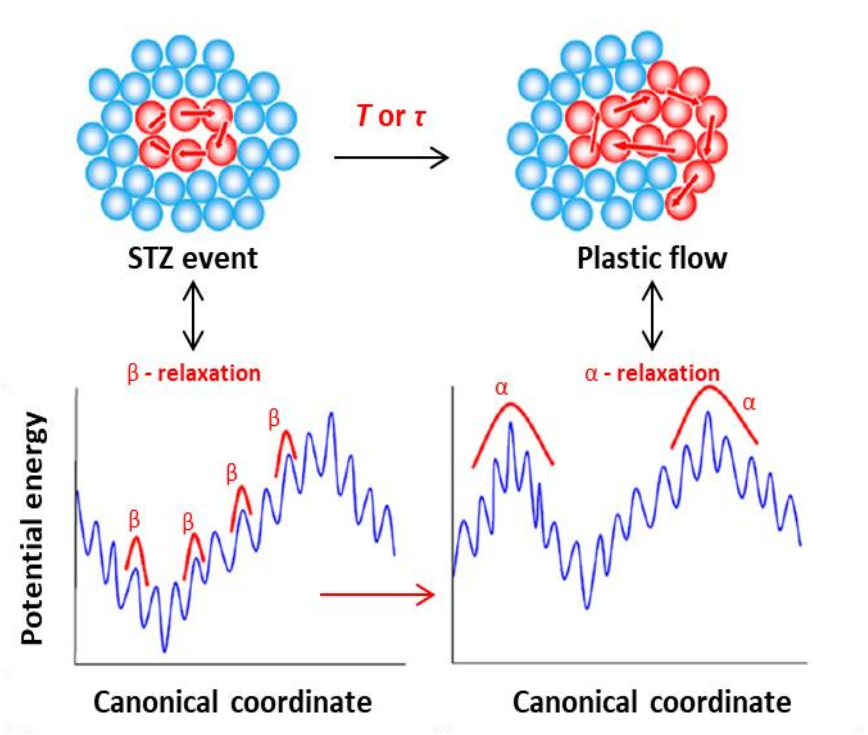

Figure 3.8. A 2D schematic illustration of STZ or flow unit activation of β–relaxations (left) and α-relaxations (right), and their corresponding origination in the potential energy landscapes. Blue circles represent atoms with low propensity of motion, while the red circles represent atoms with high propensity of motion. The arrows indicate the possible motion of atoms. β–relaxations correspond to the stochastically and reversible activated hopping events across "sub-basins", which are confined within the inherent megabasin; while, α-relaxations correspond to the irreversible hopping events that extend across different energy landscape megabasins[88].

3.3.3. Microstructural relaxation

We attribute the substantial increase in Young's modulus and yield strength after aging to the microstructural relaxation that occurred via atomic rearrangements and a concomitant reduction in free volume during aging. These atomic rearrangements resulted in larger clusters of atoms that are in a lower potential energy state than those of the as-sputtered sample. Hence, they are stiffer and can accommodate larger stresses before nucleating and propagating shear bands. From the previous discussion, we can determine the shear band activation energy density (Γ) in the aged vs. as-sputtered

samples by equating the strain energy relief to the energy of shear band formation for d = 600 nm (the critical diameter where the deformation mode transitions). For the aged sample, Γ = 75 J/m^2, while for the as-sputtered sample, Γ = 20 J/m^2. The combination of higher critical stress and larger shear band activation energy density in the aged sample suggest that microstructural relaxation occurred, which led to a redistribution and reduction in the free volume. To reveal further insight, we will be turning to MD simulations in the upcoming chapter.

To confirm our explanation of microstructural relaxation, a direct measurement of the atomic spacing, which is related to the free volume, before and after aging will be a useful supporting evidence. We propose to use synchrotron XRD for this study. In sputtered Zr-Ni-Al MG, synchrotron XRD has been used to demonstrate that annealing reduced the free volume[1]. The differences in peak position of the scattering vector Q quantify the amount of atomic spacing. Q is related to the mean atomic volume by the following equation[99]:

$$\frac{V_{aged}}{V_{as-sputtered}} = \left(\frac{Q_1^{as-sputtered}}{Q_1^{aged}}\right)^3 \tag{3.4}$$

where V_{aged} and $V_{as\text{-}sputtered}$ are the average atomic volumes in the aged and the as-sputtered states, respectively. Therefore, by measuring the position of the principle peak (Q_1), we can estimate the change in atomic volume and the resulting change in free volume due to aging.

Compared to crystalline metals, MGs have lower elastic moduli. This is attributed to the higher density of atoms (~2% denser) in a crystalline metal [100]. Simulations on the effect of equilibrium density on the elastic constants reveal that the shear modulus of amorphous metals can be 29-58% lower than that of a crystalline solid[100]. Similarly, the bulk modulus of amorphous metals can be increased by 4-17% upon crystallization[100]. In our work, we observed a significant enhancement in the

Young's modulus. Microstructural relaxation reduces the free volume and increases the atomic density. Although our aged Zr-Ni-Al MG remained amorphous, it is possible that the enhancements in Young's modulus is related to the increase in SRO such that the microstructural state becomes 'slightly closer towards crystalline'.

3.4 Summary

We investigated the effect of room–temperature aging on the microstructural and mechanical properties of sputtered Zr–Ni–Al MG. Microstructurally, the TFMG remained amorphous after aging. We discovered that aging resulted in a 43% increase in the yield strength, from 1.81 ± 0.4 to 2.7 ± 0.2 GPa, and a 30% enhancement in the Young's modulus, from 69 ± 3 to 91 ± 4 GPa. 2. The hardening rate also increased by ~ 40% to 10 GPa after aging. Furthermore, both the as-sputtered and aged pillars with diameters less than 600 nm experienced homogeneous deformation, while those with larger diameters deformed via shear banding. We believe that the enhancement in mechanical properties is attributed to the microstructural relaxation that occurred within the MG. We also proposed to use the synchrotron XRD to verify this explanation. MD simulations were performed to provide a better understanding of the atomistic mechanisms for this aging phenomenon and will be discussed in the next chapter. Overall, the findings from this work provide a useful foundation for simple design of advanced materials whose mechanical properties can be predicted and prescribed a priori using physical principles of atomic-level relaxation.

Chapter 4. Molecular Dynamics Simulation Confirms Microstructural Relaxation

4.1. MD simulation methodology

4.1.1. Quenching simulations

MD simulations were employed to investigate the effect of relaxation on the mechanical behavior of Zr–Ni–Al MG and to identify associated microstructural changes. A simulation cube, shown in the inset of figure 4.1, was created with 53 Å sides and periodic boundary conditions in all dimensions. This simulation box was populated with a face centered cubic (FCC) lattice of Zr atoms. The Zr atoms were randomly replaced with Ni and Al atoms until the composition was nominally $Zr_{55}Ni_{25}Al_{20}$. This sample was immediately brought to a temperature of 2300 K and held under zero pressure boundary conditions for 10 ns under time integration of the isothermal- isobaric (NPT) ensemble where the amount of atoms (N), pressure (P) and the temperature (T) are conserved. All simulations were performed using an integration time step of 1 fs. Following liquid equilibrium, the sample was quenched down to 50 K at various quench rates of: 10^{10} K/s, 10^{11}K/s, 10^{12} K/s, and 10^{13} K/s. A plot of the potential energy as a function of temperature for various quench rates is shown in figure 4.1. Above 1125 K, all samples are in the liquid state and exhibit the same potential energy. Deviations in the potential energy start to emerge below 1125 K where the samples crossover their respective glass transition temperatures. As the quench rate increases, so does the potential energy.

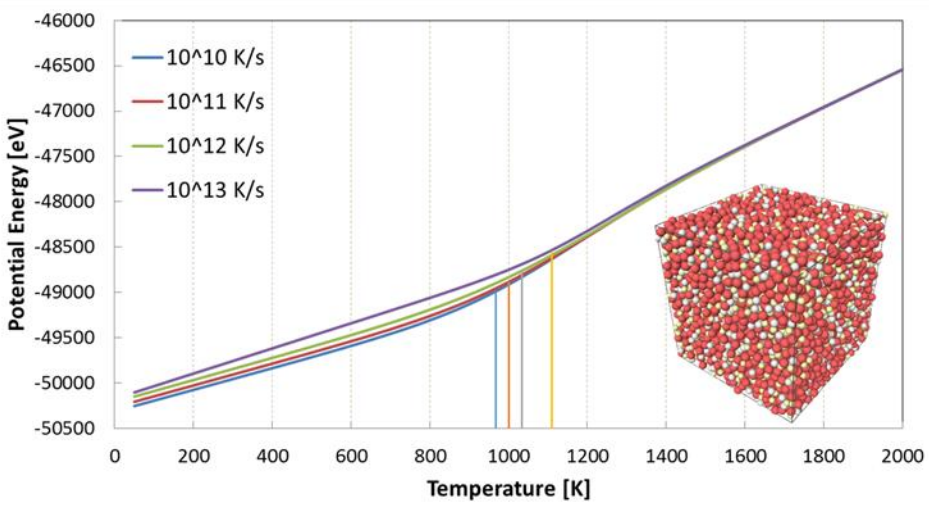

Figure 4.1. Effect of varying quench rate from 10^{10} K/s to 10^{13} K/s on the potential energy-temperature curves. Vertical lines correspond to the calculated glass transition temperature. Inset: Simulation cube of Zr–Ni–Al metallic glass.

The glass transition temperature (T_g) was determined by fitting the potential energy–temperature curves to the following function:

$$PE(T) = \big(1 - \varphi(T)\big) * (A_{solid} * T + B_{solid}) + \varphi(T) * \big(A_{liquid} * T + B_{liquid}\big) \tag{4.1}$$

$$\varphi(T) = \frac{1}{1 - \exp\left(\frac{T - T_m}{T_r}\right)} \tag{4.2}$$

This equation interpolates between the linear regimes of the potential energy–temperature curve at the high temperature (liquid) and low–temperature (solid) regimes. The slope and y-intercept of the linear fit for each regime is denoted by A and B, respectively. In equation 4.1, the first and second terms correspond to the solid and liquid regime, respectively. Each term is weighted by the interpolator, φ(T), which is the logistic function where T_r is the temperature span of the transition regime and T_m is the median temperature of the transition regime. The transition regime corresponds to the temperature range where the non-linearity occurs between the two solid and liquid regimes. The glass transition temperature (T_g) is then found as the temperature at which the MG enters into the solid

regime. From the PE curves, the T_g corresponds to the temperature when the solid regime deviates from non-linearity.

$$T_g = T_m - \frac{T_r}{2} \tag{4.3}$$

This definition is consistent with commonly used differential scanning calorimetry (DSC) measurements where T_g is taken as the beginning of an endothermic event when heating the sample from the solid regime[101,102]. This method is also a robust approach for comparing the T_g across different quench rates. A plot of the glass transition temperature as a function of quench rate is shown in figure 4.2. As the quench rate increases, the glass transition also increases.

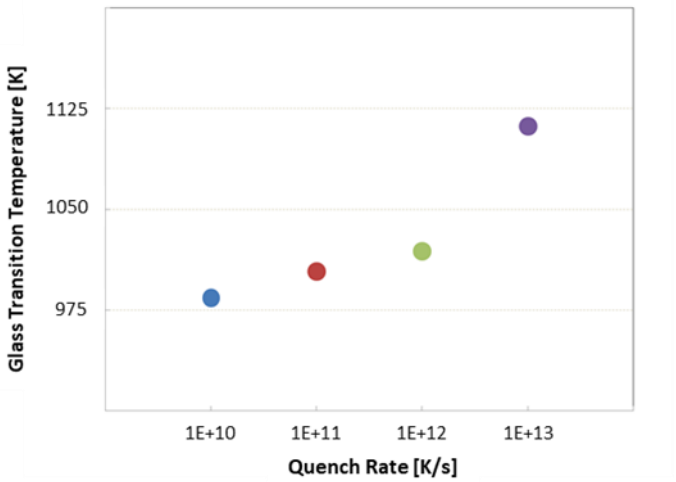

Figure 4.2. Effect of varying quench rate from 10^{10} K/s to 10^{13} K/s on the glass transition temperature.

4.1.2. Thermal annealing simulations

Annealing simulations were performed by bringing the quenched samples to 90% of their T_g and held under zero pressure boundary conditions using time integration of the NPT ensemble. To understand the effect of annealing time, the annealing simulations were performed for 0 ns, 100 ns, 200 ns, 300 ns, and 400 ns (as shown in figure 4.3 (a)). After annealing, the samples were quenched back down to 50 K at a quench rate of 10^{13} K/s. Since the second quenching was performed within

the solid regime, the high quench rate after annealing did not result in the rejuvenation of the relaxed state. The potential energy (shown in figure 4.3 (b)) for all samples shows a decrease within 100 ns of annealing. Beyond 100 ns, the 10^{12} K/s and 10^{13} K/s samples show no significant change in potential energy. However, 200 ns of annealing time are needed for the 10^{11} K/s sample to plateau. The potential energy curve of the 10^{10} K/s sample shows continuous decrease in energy for the entire length of the annealing. Overall, higher quench rates still exhibit higher potential energy for each of the respective annealing times.

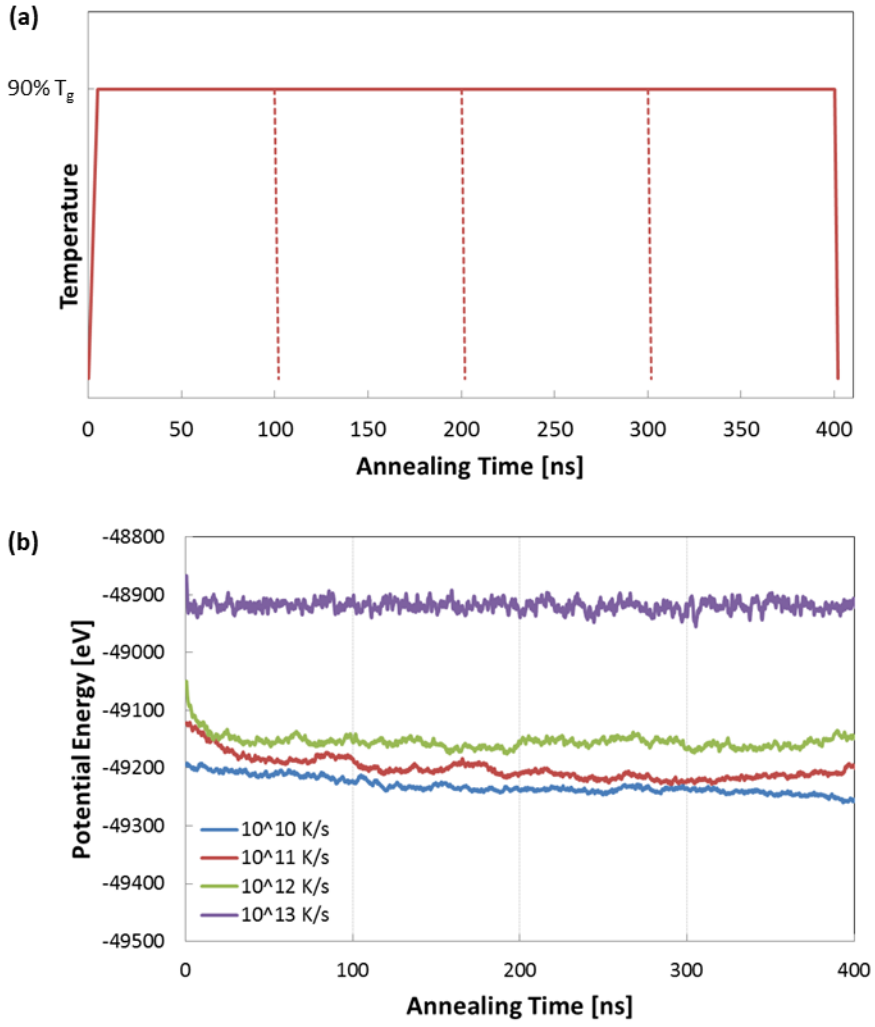

Figure 4.3. Annealing simulations for Zr–Ni–Al metallic glass. (a) Annealing at 90% T_g for various annealing times from 0 to 400 ns. (b) Effect of varying annealing time and quench rate on the average potential energy.

The dotted lines in figure 4.4 and figure 4.5 denote the potential energy pathway for each of the samples during the annealing step. For the 10^{10} K/s, 10^{11}K/s and 10^{12} K/s samples, rapid heating from low temperature follows the linear pathway with a slope equal to the solid (low–temperature) curve. This deviates from the quenched curve as we enter into the supercooled liquid regime. Annealing at a fixed temperature leads to an energy decrease with relaxation. After annealing, rapid cooling follows the same linear pathway but offsets by the energy gained from annealing.

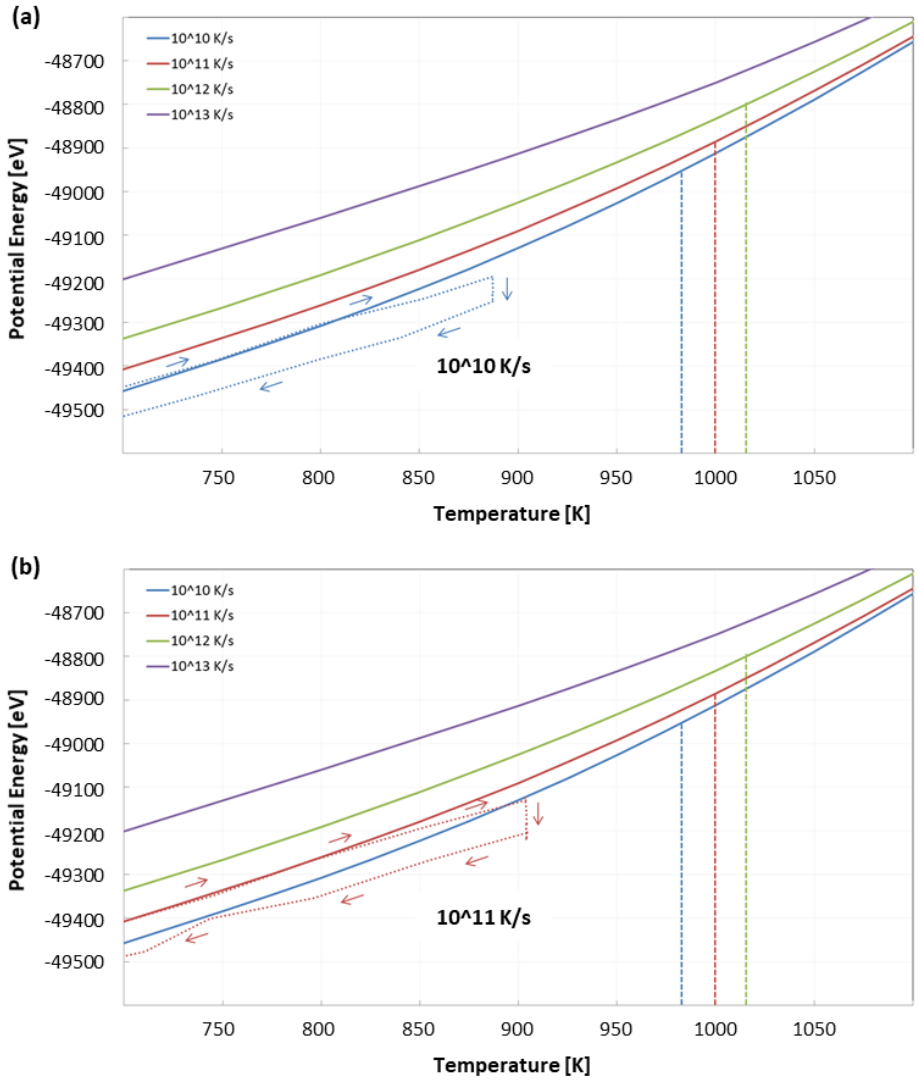

Figure 4.4. Potential energy pathways (denoted by dotted lines with arrow pointing along the direction of the pathway) for the (a) 10^{10} K/s and (b) 10^{11} K/s samples, which were annealed from 50 K to $0.9T_g$ and then quenched back to 50 K. For reference, the solid lines correspond to the same initial quenching curves shown in Figure 4.1.

For the 10^{13} K/s sample, it differs from the other samples in that its annealing curve does not follow its own low–temperature quenching curve. In fact, it quickly relaxes and even temporarily reaches below the 10^{10} K/s quench line. This shows that the sample has reached a highly relaxed state, which is consistent with the constant value of potential energy during annealing.

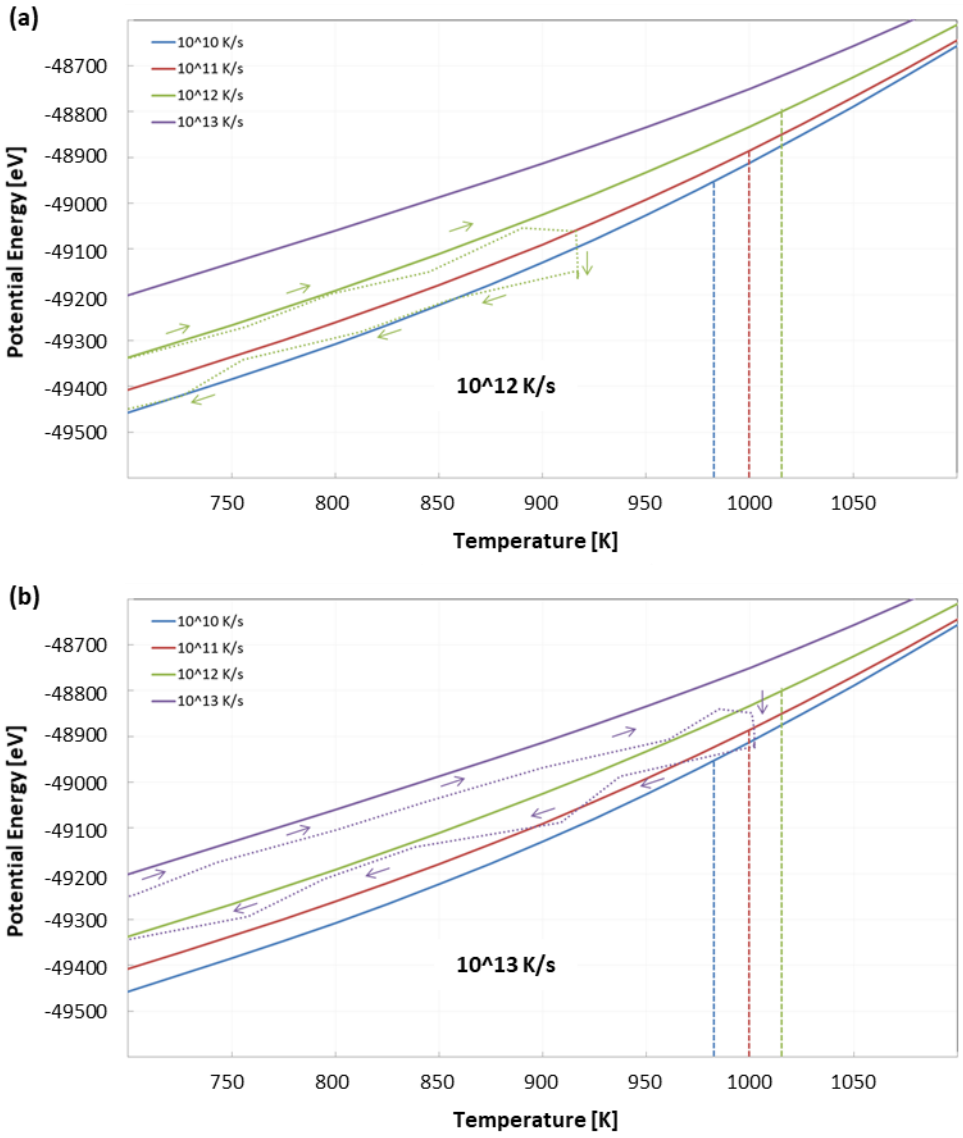

Figure 4.5. Potential energy pathways (denoted by dotted lines with arrow pointing along the direction of the pathway) for the (a) 10^{12} K/s and (b) 10^{13} K/s samples, which were annealed from 50 K to $0.9T_g$ and then quenched back to 50 K. For reference, the solid lines correspond to the same initial quenching curves shown in Figure 4.1.

4.1.3. Simulated Zr–Ni–Al nanowire

Using these initially cubic samples, nanowires were constructed by replicating the cubic samples in all dimensions and removing atoms to leave a cylindrical geometry with a diameter of 30.2 nm and height of 114.3 nm. The boundary condition in the axial dimension (i.e., z direction) was taken as periodic while the lateral dimensions were set as free surfaces. The nanowire sample was then brought to 300 K and held for 200 ps for equilibrium. Nanowires were constructed using samples from all quench rates and for both un-annealed and annealed samples. This resulted in a total of 20 simulated compression samples. Compression was then simulated by deforming the simulation box in the axial direction up to 12% total strain and at an engineering strain rate of 10^8 s^{-1}. Such a high strain rate is an unavoidable consequence of the time scales accessible during MD simulations and may over predict the initial yield strength in these samples.

All simulations were performed using the Large-Scale Atomic/Molecular Massively Parallel Simulator (LAMMPS) MD software[103]. To calculate the interatomic interactions, we employed an embedded atom model (EAM) potential parameterized for the Zr-Cu-Ni-Al system[104]. OVITO was used for the calculations of the atomic shear strain and visualizations[105]. Radical Voronoi analysis was performed on samples during quenching and post-annealing using the Voro++ software package[106]. The natural definition of NN in this MG is defined as atoms that share a face of a Voronoi polyhedron. The computed Voronoi index also provides a measure of local order in the MG.

Even though the EAM potential for the Zr-Cu-Ni-Al system was utilized, the results from the MD simulations are still relevant to our Zr-Ni-Al MG system. The substitution of Cu atoms for Zr atoms in the Zr-Ni-Al system promotes more efficient cluster packing structure of the amorphous alloys and leads to a pronounced increase in their glass-forming ability[107]. Sun et al. showed that by increasing the Cu atomic content from 17.5 % to 28%, the critical casting diameter improved from 6

mm to 14 mm[107]. However, the addition of Cu deteriorates the MG's oxidation resistance because Cu is a catalyst for the oxidation process[80,81]. However, in MD simulations, the simulation environment does not contain oxygen and thus, the effect of enhanced oxidation of Zr-Cu-Ni-Al is irrelevant. Fundamentally, the structural properties of the Zr-Cu-Ni-Al systems are similar to that of Zr-Ni-Al systems[108]. Thus, the atomistic mechanisms and trends that we observed in MD simulations are still valid and applicable for our Zr-Ni-Al systems.

4.2. Limitations of MD simulations

Although MD simulations are a powerful tool to reveal and understand the underlying physics of the material, it has some limitations. They require intensive computational resources, which makes it impractical to simulate the exact conditions used in experiments (i.e., lower strain rates, long term room temperature aging, and larger pillar sizes). Thus, MD simulations require making compromises in the spatial and temporal scale. For example, orders of magnitude higher strain rate of 10^{8} s^{-1} are used in simulation; compared to the experimentally lower strain rates of 10^{-3} s^{-1}. As a result, the higher strain rate typically results in a higher simulated yield strength. To achieve the relaxed microstructure, MD simulations relied on thermal annealing at $0.9T_g$ for up to 400 ns, which is significantly faster and at a higher temperature compared to the experimental process of room–temperature aging for 3 years.

Finally, the sample size of our simulated Zr–Ni–Al cylindrical pillar has a smaller volume than experimentally tested. The simulated samples had a diameter of 30.2 nm and a height of 114.3 nm, while experimental tested samples had diameters between 300 nm to 1.1 μm and heights between 900 nm to 3.3 μm, respectively. Despite these differences, MD simulations are still a reliable technique that provides insight into the overall mechanistic trends and deformation modes. For example, if the

MD simulations reveal similar mechanical properties or behavior as experimental results, we can utilize the simulations to understand and identify the associated microstructural changes in the samples.

4.3. Results and discussion

4.3.1. Voronoi tessellation

A common approach in MD simulations is to perform a Voronoi tessellation of the atomic configuration and identify frequently occurring coordination polyhedral as a measure of SRO. The polyhedron can be constructed between each atom and their NN to form triangular (i.e., threefold bonds), quadrangular (i.e., fourfold bonds), pentagonal (i.e., fivefold bonds) or hexagonal (i.e., sixfold bonds) faces. The total number of each type of bonds can be compiled together to form the Voronoi index. For example, a Voronoi index of <0,5,2,1> corresponds to zero threefold bond, five fourfold bonds, two fivefold bonds and one sixfold bond. Table 4.1 and figure 4.6 show the percentage of each type of Voronoi configurations found at 50 K for the corresponding quench rates. The top 5 most prevalent Voronoi configurations for each category (i.e., Zr–centered, Ni–centered, and Al–centered) are listed. Many other Voronoi configurations do exist but they have significantly lower percentages and are not reported. Thus, for a given quench rate and category (i.e., Zr–centered, Ni–centered, and Al–centered), the percentages do not add up to 100%. These percentages are calculated for the quenched sample in the as-quenched state (i.e., before annealing).

Results indicate that Ni and Al serve as the centers for high local packing with Zr atoms filling in the intermediate spacing. No single Zr–centered configuration is found to occur at more than 6.4% of all Zr atoms. Decreasing the quench rate shows an increase in high packing density configurations for Ni– and Al–centered configurations. Notably, they are the following configurations: <0,1,10,5>

configuration for Zr, <0,2,8,0> for Ni, <0,2,8,2> and <0,0,12,0> for Al. All other configurations are negligibly impacted by quenching rate.

Table 4.1. Percentage of each type of Voronoi configuration found at 50 K for the corresponding quench rates in the as–quenched state.

Zr-Centered	10^{10} K/s	10^{11} K/s	10^{12} K/s	10^{13} K/s
<0,1,10,5>	6.36%	6.26%	5.15%	4.88%
<0,2,8,5>	5.45%	5.28%	4.74%	4.79%
<0,2,8,6>	5.46%	5.00%	5.07%	5.02%
<0,1,10,4>	4.70%	4.18%	4.29%	4.59%
<0,3,6,6>	3.81%	3.20%	2.85%	3.06%
Ni-Centered	10^{10} K/s	10^{11} K/s	10^{12} K/s	10^{13} K/s
<0,2,8,0>	23.02%	20.71%	19.37%	18.06%
<0,3,6,1>	15.78%	16.31%	15.57%	15.15%
<0,3,6,0>	15.37%	15.07%	15.26%	14.35%
<0,2,8,1>	12.49%	11.42%	11.72%	11.79%
<1,3,3,3>	3.95%	3.78%	4.03%	3.51%
Al-Centered	10^{10} K/s	10^{11} K/s	10^{12} K/s	10^{13} K/s
<0,2,8,2>	18.50%	18.94%	17.53%	16.21%
<0,0,12,0>	14.66%	14.68%	12.27%	10.83%
<0,3,6,3>	8.57%	7.65%	8.44%	7.78%
<0,2,8,1>	8.03%	7.25%	7.91%	8.07%
<0,1,10,2>	7.77%	6.27%	6.72%	6.93%

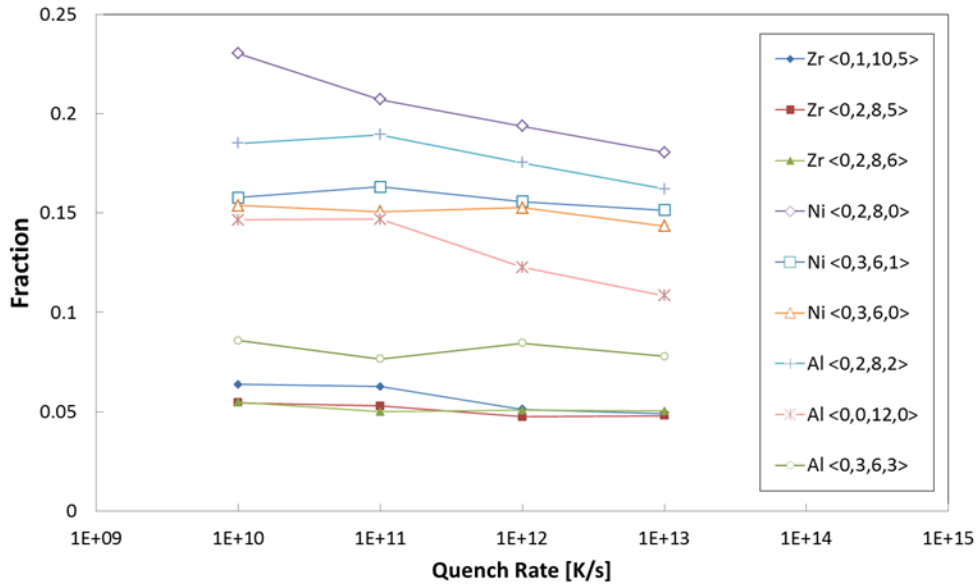

Figure 4.6. Fraction of each Voronoi configuration found at 50 K plotted against various quenching rates for the as-quenched state.

After annealing for 400 ns and re-quenching down to 50 K, the Voronoi analysis was performed again to determine the fractional change in the energetically favorable Voronoi configurations. For a direct comparison, we have focused on the same set of Voronoi configurations that was used in the as-quenched state. Table 4.2 displays the percentage of each Voronoi configuration after 400 ns of annealing. The up or down arrows correspond to their respective increase or decrease of that specific Voronoi configuration after annealing. The percentage from the as-quenched simulation is denoted in the parenthesis.

Table 4.2. Percentage of each type of Voronoi configuration found after 400 ns of annealing at $0.9T_g$. The up or down arrows correspond to their respective increase or decrease of that specific Voronoi configuration after annealing. The percentage from the as-quenched simulation is denoted in the parenthesis.

Zr-Centered	10^{10} K/s	10^{11} K/s	10^{12} K/s	10^{13} K/s
<0,1,10,5>	↑ 6.77% (6.36%)	↑ 7.03% (6.26%)	↑ 6.44% (5.15%)	↑ 5.59% (4.88%)
<0,2,8,5>	↑ 5.56% (5.45%)	↑ 6.02% (5.28%)	↑ 5.31% (4.74%)	↑ 5.12% (4.79%)
<0,2,8,6>	↑ 5.56% (5.46%)	↑ 5.27% (5.00%)	↑ 5.63% (5.07%)	↓ 4.86% (5.02%)
<0,1,10,4>	↑ 4.83% (4.70%)	↑ 5.17% (4.18%)	↑ 4.77% (4.29%)	↓ 4.38% (4.59%)
<0,3,6,6>	↓ 3.15% (3.81%)	↑ 3.37% (3.20%)	↑ 3.34% (2.85%)	↑ 3.26% (3.06%)
Ni-Centered	10^{10} K/s	10^{11} K/s	10^{12} K/s	10^{13} K/s
<0,2,8,0>	23.02% (23.02%)	↑ 23.05% (20.71%)	↑ 21.96% (19.37%)	↑ 20.77% (18.06%)
<0,3,6,1>	↑ 16.45% (15.78%)	↓ 15.64% (16.31%)	↑ 16.50% (15.57%)	↑ 15.38% (15.15%)
<0,3,6,0>	↑ 15.61% (15.37%)	↑ 15.48% (15.07%)	↑ 15.90% (15.26%)	↑ 15.52% (14.35%)
<0,2,8,1>	↓ 12.33% (12.49%)	↑ 12.23% (11.42%)	↓ 11.51% (11.72%)	↓ 11.47% (11.79%)
<1,3,3,3>	↓ 3.91% (3.95%)	↑ 4.55% (3.78%)	↓ 3.64% (4.03%)	↓ 3.20% (3.51%)
Al-Centered	10^{10} K/s	10^{11} K/s	10^{12} K/s	10^{13} K/s
<0,2,8,2>	↓ 17.85% (18.50%)	↑ 20.29% (18.94%)	↑ 20.03% (17.53%)	↑ 18.85% (16.21%)
<0,0,12,0>	↑ 16.20% (14.66%)	↑ 16.33% (14.68%)	↑ 15.05% (12.27%)	↑ 11.30% (10.83%)
<0,3,6,3>	↓ 8.10% (8.57%)	↑ 7.81% (7.65%)	↑ 8.75% (8.44%)	↑ 8.33% (7.78%)
<0,2,8,1>	↑ 8.15% (8.03%)	↑ 7.57% (7.25%)	↓ 7.45% (7.91%)	↓ 7.25% (8.07%)
<0,1,10,2>	↓ 6.23% (7.77%)	↓ 6.24% (6.27%)	↓ 6.41% (6.72%)	↑ 7.60% (6.93%)

These results indicate that there is an increase in a majority of the low-energy atomic configurations for all sample sets. More specifically, we can focus on three Voronoi configurations: Zr <0,1,10,5>, Ni <0,2,8,0>, and Al <0,2,8,2>. The fraction of these Voronoi configurations as a

function of annealing time is plotted in figure 4.7. These plots confirm that most of the configurations tend to increase with the amount of annealing time.

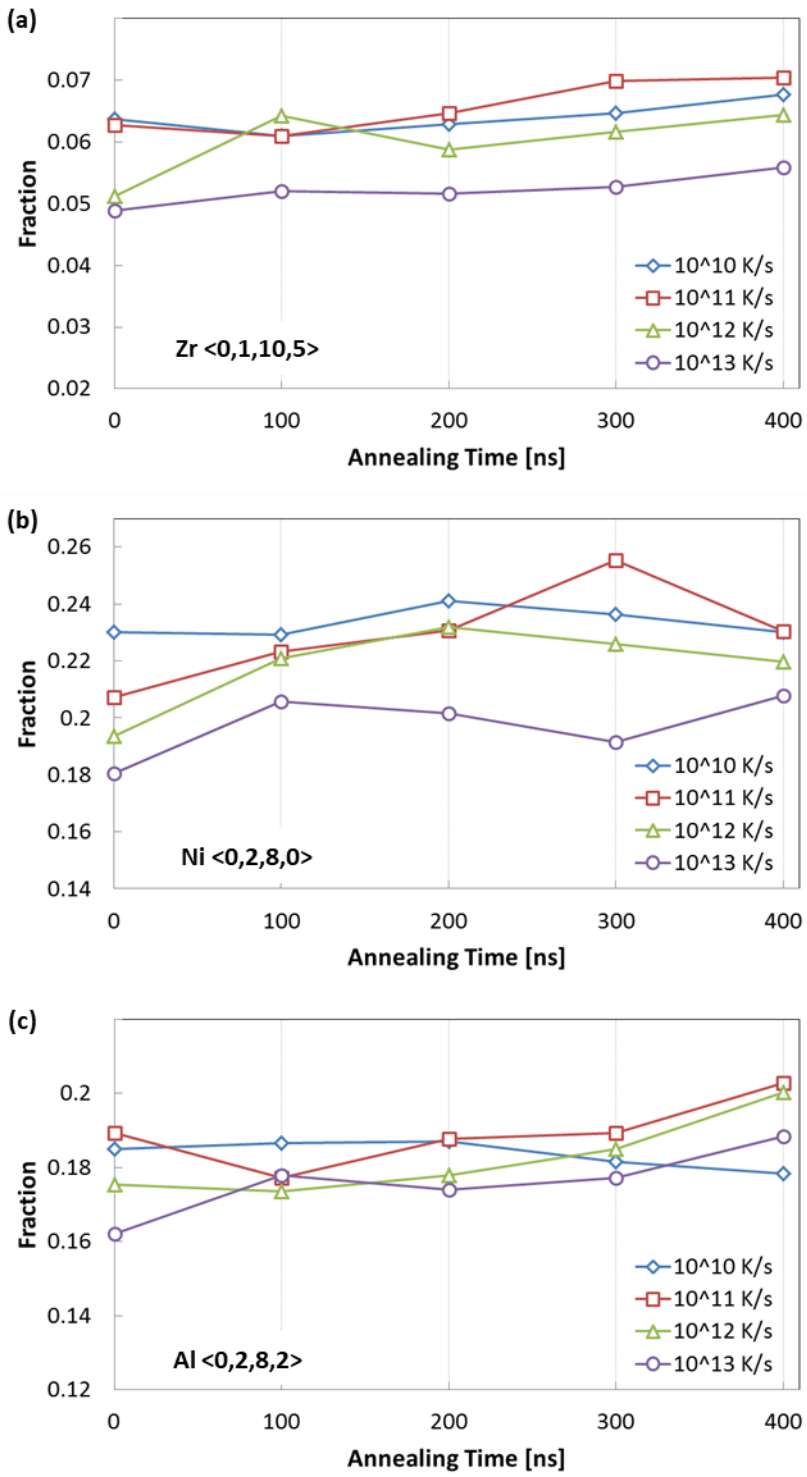

Figure 4.7. Fraction of (a) Zr <0,1,10,5>, (b) Ni <0,2,8,0>, and (c) Al <0,2,8,2> Voronoi configuration as a function of annealing time for various quench rates (10^{10} K/s to 10^{13} K/s).

4.3.2 Warren–Cowley analysis

Voronoi analysis shows the local SRO, but does not account for the type of neighboring atoms. Computation of the Warren–Cowley (WC) parameter provides a quantitative measure of the chemical SRO and indicates the correlation of the first NN pairs. Assuming that we have a central atom of type *A* with a NN of type *B*, the WC parameter is defined as:

$$\alpha_{AB} = 1 - \frac{Z_{AB}}{Z_A x_B} \tag{4.4}$$

where Z_{AB} is the number of *B*-type NN atoms around an *A*–type atom, Z_A is the total coordination number around an *A*–type atom, and x_B is the atomic fraction of *B*–type atoms in the alloy. A WC parameter of 0 indicates that the NN bonds between atom types *A* and *B* are random; while a negative WC parameter indicates a preference for NN bond formation. A positive WC parameter indicates that those NN bonds are avoided.

Table 4.3 presents the Warren–Cowley analysis for the as-quenched Zr-Ni-Al sample. The tables are organized based on their quenching rates. The rows indicate the central atom type and the columns specify the NN shell atom type (i.e., for α_{AB}, *A* corresponds to rows and *B* corresponds to columns). The colors blue and red correspond to negative WC parameters (i.e., like to be neighbors) and positive WC parameters (i.e., dislike to be neighbors), respectively. The intensity of each color corresponds to its magnitude.

A plot of the WC parameters as a function of quench rate is shown in figure 4.8. The results indicate that a decrease in quench rate leads to a moderate increase in α_{Ni-Ni} and α_{Al-Al} with a corresponding moderate decrease in α_{Ni-Zr} and α_{Al-Zr}. This is in agreement with the observations from the Voronoi analysis where the increase in ordered, highly packed Ni– and Al–centered clusters occurred with decreasing quench rates.

Table 4.3. Warren–Cowley analysis for the as-quenched Zr–Ni–Al sample. Tables are organized based on their quenching rates. Top left: 10^{10} K/s; Top right: 10^{11} K/s; Bottom left: 10^{12} K/s; Bottom right: 10^{13} K/s.

10^{10} K/s	Zr	Ni	Al
Zr	-0.052	0.117	-0.0004
Ni	-0.379	0.862	-0.017
Al	-0.312	0.147	0.676

10^{11} K/s	Zr	Ni	Al
Zr	-0.052	0.118	-0.0008
Ni	-0.378	0.845	-0.001
Al	-0.313	0.158	0.665

10^{12} K/s	Zr	Ni	Al
Zr	-0.058	0.127	0.004
Ni	-0.367	0.825	-0.007
Al	-0.309	0.152	0.661

10^{13} K/s	Zr	Ni	Al
Zr	-0.065	0.133	0.016
Ni	-0.353	0.790	-0.0004
Al	-0.294	0.155	0.616

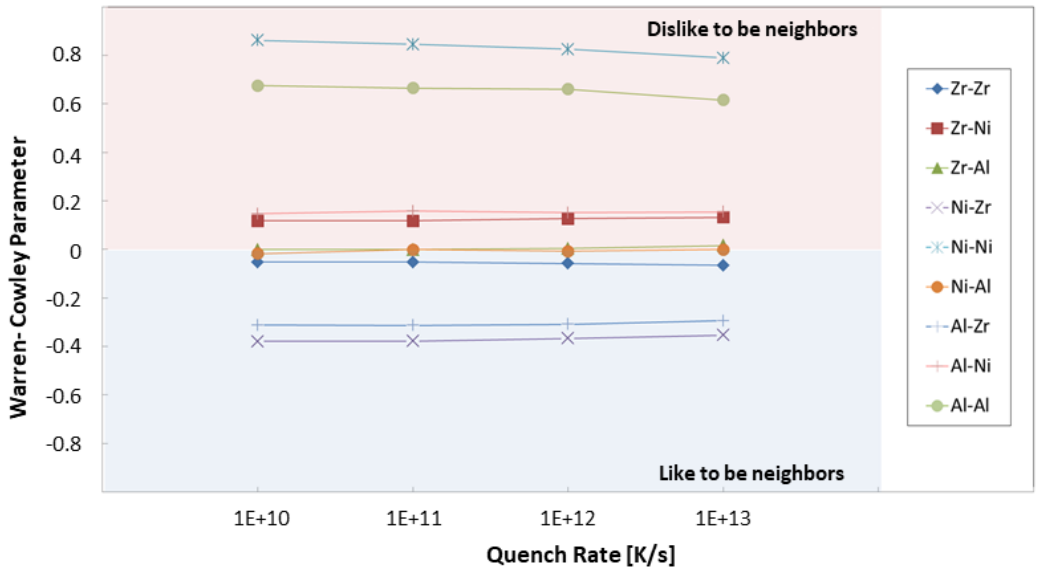

Figure 4.8. Warren–Cowley parameter as a function of quench rate for the as–quenched Zr–Ni–Al sample.

After annealing, the Warren–Cowley analysis was performed again to determine the change in bonding preference. The plots of the WC parameter for the Ni–Ni and Al–Al bonds as a function of annealing times and quenching rates are shown in figure 4.9. The Ni–Ni and Al–Al bonds, which dislike to be neighbors, both show an increasing WC parameter with increasing annealing time. Notably, the increase in WC parameters for Al–Al bonds appears to proceed at the same rate even after 400 ns of annealing (for 10^{10} and 10^{11} K/s samples). This suggests that Al atoms are continuing to spread themselves apart.

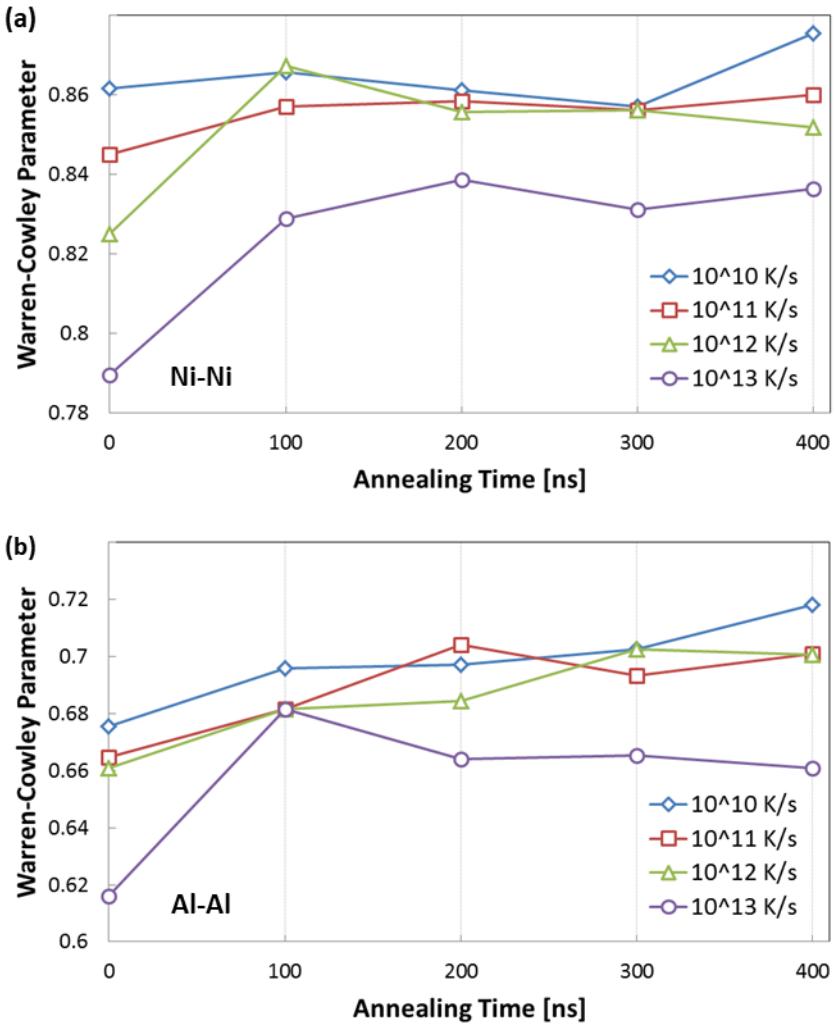

Figure 4.9. Warren–Cowley analysis for (a) Ni–Ni bonds and (b) Al–Al bonds as a function of annealing times and quenching rates.

The plots of the WC parameter for the Ni–Zr and Al–Zr bonds as a function of annealing times and quenching rates are shown in figure 4.10. Both types of bonds, which prefer to be neighbors, show a decreasing WC parameter with increasing annealing time. Also, the decrease in WC parameter for the Al–Zr bonds appears to be proceeding at the same rate even after 400 ns of annealing (for 10^{10} and 10^{12} K/s samples). Thus, Al atoms are continuing to increase their Zr bonding.

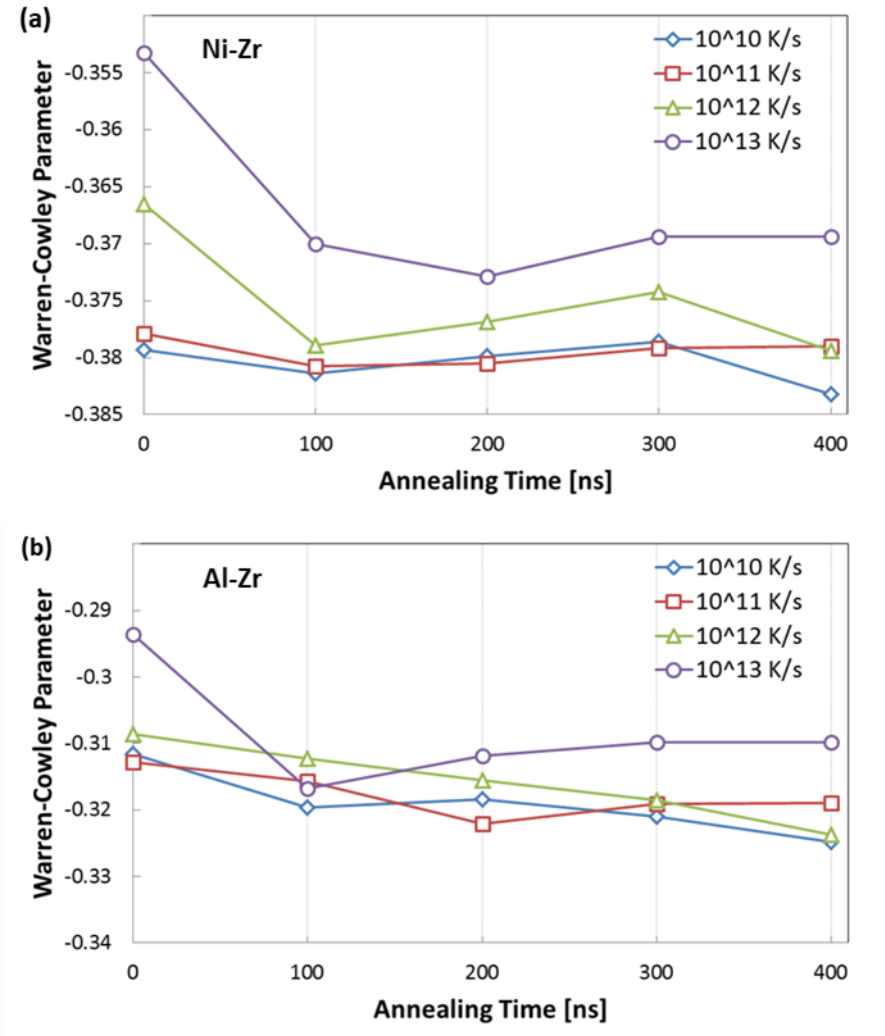

Figure 4.10. Warren–Cowley analysis for (a) Ni–Zr bonds and (b) Al–Zr bonds as a function of annealing times and quenching rates.

4.3.3 Fivefold bonding

Numerous studies have shown that 5-fold symmetries have the highest local symmetry and can be correlated to the amount of atomic relaxation in MG[109–112]. For example, <0,0,12,0> is a regular dodecahedron with 12 NN atoms organized in a full–icosahedron cluster. It is found in Cu–Zr binary MG systems and correlates positively with strength and negatively with average atomic energy. This concept is analogous to crystalline Frank–Kasper alloys where the ordered motifs that comprise of the Frank-Kasper phases are the polytetrahedral clusters that maximize 5-fold bonding under 12, 14, 15, and 16 coordination[113]. Thus for our simulated $Zr_{55}Ni_{25}Al_{20}$ MG, we tracked the amount of 5-fold symmetries as a function of varying quench rates and annealing times.

Figure 4.11 depicts an example ensemble of atoms taken from one of our simulated samples. From the Voronoi analysis, the two atoms of interest (colored red) are defined as neighbors when they share a face of the Voronoi tessellation (indicated by the red bond). The bonds between the five NN atoms and the two atoms of interest are depicted with gray bonds. Thus, the red bond is referred to as a "fivefold bond" because the bonded atoms share five neighbors.

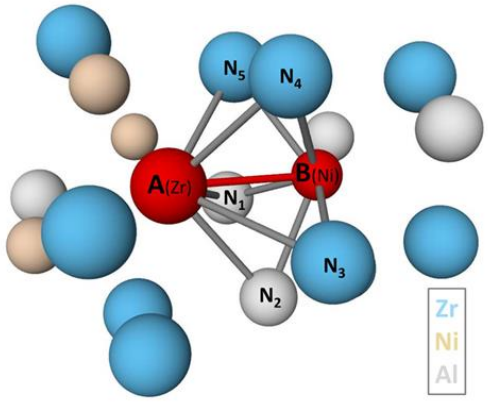

Figure 4.11. A schematic fivefold bond (denoted by the red bond) where the two red atoms share 5 neighbors (indicated by gray bonds).

The relationship between quench rate and fivefold bonding is shown in the figure 4.12. For all atomic species, it is observed that the average number of fivefold bonding increases with decreasing quench rate. Also, there is significantly more Zr and Al fivefold bonds than Ni fivefold bonds. This is consistent with the Warren–Cowley analysis where there is a greater presence of Zr–Ni and Zr–Al bonds compared to Ni–Ni bonds.

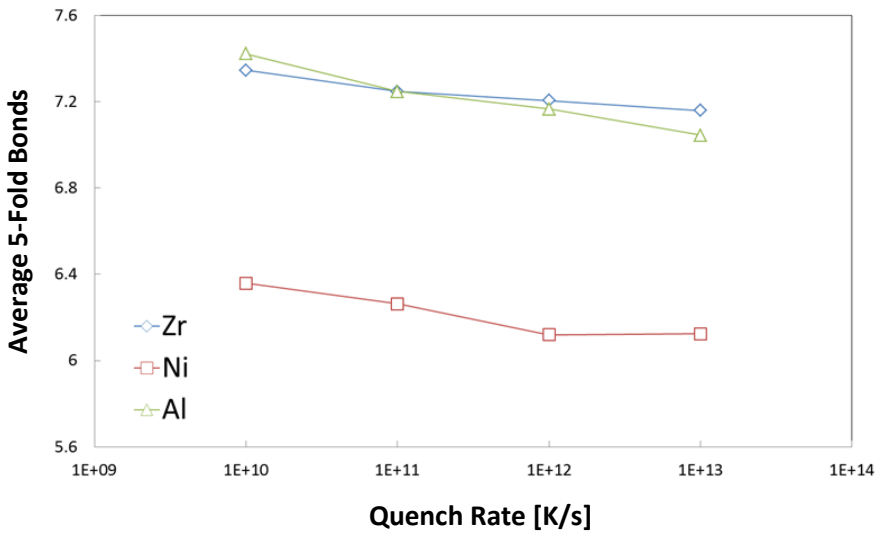

Figure 4.12. Average number of fivefold bonds as a function of quench rates for the as-quenched Zr-Ni-Al sample.

Analogous to the icosahedral configurations in the binary Cu–Zr system, figure 4.13 (a) shows the system-wide average number of fivefold bonds as a function of annealing time. As observed with the potential energy, both the 10^{11} K/s and 10^{12} K/s samples approach similar amounts of fivefold bonding as the 10^{10} K/s sample during annealing. The sample prepared with a quench rate of 10^{13} K/s shows a modest increase in the average number of fivefold bonds with annealing. The plot in figure 4.13 (b) shows a clear correlation where increasing the amount of fivefold bonding results in a decrease of the potential energy in the Zr–Ni–Al MG. These data points include all quench rates and annealing times. It shows that the energy relaxation observed during annealing can be chiefly attributed to atoms

from low density, high-energy configurations (Voronoi configurations with few fivefold bonds) relaxing to high–density, low–energy configurations (Voronoi configurations with many fivefold bonds).

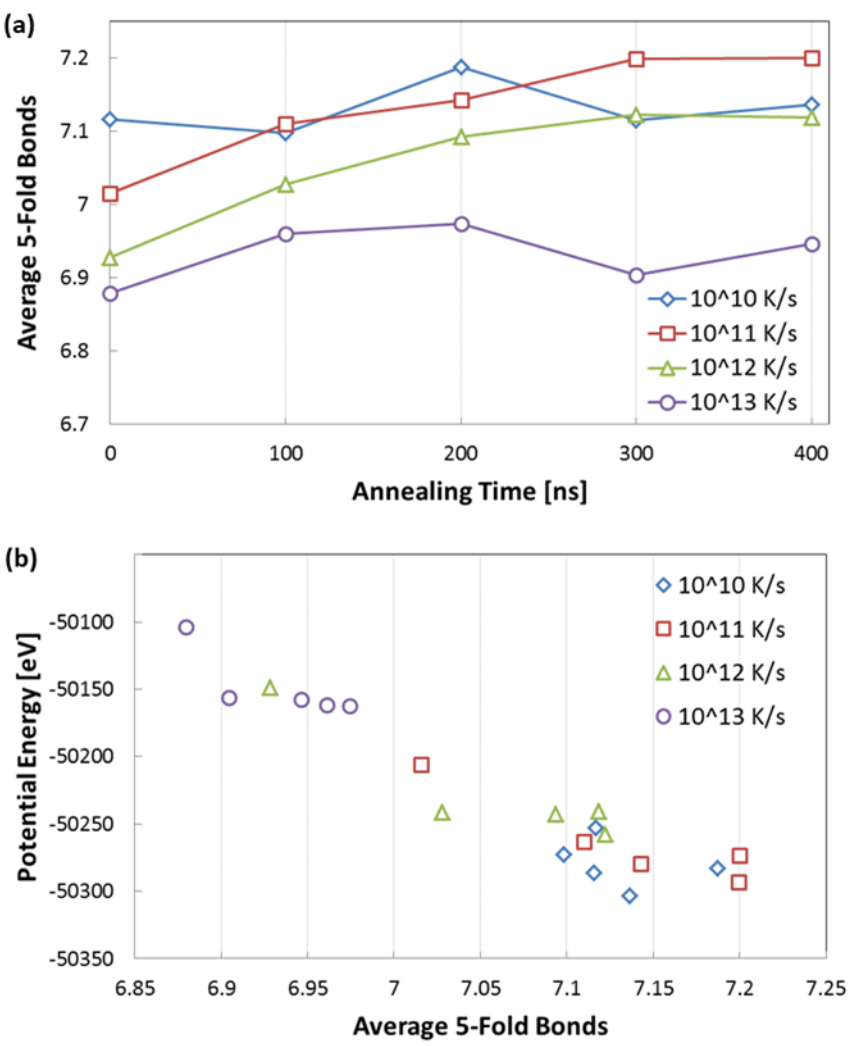

Figure 4.13. Correlation between the average number of fivefold bonds versus (a) annealing time and (b) potential energy for all quenching rates.

4.3.4 Simulated compression of Zr–Ni–Al nanowire

Simulated compressions of Zr–Ni–Al nanowires were performed to understand the mechanical properties and deformation mechanisms. The stress-strain curves for nanowires that were quenched at various cooling rates and annealed for various times are shown in figure 4.14. In particular,

the sample that was quenched at 10^{13} K/s and not annealed is displayed in gray. The stress–strain curve follows an initially linear elastic regime, and then yields into a nearly–perfectly plastic regime with a maximum stress of 1.72 GPa (indicated by the gray star in figure 4.14). Samples that were both quenched at a slower rate or had been annealed (denoted in various shades of red in figure 4.14) show both an increased slope in the elastic regime as well as an increase in maximum stress. The maximum stress of the sample that was quenched at 10^{10} K/s and annealed for 400 ns (curve displayed in red) reached a maximum stress of 3.40 GPa (indicated by the red star in figure 4.14). Yielding was accompanied by the buckling of the nanowire and was attributed to the periodic boundary conditions in the axial direction and the free surface boundary conditions in the lateral directions. Maximum stress and yielding typically occurred between 0.06–0.07 strain, with subsequent deformation proceeding by continued bending of the buckled morphology. Thus, the relevant stress–strain data is only shown up to 0.08 strain.

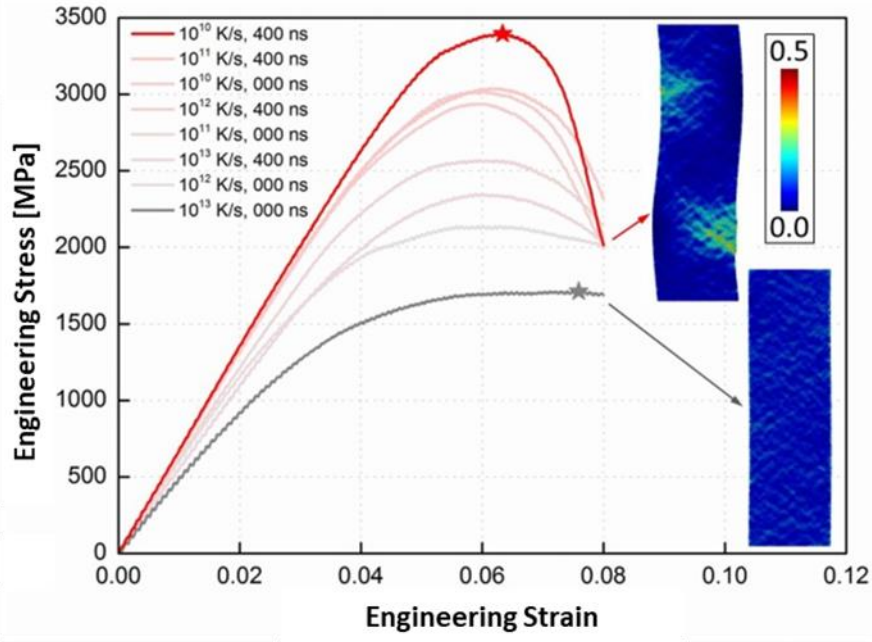

Figure 4.14. Summary stress-strain plot of simulated compression of a $Zr_{55}Ni_{25}Al_{20}$ nanowire. The red curve indicates a sample that was initially quenched at 10^{10} K/s and subsequently annealed for 400 ns. The gray curve indicates a sample that was initially quenched at 10^{13} K/s and was not annealed. Insets show the deformed nanowires colored by atomic shear strain. Several stress-strain curves from intermediately relaxed samples are included for comparison.

The two insets in figure 4.14 show the nanowire at 0.08 strain for two samples: (1) a sample quenched at 10^{10} K/s followed by annealing for 400 ns (red arrow) and; (2) another sample that was quenched at 10^{13} K/s without annealing (gray arrow). The color gradient depicts the amount of atomic shear strain of each atom. The nanowire constructed from a sample quenched at 10^{13} K/s without annealing showed that the deformation was distributed homogeneously throughout the entire sample. In contrast, the nanowire constructed from a MG quenched at 10^{10} K/s and then annealed for 400 ns showed that the deformation was localized to regions of high shear strain near surfaces of high compressive stress resulting from the buckled configuration.

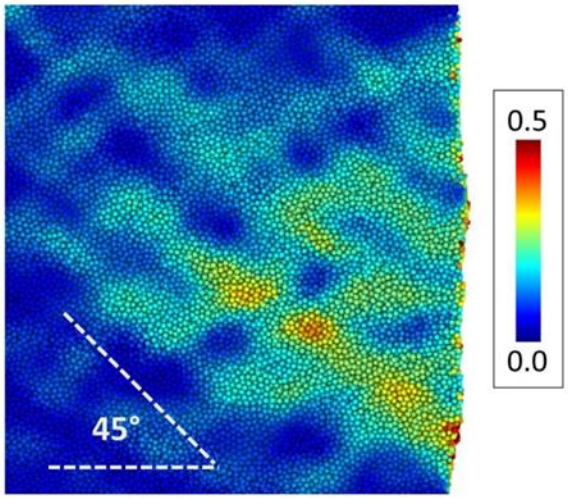

Figure 4.15. A close-up of the sample initially quenched at 10^{10} K/s and subsequently annealed for 400 ns at 0.8 shear strain. Atoms are colored by their atomic shear strain. Shear planes nucleate from the surface and propagate into the wire at an angle of ~45° with respect to the nanowire axis.

Figure 4.15 displays a close-up view of the sheared region. This region displays shear band-like characteristics with several sheared regions oriented approximately 45° from the nanowire axis. The simulated stress-strain behavior and the atomic shear strain snapshots indicate that strengthening and a transition from homogeneous to localized deformation occurred with decreasing quench rates and increasing annealing time. These mechanistic features are indicative of microstructural relaxation within the MG where groups of atoms rearrange into high–density, lower–energy clusters. Numerous

models have provided an atomic basis for the mechanical properties in MG; focusing on several indicators of the internal microstructural state[114–117].

The aging-induced relaxation reported here was also observed in similar TFMGs that were annealed at elevated temperatures[1]. There are many similarities between both relaxation mechanisms and possibly, may have similar origins. At elevated temperatures, as seen during annealing, $\alpha-$ relaxation dominates and the relaxation occurs via hopping between the megabasins on an experimental time scale. Below the glass transition temperature, $\beta-$relaxation dominates and the relaxation occurs chiefly on the scale of the SRO. This is analogous to relaxation of the SRO described in our MD simulations. For a sufficiently long period of time (i.e., three years of room–temperature aging), several successive $\beta-$relaxation events could lead to a relaxation state similar to a single $\alpha-$ relaxation event. Sputtered MGs, which have low density and high free volume, can be considered as lying in a higher potential energy basin and thus, have a greater probability of making a basin jump through smaller $\beta-$relaxation events.

Figure 4.16 demonstrates the relationship between the average number of fivefold bonds per atom versus the Young's modulus and the maximum compressive stress. The maximum compressive stress is determined as the maximum stress from the simulated compression of the Zr-Ni-Al nanowire. For example, gray and red stars in figure 4.14 denote the maximum compressive stress for the sample quenched at 10^{13} K/s and the sample quenched at 10^{10} K/s followed by annealing for 400 ns, respectively. It demonstrates that with the increasing number of fivefold bonds, there is an increase in both mechanical properties. Experimentally, we also observed significant improvements in both the Young's modulus and yield strengths. Thus, we attribute the microstructural relaxation through the increase in the number of fivefold bonds as one of the mechanisms for the enhancements in

mechanical properties. Due to the high strain rates of MD simulations, we can only compare the mechanistic trends and cannot accurately compare the absolute values of these simulated results with our experimental data. Although this correlation of the strength with fivefold bonding was observed for all samples, SRO is likely not a complete description of the relaxation state of the MG. Medium–range order also emerges with relaxation, but unfortunately there is no clear quantitative measure of medium-range order for this system.

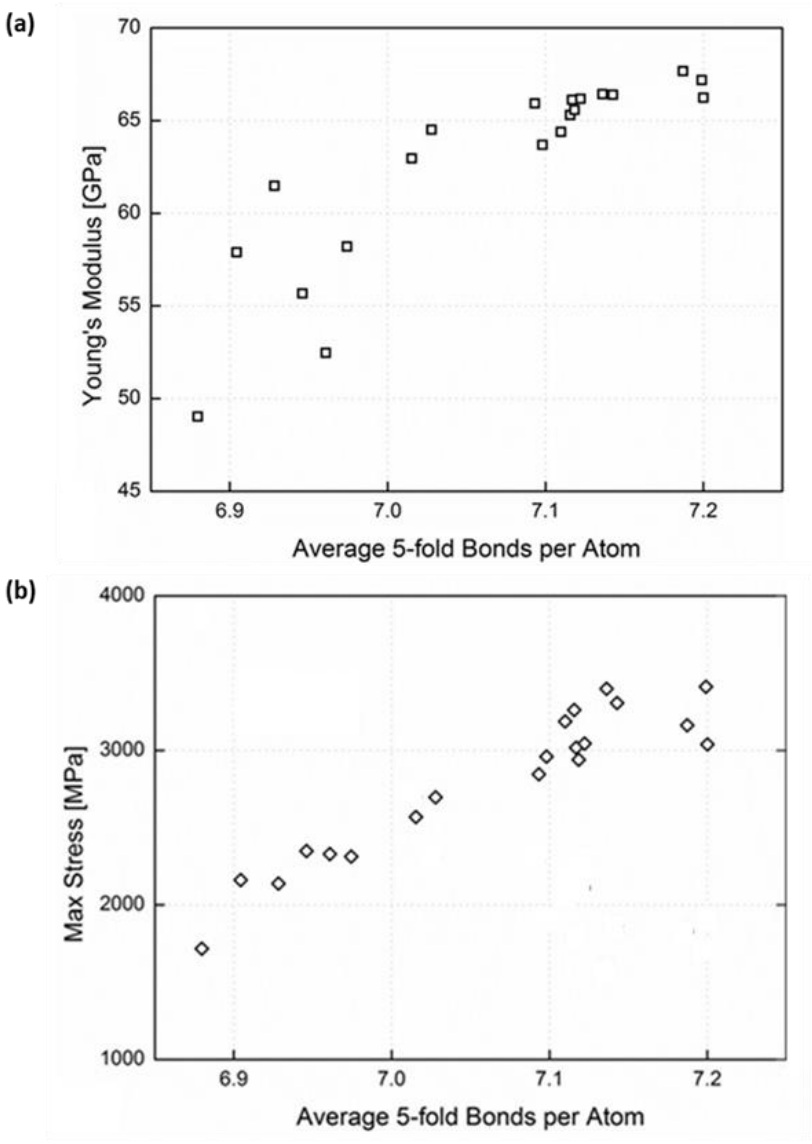

Figure 4.16. Correlation between the average number of fivefold bonds versus (a) Young's modulus and (b) maximum compressive stress.

4.4 Summary

MD simulations were performed for $Zr_{55}Ni_{25}Al_{20}$ alloy at various quench rates between 10^{10} to 10^{13} K/s. Voronoi analysis showed that increasing SRO occurred with decreasing quench rate. Furthermore, computation of the WC parameter indicated that Ni and Al atoms were randomly distributed and had a preference for Zr in their NN shells.

Thermal annealing was performed at 90% of their respective T_g for various times from 0 ns to 400 ns. Samples that were prepared at elevated quench rates (10^{11}–10^{13} K/s) experienced a rapid decrease in potential energy within the first 100 ns of annealing time. The potential energy of the 10^{11} K/s and 10^{12} K/s samples approached the potential energy of the 10^{10} K/s sample after 100 ns of annealing and plateaued. While, the potential energy of the 10^{13} K/s sample remained steady after the initial decrease during the first 100 ns of annealing. Annealing led to an increase in the most high-density, low-energy atomic configurations. This relaxation is observed as an increase in the number of fivefold bonds, which has been shown to be a good structural indicator of potential energy.

MD simulations demonstrated that relaxation moves towards a state of increased fivefold bonds (higher polytetrahedral packing). This relaxation predicts higher strength and localized deformation under compression. At the atomic scale, relaxation does not distinguish between annealing and aging. This conclusion agrees well with our experimental observation that room–temperature aging of sputtered MG results in significant increase in strength and Young's modulus.

Chapter 5. Dynamic Mechanical Analysis Reveal Hydrides in Zr–Ni–Al

5.1. Motivation

DMA is a useful technique to provide insight into the viscoelastic properties by studying the perturbations of atomic motions from an applied oscillatory load. This load can vary in frequency, temperature or both frequency and temperature. These mechanical vibrations reveal a material's damping properties and its ability to dissipate elastic strain energy. Under quasi–static pillar compression, we have demonstrated that aging improved the strength and Young's modulus of the sputtered Zr–Ni–Al MG. We turn to DMA to explore how aging affected the material's damping properties. In particular, focusing on the loss modulus since it represents the internal friction and quantifies the energy dissipation within the material.

5.2. Room–temperature DMA

5.2.1. Low frequency DMA

DMA was conducted between the frequency range of 2 to 600 Hz. We categorized the low frequency data to be between 2 to 10 Hz; while the high frequency data lies between 300 to 600 Hz. A plot of the loss modulus as a function of frequency for the as-sputtered and aged Zr–Ni–Al MG is shown in figure 5.1 The colors blue and red correspond to the as-sputtered and aged Zr–Ni–Al, respectively; while the color gradient from dark to light corresponds to pillar sizes from small to large,

respectively. For each sample, three pillar diameters were investigated: 600 nm, 850 nm, and 1000 nm. The data points are the experimentally measured loss modulus, while the solid horizontal line is the calculated average loss modulus for a specific pillar diameter. A summary of the loss modulus for each sample and pillar diameter is shown in table 5.1. Overall, the loss modulus for the as-sputtered samples ranged from 0.29 GPa to 0.75 GPa, while the loss modulus for the aged samples ranged from 0.67 GPa to 1.17 GPa. We observed that the loss modulus increased after aging. From MD simulation, the aging phenomenon reduced the free volume in the MG, which increased the local SRO and the cluster sizes of the atoms. These larger clusters have higher internal friction between the atoms and as a result, increase the loss modulus.

Additionally, it is observed that the loss modulus increases with decreasing pillar diameter. This is attributed to the difference in surface area to volume ratio where smaller diameter pillars have larger surface area to volume ratio than larger diameter pillars. The atoms at the surface of the pillar contain broken bonds and cannot form clusters with high local symmetries. In contrast, the atoms that are in the middle of the pillar can form full icosahedra with its neighboring atoms. The lack of full icosahedra on the surfaces means that it is a structurally liquid and thus, the atoms are in a highly disordered state. When a sinusoidal load is applied, energy loss through the surface becomes dominant and the loss modulus increases.

Table 5.1. Summary of the average loss modulus for the as-sputtered and aged Zr–Ni–Al for pillar diameters: 600 nm, 850 nm, and 1000 nm

	Average Loss Modulus	
Pillar Diameter (nm)	**As- Sputtered MG**	**Aged MG**
~ 600	**0.75** ± 0.05	**1.17** ± 0.11
~ 850	**0.62** ± 0.06	**0.8** ± 0.05
~ 1000	**0.29** ± 0.02	**0.67** ± 0.03

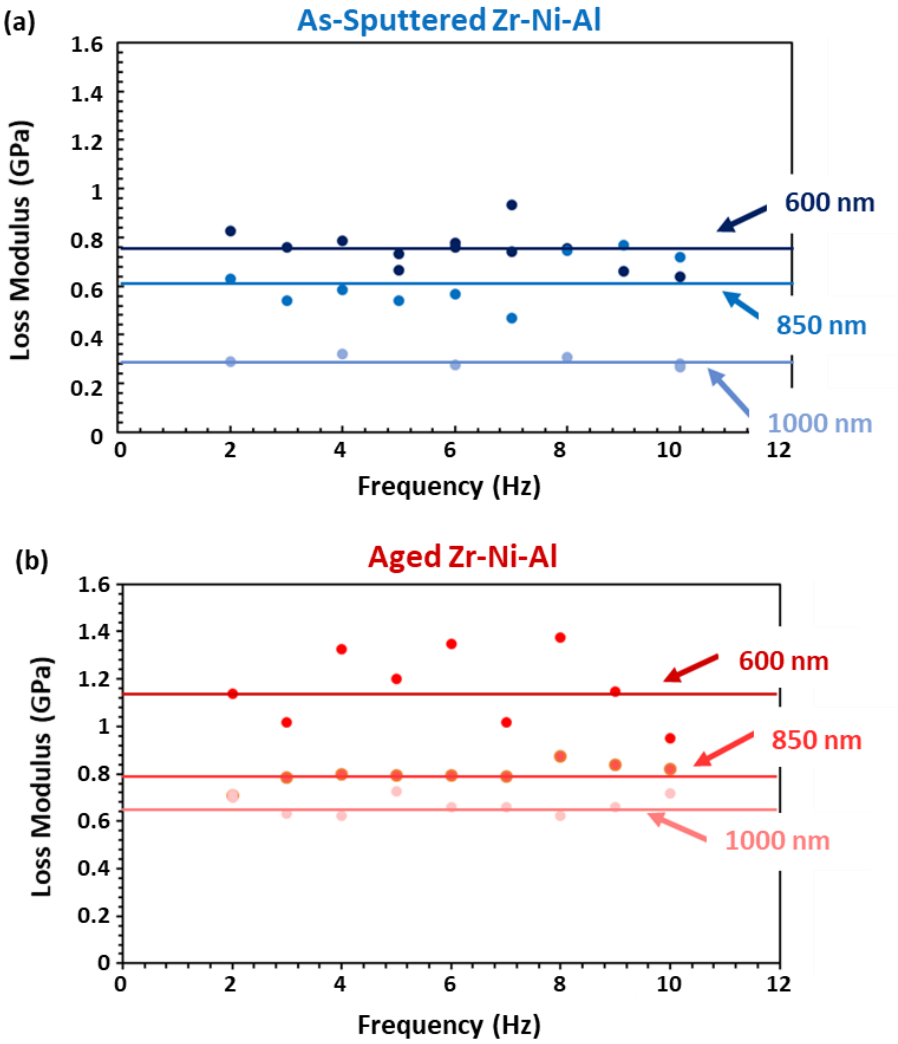

Figure 5.1. Loss modulus as a function of frequency for (a) as-sputtered and (b) aged Zr–Ni–Al MG. For each sample, three pillar diameters were investigated: 600 nm, 850 nm, and 1000 nm. The data points are the experimentally measured loss modulus, while the solid horizontal line is the calculated average loss modulus for a specific pillar diameter.

5.2.2. High frequency DMA

Besides the low frequency studies, a detailed frequency scan was conducted up to 600 Hz (experimental measurements were taken every 5 Hz). The underlying trends that were observed in the low frequency range persisted throughout most of the higher frequency range. However, at around 450 Hz, we encountered a peak in the loss modulus. Figure 5.2 displays the loss modulus peak for the

as–sputtered and aged Zr–Ni–Al sample. The table on the right of each plot summarizes the loss modulus at the peak frequency for each pillar size. In the aged sample, the peak frequency of 450 Hz is very consistent, while in the as-sputtered sample, the peak frequency varies linearly with the sample diameter. Furthermore, for both samples, the loss modulus is dependent on the size of the pillar (i.e., larger pillars exhibited a higher loss modulus).

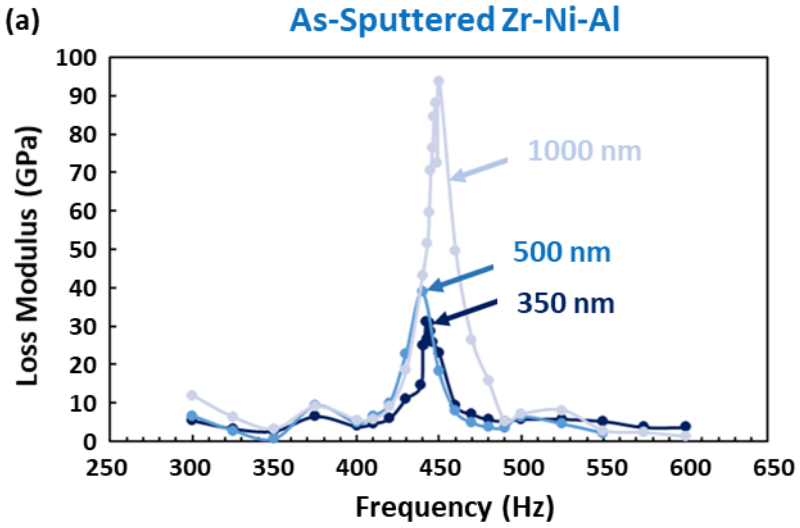

Pillar Diameter (nm)	Peak frequency (Hz)	Peak Loss Modulus (GPa)
350	442	31.1
500	440	38.8
1000	450	93.7

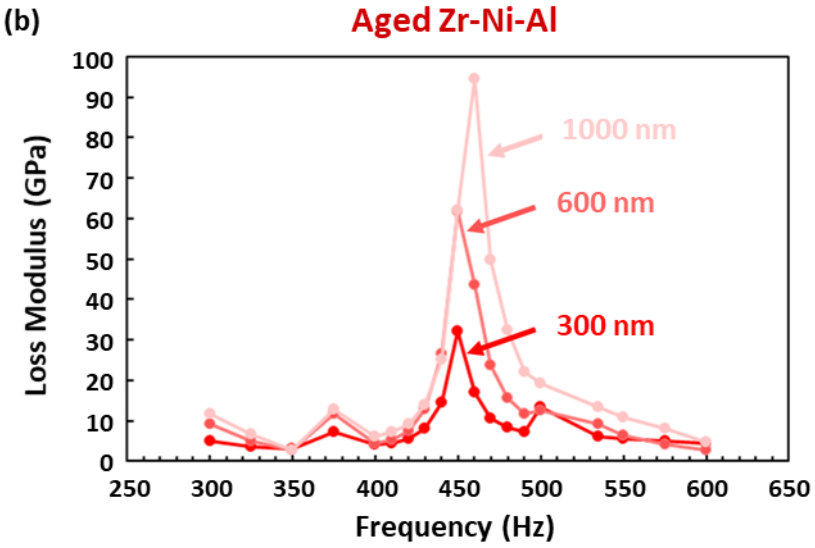

Pillar Diameter (nm)	Peak frequency (Hz)	Peak Loss Modulus (GPa)
300 nm	450	32.1
600 nm	450	61.5
1000 nm	452	96.9

Figure 5.2. Loss modulus peak for the (a) as-sputtered and (b) aged Zr–Ni–Al MG. The table on the right of each plot summarizes the loss modulus at the peak frequency for each pillar size.

To explain the physical meaning of this peak, we referred to previous studies on the internal friction measurements of amorphous metals. Hazelton et al. measured the internal friction of amorphous Zr_2PdH_x and observed a broad peak, which was attributed to a distribution of activation energies for hydrogen hopping[118]. Christensen et al. studied the site occupation of the hydrogen–zirconium system and reported that interstitial hydrogen atoms tend to preferentially occupy tetrahedral sites[119]. The calculated enthalpies of formation ranged from -7.8 kJ/mol to -53.7 kJ/mol for Zr_4H and ZrH_2, respectively, which suggests that hydride formation with zirconium is energetically favorable[119]. We hypothesize that the observed peak in loss modulus corresponds to the activation of hydrogen mobility within our material. Due to the sputtered (i.e., high free volume) and amorphous nature of our thin–film, hydrogen diffusion and hydride formation with zirconium and nickel atoms is readily occurring.

There are two possible sources of hydrogen. First, hydrogen could have come from the dissociation of atmospheric water molecules. Ni has been demonstrated to be an effective catalyst for the dissociation of water[120,121]. The dissociated hydrogen atom can diffuse deeper into the MG material to form hydrides. Second, trace amounts of hydrogen in the sputtering chamber could have contributed to the formation of hydrides in MG. Even though the sputtering chamber was pumped down to 10^{-6} Torr before deposition, gas analysis on the residual pressure demonstrates that trace amounts of hydrogen exists[84].

With this interpretation, the observed trends in the peak loss modulus can be now be clarified. Figure 5.3 shows the plots of peak loss modulus and the corresponding frequency as a function of pillar diameter. For the aged Zr–Ni–Al, the consistent peak frequency of 450 Hz suggests that the hydride in the aged sample is more–uniformly distributed and possibly trapped at a lower–energy state compared to the as-sputtered sample. Hydrides in the as-sputtered sample have a range of activation

frequencies, from 440 to 450 Hz, where some hydrogen atoms are weakly bonded in the interstitial sites, while others are more–strongly bonded[122,123]. Thus, the activation frequency is independent for the aged Zr–Ni–Al, but is size dependent for the as–sputtered Zr–Ni–Al. For the as- sputtered Zr–Ni–Al, the loss modulus ranged from 31.1–93.7 GPa for pillar diameters between 300 nm–1 μm. Whereas for aged Zr–Ni–Al, the loss modulus ranged from 32.1–96.9 GPa for the same pillar diameter range. In both samples, the loss modulus increases as a function of pillar diameter. Since the loss modulus is a direct measurement of the hydride mobility, the larger pillars have more interstitial sites which can accommodate higher amounts of hydrides than smaller pillars. Thus, we observe an increase in the loss modulus[122,124].

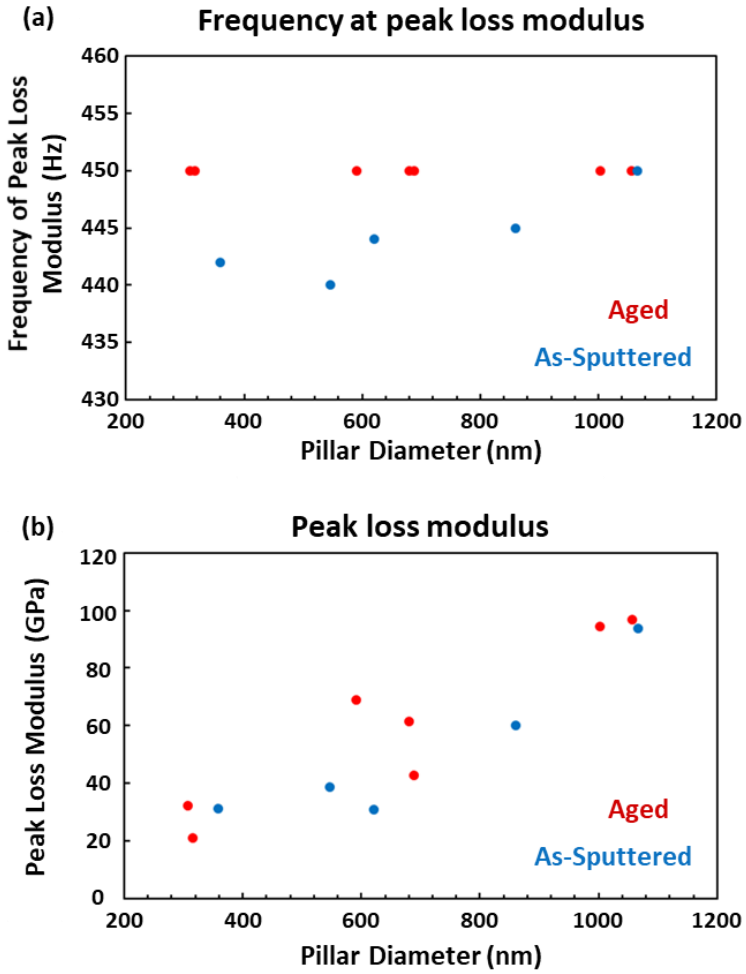

Figure 5.3. (a) The frequency of the loss modulus peak and (b) the value of the peak loss modulus as a function of pillar diameter for the as-sputtered and aged Zr–Ni–Al MG.

5.3. Hydrides in sputtered Zr–Ni–Al

It is worth exploring the effect of hydrides on the microstructure and mechanical properties of MGs. Berry et al. studied the an–elastic relaxation of Ni–Zr bulk MG and observed a connection between the host–atom diffusion and the presence of hydrogen[125]. Specifically, the introduction of hydrogen accelerates the relaxation behavior of host atoms, which is called hydrogen-enhanced host diffusion[125]. For sputtered MG, the as-sputtered micron-thick film on the silicon substrate experienced residual stress as a result of the deposition process[67]. This stress provided the energy for the redistribution of the host–atoms, which led to the microstructural relaxation and increase in SRO. After aging, we believe that the relaxed thin film has significantly less residual stress. Combining the contributions from the residual stress (that originated from the deposition process) and the propensity for hydride formation, we can expect that the rate of aging to be enhanced for sputtered Zr–based MG. Thus, the mechanical properties (i.e., Young's modulus and yield strength) of aged Zr–Ni–Al MG are higher than that of as–sputtered.

5.4. High temperature DMA

DMA at elevated temperatures of 360 K were also conducted on the aged Zr-Ni-Al MG. Figure 5.4 plots the loss modulus for two pillar diameters: 600 nm (green) and 1000 nm (yellow). The lower frequencies between 2–10 Hz are shown in figure 5.4 (a) with the average loss modulus denoted by the solid line, while the higher frequencies between 300–600 Hz are shown in figure 5.4 (b). The intermediate frequencies between 10-300 Hz exhibit similar loss modulus as those in the lower frequencies (i.e., 2-10 Hz). At low frequencies, the average loss modulus for the 600 nm and 1000 nm diameter pillars are 1.41 ± 0.05 GPa and 0.88 ± 0.09 GPa, respectively. At high frequencies, the loss

modulus peak (which corresponds to the activation of hydrogen mobility) remained at 450 Hz for both pillar diameters. The loss modulus for the 600 nm and 1000 nm diameter pillars are 25.9 GPa and 39.2 GPa, respectively.

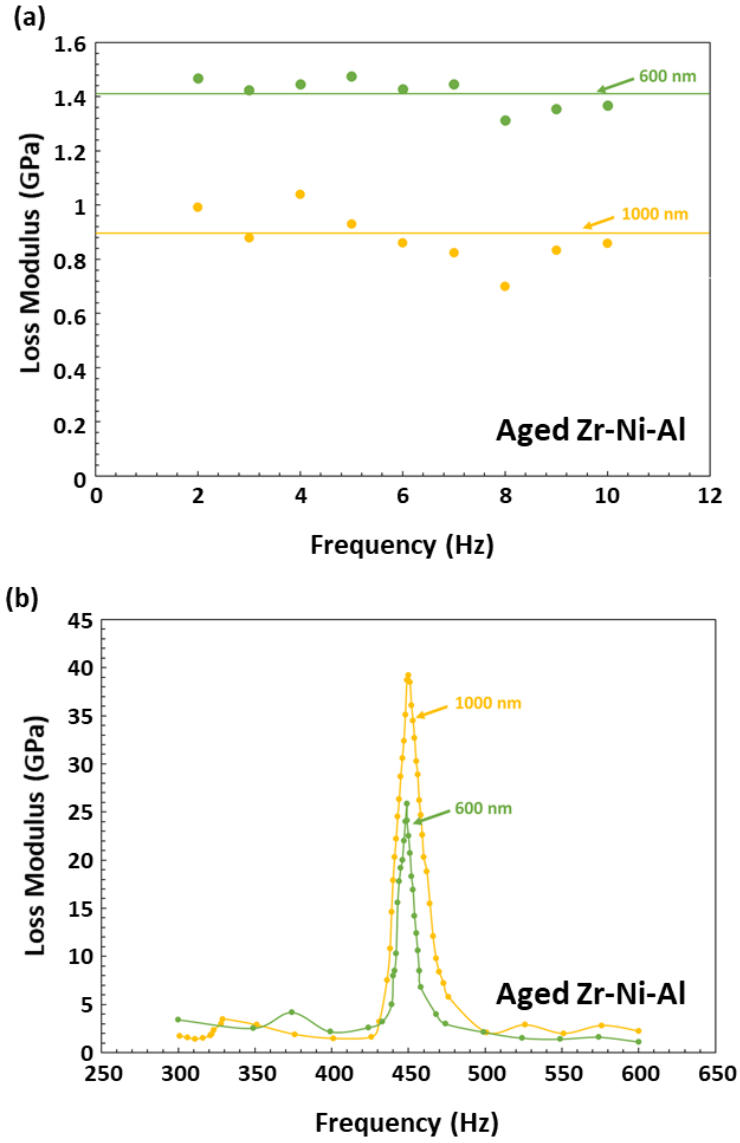

Figure 5.4. At 360 K: Loss modulus as a function of frequency for aged Zr-Ni-Al in the (a) low frequency regime: 2–10 Hz and (b) high frequency regime: 300–600 Hz. Two pillar diameters were investigated: 600 nm (green) and 1000 nm (yellow). For the low frequency plot, the data points are the experimentally measured loss modulus, while the solid horizontal line is the calculated average loss modulus for a specific pillar diameter.

At low frequencies, the loss modulus is higher for smaller pillars than larger pillars. This is similar to the results from room temperature DMA and is attributed to the varying surface area to volume ratio of different diameter pillars. The atoms at the surface of the pillar contain broken bonds and cannot form clusters with high local symmetries. Thus, the loss modulus is larger for smaller sized pillars. For any given pillar diameter, the loss modulus is higher at elevated temperatures than at room temperature. This is attributed to two factors : (1) the strength of the pinning centers of icosahedral atomic clusters are weaker at higher temperatures and (2) diffusive atomic motions occur more readily at high temperatures[126]. Thus, the internal friction increases and the loss modulus is higher. In the high frequency regime, the peak in loss modulus at 450 Hz is also detected at 360 K. The loss modulus for both pillars are lower than their respective values at room temperature. For the given pillar size, there are less hydrides in the pillar due to hydrogen desorption at higher temperatures.

5.5. Summary and Outlook

DMA was utilized to provide a better understanding of the relaxation dynamics in MG. At low frequencies, we observed that the loss modulus increased after aging and that smaller pillars exhibited higher loss modulus than larger pillars. At the high frequencies, the loss modulus peak at around 450 Hz was attributed to the activation of hydrogen mobility within the MG host matrix. The formation of hydride within zirconium and nickel tetrahedral have been studied extensively and demonstrated to occur readily in bulk. The presence of hydrides promotes host–atom diffusion so that more–mobile atoms, like Ni and Al, can rearrange and access lower potential energy state.

To confirm the presence of hydrogen and its distribution within our sample, we can turn to resonant nuclear reaction. It is a is a non-destructive hydrogen measurement technique that was first published by Leich and Tombrello and involves the use of a high energy nuclei beam (i.e., nitrogen-15) to bombard the sample under investigation (schematic of the experimental setup is shown in figure 5.5 (a))[127,128]. If hydrogen is present, a nuclear reaction under resonant conditions will occur and result in the emission of gamma radiation. One common reaction is 15N(1H,αγ)12C (equation 5.1) and is schematically shown in figure 5.5 (b):

$$^{15}N + {}^{1}H \rightarrow {}^{12}C + \alpha + \gamma\ (4.43\ MeV) \qquad (5.1)$$

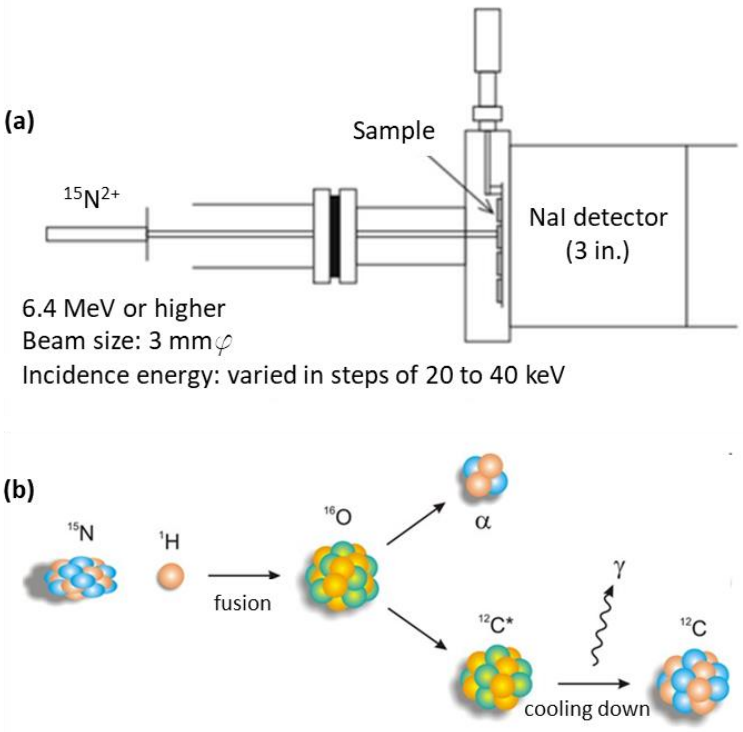

Figure 5.5. Schematic diagram for resonant nuclear reaction. (a) Experimental setup used to detect the hydrogen concentration profile as a function of depth; (b) Schematic diagram of the nuclear reaction $^{15}N(^{1}H,\alpha\gamma)^{12}C$.

At the resonance energy (6.38 MeV), the yield of the characteristic gamma radiation (4.43 MeV) will be proportional to the number of hydrogen atoms at the surface of the sample. When the energy

of nitrogen-15 is increased, the hydrogen on the sample surface is no longer detected because the energy lies above its resonance. While passing through the sample, nitrogen-15 loses energy and reaches the resonance energy at a characteristic depth. Thus, the yield of gamma ray is proportional to the hydrogen content at this depth. In this experiment, the hydrogen concentration profile can be determined by measuring the gamma ray yield versus the energy of the nitrogen-15.

Our DMA experiments focused on sweeping the frequency range of 2-600 Hz at fixed temperatures of 300 K and 360 K. It would also be useful to perform a temperature sweep from room temperature to T_g where we can capture the α – relaxation peak and also, observe the shift in loss modulus peak (for the activation of hydride). Currently, our experimental setup is limited to a maximum of 360 K because at higher temperatures, the thermal drift between the indenter tip and MG pillar dominates such that it becomes difficult to maintain consistent contact and to obtain accurate results. Thus, future work includes developing a higher temperature nanoindenter system that minimizes thermal drift. The characteristic frequency for the activation of hydride mobility may follow an Arrhenius behavior:

$$f = f_0 exp\left(\frac{E}{k_B T}\right) \tag{5.2}$$

where f is the frequency of the peak loss modulus and E is the activation energy of the mobility of hydrides. A plot of ln(f) versus 1/T can be constructed using the peak frequency for each temperature. The activation energy is determined from the slope of the curve. Comparing our calculated activation energies with literature will provide insight into the types of hydride (i.e., Zr_4H, Zr_2H, Zr_4H_3, ZrH, etc.) we have in our aged Zr-Ni-Al. Similarly, these experiments and analysis can be performed for the as-sputtered Zr-Ni-Al where we expect to find a larger variation in hydride types.

Chapter 6. Quasi-Static Uniaxial Pillar Compression at Cryogenic Temperatures

6.1. Motivation

In the previous chapters, we studied the characteristics of MG at room temperature and above. In this chapter, we will investigate whether sputtered Zr–Ni–Al MG can potentially be a good material for components used under extreme low temperature environments. Previous studies have shown that cryogenic temperature could reduce the atom mobility[129,130], alter the dynamic behavior of shear banding[131–133], improve the yield strength and increase plasticity of MG[129,134]. Thus far, no work has been reported on the effect of cryogenic temperatures on aged and sputtered MG. We have already demonstrated that aging leads to substantial enhancement of the MG's mechanical properties at room temperature. Thus, we seek to gain a better understanding of the atomic structure evolution in the low temperature regime and to understand its effect on the mechanical properties. To achieve this goal, we performed quasistatic uniaxial pillar compression experiments at cryogenic temperatures.

6.2. Nanomechanical compression results

6.2.1. Validation of nanomechanical testing methods

In Chapter 3, the quasi–static uniaxial pillar compressions that we reported were conducted using a Hysitron PI-85 pico–indenter, which is a different indenter from the one that was used for the cryogenic experiments. Our cryo–mechanical experimental setup (i.e., SEMentor) consists of a SEM

(Quanta SEM, FEI Co.) combined with a nano–indenter (InSEM, Nanomechanics, Inc.) and a cryogenic assembly by Janis Research Company. Thus using SEMentor, we first performed room–temperature uniaxial pillar compressions on the aged Zr–Ni–Al to establish a baseline and to compare the results with those obtained using Hysitron PI-85. Figure 6.1 shows the stress–strain curves for pillar compressions performed using SEMentor and Hysitron PI-85. Two representative curves for each testing method is plotted. Both methods produced very similar stress-strain curves with consistent Young's modulus (90 GPa) and yield strengths (2.6 GPa); thus, validating our testing procedure. Beyond the yield point, the deformation signature appears to differ between the two methods. This is due to the type of feedback control used for each testing setup (i.e., Hysitron utilizes load control while SEMentor utilizes displacement rate control).

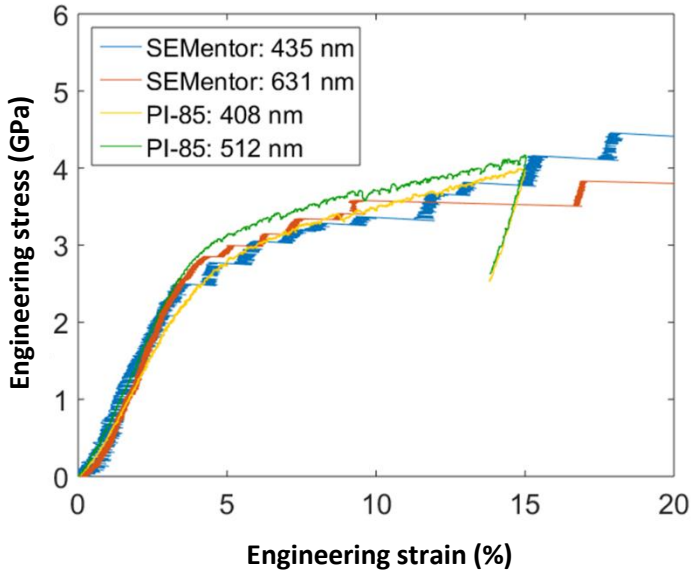

Figure 6.1. Stress–strain curves for pillar compressions performed using SEMentor and Hysitron PI-85. Sample: Aged Zr–Ni–Al metallic glass

6.2.2. Cryogenic nanomechanical compression results

Uniaxial pillar compression on aged Zr–Ni–Al pillars were performed at 140 K (using liquid nitrogen) and compared to the room–temperature (RT) experiments. Figure 6.2 is a plot of the stress–strain curves for the aged sample tested at 140 K (red and blue curves) and at room temperature (green and yellow curves). At 140 K, the stress–strain curves reveal the existence of a linear elastic regime, followed by minimal serrated flow and then, catastrophic brittle failure. This brittle failure occurred for all samples tested at 140 K. While for the RT compression tests, we observed more–significant serrated flow and shear banding. SEM images of a representative 700 nm pillar before and after compression at 140 K are shown in figure 6.3. Consistent with the stress-strain data, these pillars deform via multiple shear bands that travelled down the pillar at an angle of 45°. At 140 K, the Young's modulus and yield strength substantially increased from 90 ± 5 GPa to 326.4 ± 9.2 GPa and from 2.6 ± 0.2 GPa to 3.3 ± 0.2 GPa, respectively.

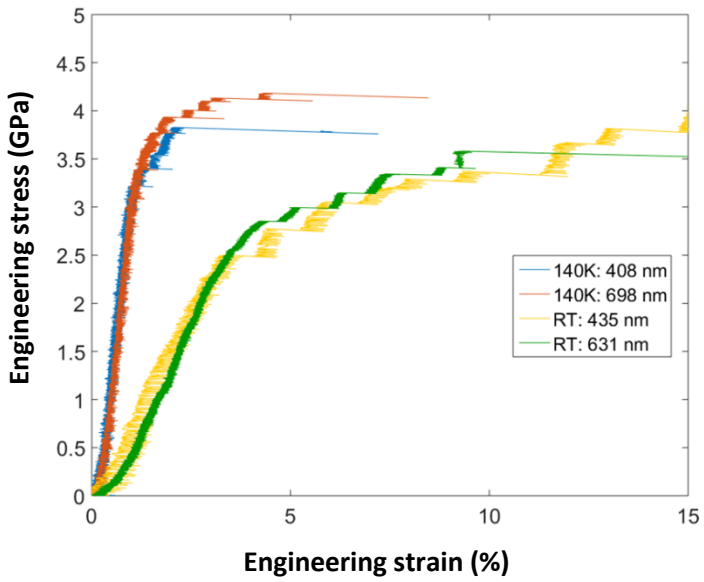

Figure 6.2. Stress–strain curves for quasi–static uniaxial pillar compression at 140K and room temperature (300K). Sample: Aged Zr–Ni–Al metallic glass

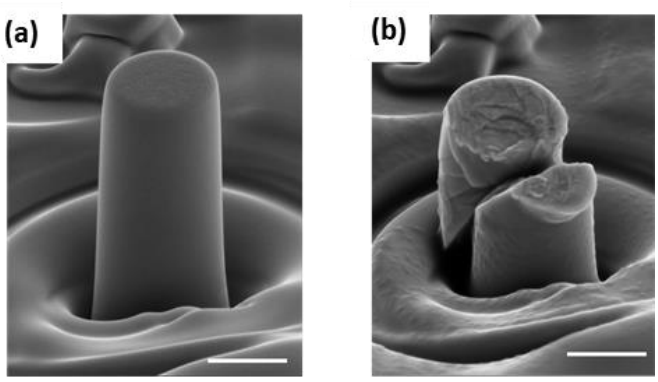

Figure 6.3. SEM images of a representative 700 nm pillar (a) before and (b) after compression at 140 K. The scale bar for both images corresponds to 500 nm. Sample: Aged Zr–Ni–Al

6.3. Discussion

The enhancement of mechanical properties at lower temperature can be explained by two factors:

1. Thermal shrinkage due to the compression of interatomic distances;
2. The difficulty for the free volume to coalesce and accommodate the stress.

6.3.1. Thermal shrinkage at cryogenic temperatures

At cryogenic temperatures, the atomic structure evolution is characterized by the overall contraction of the atomic shells. The thermodynamic mobility of atoms, such as the frequency of atomic vibration, decreases and the bonds between the atoms become stiffer. Synchrotron XRD on $Zr_{64.13}Cu_{15.75}Ni_{10.12}Al_{10}$ MG demonstrated that when the temperature decreases from 299 K to 79 K, the atomic volume decreases from 17.95 to 17.88 $Å^3$/atom, which implies that there is thermal shrinkage[135]. At low temperatures, the shifts in the scattering vector peaks suggest that the first NN shell contains of more Zr-Zr pairs and fewer Zr-Ni pairs[135]. The pair distribution functions at different temperatures reveal that there is an expansion in the first atomic shell, while the second and subsequent atomic shells experience contraction. The volume change is related to the frequency of

the lattice vibration and the coefficient of thermal expansion. It can be modelled by the Varshni expression[136]:

$$\Delta V = \Delta V_o - \frac{S}{\exp\left(\frac{\theta}{T}\right) - 1} \tag{6.1}$$

Where ΔV_o is the volume change at 0 K, θ is the effective Einstein temperature and S is a variable related to the strength of the anharmonic interactions. Between the first and second atomic shells, the difference in volume shrinkage is 11% (5.01×10^{-3} for the first peak and 5.65×10^{-3} for the second peak). The stress increment (Δp) caused by this volume change is calculated by:

$$\Delta p = K \cdot \Delta V \tag{6.2}$$

where K is the bulk modulus. With this stress increment, Bian et al. plotted the compressive strength as a function of temperature for $Zr_{64.13}Cu_{15.75}Ni_{10.12}Al_{10}$ MG, which is shown in figure 6.4[135]. The blue dots are the calculated compressive strengths, while the red stars are the experimentally measured values.

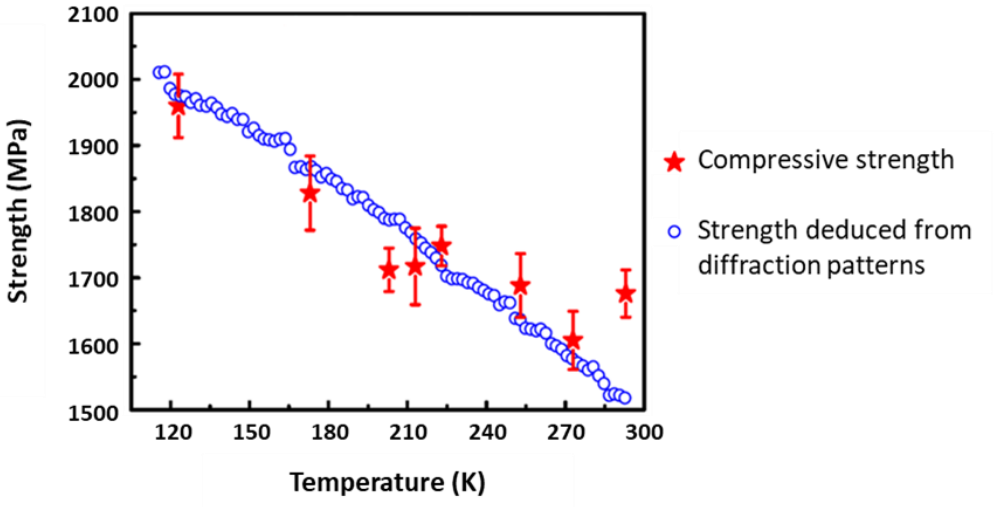

Figure 6.4. Compressive stress- strain curves vs. temperature for $Zr_{64.13}Cu_{15.75}Ni_{10.12}Al_{10}$ MG. The blue dots are the calculated compressive strengths, while the red stars are the experimentally measured values[135].

As the temperature decreases from room temperature (300 K) to 140 K, the compressive strength increases from 1518 MPa to 1950 MPa, which corresponds to a 28% increase. Compared to our data for aged Zr-Ni-Al, we observed an increase of yield strength from 2.6 GPa to 3.3 GPa, which corresponds to at 26.9% increase. This is very well matched to the increase predicted from thermal shrinkage. Thus, the enhancements in yield strengths can be attributed to the volume shrinkage and correlated with the decrease in interatomic distances between the atomic shells.

6.3.2. Difficulty for free volume to coalesce

To explain the brittle catastrophic failure mechanism observed in our cryogenic experiments, we turn to the framework of free volume. Free volume can coalesce by two ways: (1) through atomic diffusion; and (2) applied stress on the material. In the first case, the movement of free volume is a thermally activated process. At low temperatures, the annihilation rate is low for diffusion-induced free volume. As a result, atomic vibrations are minimized and free volume creation is hindered. Since cryogenic temperature results in higher density, the minimum stress required to deform a cluster of atoms (i.e. STZs) is higher. Once the stress is high enough to nucleate a shear band, it immediately results in catastrophic failure. Additionally, the formation of shear bands result in local heating[137]. When exposed to cryogenic temperatures, the local heating in the shear band can be relieved. As a result, the nucleation of the shear band requires higher applied stresses at low temperature, which leads to an increase in the yield strength[137].

6.4. Summary

Quasi–static uniaxial pillar compressions of aged Zr–Ni–Al at 140 K resulted in a substantial increase in the Young's modulus and yield strength from 90 ± 5 GPa to 326.4 ± 9.2 GPa and from

2.6 ± 0.2 GPa to 3.3 ± 0.2 GPa, respectively. The enhancement in the mechanical properties is attributed to volume shrinkage at cryogenic temperatures. A comparison between the expected volume change (from Varshni expression) and stress increment to our experimental data reveals that they are very well matched (i.e. cooling from room temperature to 140K increased the yield strength by 26.9%). Finally, our experimental stress- strain curves demonstrated that the pillars deformed by brittle catastrophic failure in the post-elastic regime. This is explained by the difficulty for free volume to coalesce at low temperatures, which results in substantially higher stress to deform a STZ.

For many practical applications, MG plasticity is very important. After aging, MGs tend to have higher strength and elastic limit, but plasticity is reduced due to shear band formation. Rejuvenation is one approach to enhance the plasticity of MGs. Studies have focused on cryogenic cycling between room temperature and liquid nitrogen temperature as a method of improving MG plasticity[138,139]. However, these results are not conclusive and more studies are needed to understand the atomistic mechanisms during cryogenic cycling.

Chapter 7. Summary and Outlook

In Chapter 3, we observed that long term aging at room temperature can improve the mechanical properties of MG due to local atomic rearrangements. This conclusion provides an important foundation for utilizing MG for any structural applications. Further studies are needed to investigate a combination of thermal annealing and RT aging to achieve a relatively stable MG with optimal mechanical property. In Chapter 4, we demonstrated that MD simulation is a powerful tool to simulate different quenching rates and produced MG with varying atomic configurations. We revealed that microstructural relaxation is correlated with an increase of fivefold bonds (higher polytetrahedral packing) and predicted higher strength and localized deformation under compression. In Chapter 5, we utilized DMA to provide a better understanding of the relaxation dynamics in MG. At low frequencies, we observed that the loss modulus increased after aging and that smaller pillars exhibited higher loss modulus than larger pillars. At high frequencies, the loss modulus peak at around 450 Hz was attributed to the activation of hydrogen mobility within the MG host matrix. This is an important finding since hydrogenation in an open air environment occurs prevalently. The formation of hydride in MG becomes an important consideration when it is being designed for practical applications. Future research in understanding the presence of hydrides in sputtered MG and finding ways to enhance the MG performance is an important research direction. In chapter 6, we studied the mechanical properties of MGs at cryogenic temperature. We observed enhancement of mechanical properties due to the volume shrinkage at cryogenic temperatures.

Oxidation of MG at room temperature is another important factor that can affect the microstructure and mechanical properties of the material. In literature, there are numerous conflicting studies on this subject. Sun et al. reported that the oxidation of $Zr_{60}Ni_{25}Al_{15}$ MG can occur between 310 ^{o}C and 410 ^{o}C[140]. Their data revealed that an amorphous layer of zirconium- aluminium- oxide

was formed at the surface of the sample. Both Zr and Al uniformly oxidized such that the Zr/Al ratio in the oxide layer was similar to that of the bulk alloy. However, Ni was absent in the oxide layer and found to enrich the amorphous alloy near the interface. Both the metallic glass and oxide remained fully amorphous. Triwikantoro et al. investigated the oxidation resistance of five different compositions of Zr-Cu-Al MG[80]. Under similar conditions as Sun et al. (i.e., 330 °C to 370 °C), they discovered that $Zr_{65}Cu_{27.5}Al_{7.5}$ oxidized the quickest while $Zr_{70}Ni_{20}Al_{10}$ was very oxidation resistant. Oxidation resistance was found to deteriorate with increasing Cu content but improved with the higher Al content. Thus, the oxidation resistance of a MG is heavily dependent on its composition. Qin et al. also studied the electrochemical corrosion and oxidation of $Zr_{60}Ni_{21}Al_{19}$ bulk MG[141]. They revealed that this amorphous alloy exhibited high electrochemical corrosion and oxidation resistance. Furthermore, they also confirmed that the addition of Cu (i.e., $Zr_{65}Ni_{10}Al_{10}Cu_{15}$) reduces the oxidation resistance of the material. Liontas et al. utilized EDS to determine the oxygen content in sputtered $Zr_{55}Ni_{29}Al_{16}$ and verified the high oxidation resistance of this material[1]. Thus, we believe that oxidation in our material is negligible. However, future work on understanding the effect of the aging phenomenon on different compositions of Zr-based MGs will need to consider the effect of oxidation on its microstructure and mechanical properties.

In this thesis, we studied the aging characteristics of sputtered MG. It is imperative to fully understand this fundamental phenomenon before sputtered metallic glass can be utilized in practical applications. Our experimental results demonstrated that aging enhanced the mechanical properties of the MG. Therefore, we would want to accelerate the aging process so that the MG reaches a relatively stable microstructural state for better performance and stability. Further investigations on varying the chemical composition and designing the annealing processes to enhance the performance and stability is needed. When choosing the MG composition, it is also important to consider the long term effects of corrosion, oxidation and hydrogenation. Since the microstructure of sputtered MGs

are at a relatively high potential energy state, the aging phenomenon is much more pronounced than in bulk MG. Certain elements such as Ni, Cu, Pt, Pd, Ti are known to be very effective catalyst for oxidation or hydrogenation processes. Therefore, a very careful choice of metallic glass composition is needed.

In our sputtered MG research, we used FIB to prepare micro- and nanopillars because it allows for the precise patterning and removal of material. However, FIB is a slow and expensive technique that is not a suitable for large-scale manufacturing. Semiconductor integrated circuit (IC) manufacturing processes is one practical approach that can implement sputtered MG for real world applications. Thus, engineering research into how we can improve the efficiency and reduce the cost of fabricating and processing sputtered metallic glass is important. In the next 5 to 10 years, many fundamental and engineering problems, such as the choice of material compositions, fabrication processes, aging, and corrosion effects, will need to be investigated so that sputtered MG can be more widely utilized in practical applications.

References

1. Liontas, R. *et al.* Substantial tensile ductility in sputtered Zr-Ni-Al nano-sized metallic glass. *Acta Mater.* **118**, 270–285 (2016).

2. Klement, W., Willens, R. H. & Duwez, P. Non-crystalline Structure in Solidified Gold-Silicon Alloys. *Nature* **187**, 869–870 (1960).

3. Ashby, M. F. & Greer, A. L. Metallic glasses as structural materials. *Scr. Mater.* **54**, 321–326 (2006).

4. Greer, A. L., Cheng, Y. Q. & Ma, E. Shear bands in metallic glasses. *Mater. Sci. Eng. R Reports* **74**, 71–132 (2013).

5. Schuh, C. A., Hufnagel, T. C. & Ramamurty, U. Mechanical behavior of amorphous alloys. *Acta Mater.* **55**, 4067–4109 (2007).

6. Telford, M. The Case for bulk metallic glass. *Mater. Today* **7**, 36–43 (2004).

7. Johnson, W. L. & Samwer, K. A Universal Criterion for Plastic Yielding of Metallic Glasses with a (T/Tg)^2/3 Temperature Dependence. *Phys. Rev. Lett.* **95**, 195501 (2005).

8. Yang, B., Liu, C. T. & Nieh, T. G. Unified equation for the strength of bulk metallic glasses. *Appl. Phys. Lett.* **88**, (2006).

9. Liu, Y. H. *et al.* Thermodynamic origins of shear band formation and the universal scaling law of metallic glass strength. *Phys. Rev. Lett.* **103**, 5–8 (2009).

10. Inoue, A., Shen, B., Koshiba, H., Kato, H. & Yavari, A. R. Cobalt-based bulk glassy alloy with ultrahigh strength and soft magnetic properties. *Nat. Mater.* **2**, 661–663 (2003).

11. Lewandowski, J. J., Wang, W. H. & Greer, A. L. Intrinsic plasticity or brittleness of metallic glasses. *Philos. Mag. Lett.* **85**, 77–87 (2005).

12. Demetriou, M. D. *et al.* A damage-tolerant glass. *Nat. Mater.* **10**, 123–128 (2011).

13. Greer, A. L., Rutherford, K. L. & Hutchings, I. M. Wear resistance of amorphous alloys and related materials. *Int. Mater. Rev.* **47**, 87–112 (2002).

14. Soinski, M., Bulica, W., Creslewicz, K. & Szczyglowski, J. Current transformer with cut core made of metallic glass ribbon. *IEEE Trans. Magn.* **24**, 1871–1872 (1988).

15. Konczos, G., Kisdi-Koszo, E. & Lovas, A. Recent Progress in the Application of Soft Magnetic Amorphous Materials: Alloys, Preparation, Devices. *Phys. Scr.* **T24**, 42–48 (1988).

16. Ramanan, V. R. V. Metallic glasses in distribution transformer applications: An update. *J. Mater. Eng.* **13**, 119–127 (1991).

17. Johnson, W. L. Bulk amorphous metal-An emerging engineering material. *Jom* **54**, 40–43 (2002).

18. Inoue, A., Shen, B. & Nishiyama, N. Development and applications of late transition metal bulk metallic glasses. *Bulk Met. Glas. An Overv.* **18**, 1–25 (2008).

19. Chu, J. P. *et al.* Thin film metallic glasses: Unique properties and potential applications. *Thin Solid Films* **520**, 5097–5122 (2012).

20. Chu, J. P., Huang, J. C., Jang, J. S. C., Wang, Y. C. & Liaw, P. K. Thin film metallic glasses: Preparations, properties, and applications. *Jom* **62**, 19–24 (2010).

21. Fukushige, T., Hata, S. & Shimokohbe, A. A MEMS conical spring actuator array. *J. Microelectromechanical Syst.* **14**, 243–253 (2005).

22. Kanik, M. *et al.* Microscale three-dimensional hemispherical shell resonators fabricated from metallic glass. *1st IEEE Int. Symp. Inert. Sensors Syst. ISISS 2014 - Proc.* (2014). doi:10.1109/ISISS.2014.6782500

23. Schroers, J., Pham, Q. & Desai, A. Thermoplastic Forming of Bulk Metallic Glass— A Technology for MEMS and Microstructure Fabrication. *J. Microelectromechanical Syst.* **16**, 240–247 (2007).

24. Barmatz, M. & Chen, H. S. Young's modulus and internal friction in metallic glass alloys from 1.5 to 300 K. *Phys. Rev. B* **9**, 4073–4083 (1974).

25. Morito, N. & Egami, T. Internal friction and reversible structural relaxation in the metallic glass Fe32Ni36Cr14P12B6. *Acta Metall.* **32**, 603–613 (1984).

26. Schroers, J., Kumar, G., Hodges, T. M., Chan, S. & Kyriakides, T. R. Bulk metallic glasses for biomedical applications. *Jom* **61**, 21–29 (2009).

27. Wang, Y. B. *et al.* Biodegradable CaMgZn bulk metallic glass for potential skeletal application. *Acta Biomater.* **7**, 3196–3208 (2011).

28. Wang, Y. B., Li, H. F., Cheng, Y., Zheng, Y. F. & Ruan, L. Q. In vitro and in vivo studies on Ti-based bulk metallic glass as potential dental implant material. *Mater. Sci. Eng. C* **33**, 3489–3497 (2013).

29. Inoue, A. Stabilization of metallic supercooled liquid and bulk amorphous alloys. *Acta Mater.* **48**, 279–306 (2000).

30. Jing, Q., Zhang, Y., Wang, D. & Li, Y. A study of the glass forming ability in ZrNiAl alloys. *Mater. Sci. Eng. A* **441**, 106–111 (2006).

31. Slater, J. C. Atomic radii in crystals. *J. Chem. Phys.* **41**, 3199–3204 (1964).

32. Zhao, S., Li, J. & Liu, B. Formation of the Ni–Zr–Al Ternary Metallic Glasses Investigated by Interatomic Potential through Molecular Dynamic Simulation. *J. Phys. Soc. Japan* **79**, 064607 (2010).

33. Korkmaz, S. & Kariper, A. Glass formation, production and superior properties of Zr-based thin film metallic glasses (TFMGs): A status review. *J. Non. Cryst. Solids* **527**, (2020).

34. Jeong, H.-W., Hata, S. & Shimokohbe, A. Microforming of three-dimensional microstructures from thin-film metallic glass. *J. Microelectromechanical Syst.* **12**, 42–52 (2003).

35. Chen, M. A brief overview of bulk metallic glasses. *NPG Asia Mater.* **3**, 82–90 (2011).

36. Gallino, I., Shah, M. B. & Busch, R. Enthalpy relaxation and its relation to the thermodynamics and crystallization of the Zr58.5Cu15.6Ni12.8Al10.3Nb2.8 bulk metallic glass-forming alloy. *Acta Mater.* **55**, 1367–1376 (2007).

37. Liu, Y. H., Fujita, T., Aji, D. P. B., Matsuura, M. & Chen, M. W. Structural origins of Johari-Goldstein relaxation in a metallic glass. *Nat. Commun.* **5**, 1–7 (2014).

38. Liu, Y. H. *et al.* Deposition of multicomponent metallic glass films by single-target magnetron sputtering. *Intermetallics* **21**, 105–114 (2012).

39. Wei, X. *et al.* Fabrication, corrosion, and mechanical properties of magnetron sputtered Cu-Zr-Al metallic glass thin film. *Materials (Basel).* **12**, (2019).

40. Hu, X., Ng, S. C., Feng, Y. P. & Li, Y. Cooling-rate dependence of the density of Pd40Ni10Cu30P20 bulk metallic glass. *Phys. Rev. B - Condens. Matter Mater. Phys.* **64**, 29–32 (2001).

41. Qiao, J. C. & Pelletier, J. M. Enthalpy relaxation in Cu46Zr45Al7Y 2 and Zr55Cu30Ni5Al10 bulk metallic glasses by differential scanning calorimetry (DSC). *Intermetallics* **19**, 9–18 (2011).

42. Suh, D. & Dauskardt, R. H. Mechanical relaxation time scales in a Zr-Ti-Ni-Cu-Be bulk metallic glass. *J. Mater. Res.* **17**, 1254–1257 (2002).

43. Wang, N., Yan, F. & Li, L. Mesoscopic examination of cyclic hardening in metallic glass. *J. Non. Cryst. Solids* **428**, 146–150 (2015).

44. Delogu, F. Effects of compression cycles on the atomic mobility in metallic glasses. *Phys. Rev. B - Condens. Matter Mater. Phys.* **79**, 1–8 (2009).

45. Deng, C. & Schuh, C. A. Atomistic mechanisms of cyclic hardening in metallic glass. *Appl. Phys. Lett.* **100**, (2012).

46. Lo, Y. C. *et al.* Structural relaxation and self-repair behavior in nano-scaled Zr-Cu metallic glass under cyclic loading: Molecular dynamics simulations. *Intermetallics* **18**, 954–960 (2010).

47. Luo, J., Dahmen, K., Liaw, P. K. & Shi, Y. Low-cycle fatigue of metallic glass nanowires. *Acta Mater.* **87**, 225–232 (2015).

48. Zhan, Z. J., Liu, Q. Y., Zheng, R. G., Wang, W. K. & Liu, J. Equation of state of Zr41Ti14Cu12.5 Ni10Be22.5 bulk metallic glass. *J. Harbin Inst. Technol. (New Ser.* **14**, 432–435 (2007).

49. Li, G. *et al.* Structural relaxation of Zr41Ti14Cu 12.5Ni10Be22.5 bulk metallic glass under high pressure. *Sci. China, Ser. G Phys. Astron.* **46**, 468 (2003).

50. Wang, W. H., Wang, R. J., Zhao, D. Q., Pan, M. X. & Yao, Y. S. Microstructural transformation in a Zr41Ti14Cu12.5Ni10Be 22.5 bulk metallic glass under high pressure.

Phys. Rev. B - Condens. Matter Mater. Phys. **62**, 11292–11295 (2000).

51. Yu, P., Bai, H. Y., Zhao, J. G., Jin, C. Q. & Wang, W. H. Pressure effects on mechanical properties of bulk metallic glass. *Appl. Phys. Lett.* **90**, 2–5 (2007).

52. Tong, Y. *et al.* Structural rejuvenation in bulk metallic glasses. *Acta Mater.* **86**, 240–246 (2015).

53. Flores, K. M., Kanungo, B. P., Glade, S. C. & Asoka-Kumar, P. Characterization of plasticity-induced structural changes in a Zr-based bulk metallic glass using positron annihilation spectroscopy. *J. Non. Cryst. Solids* **353**, 1201–1207 (2007).

54. Meng, F., Tsuchiya, K., Seiichiro, I. & Yokoyama, Y. Reversible transition of deformation mode by structural rejuvenation and relaxation in bulk metallic glass. *Appl. Phys. Lett.* **101**, 2012–2015 (2012).

55. Mayr, S. G. Impact of ion irradiation on the thermal, structural, and mechanical properties of metallic glasses. *Phys. Rev. B - Condens. Matter Mater. Phys.* **71**, 1–7 (2005).

56. Xiao, Q., Huang, L. & Shi, Y. Suppression of shear banding in amorphous ZrCuAl nanopillars by irradiation. *J. Appl. Phys.* **113**, 83514 (2013).

57. Avchaciov, K. A., Ritter, Y., Djurabekova, F., Nordlund, K. & Albe, K. Controlled softening of Cu64Zr36 metallic glass by ion irradiation. *Appl. Phys. Lett.* **102**, (2013).

58. Avchaciov, K. A., Ritter, Y., Djurabekova, F., Nordlund, K. & Albe, K. Effect of ion irradiation on structural properties of Cu64Zr36 metallic glass. *Nucl. Instruments Methods Phys. Res. Sect. B Beam Interact. with Mater. Atoms* **341**, 22–26 (2014).

59. Baumer, R. E. & Demkowicz, M. J. Prediction of spontaneous plastic deformation of irradiated metallic glasses due to thermal spike-induced plasticity. *Mater. Res. Lett.* **2**, 221–226

(2014).

60. Baumer, R. E. & Demkowicz, M. J. Radiation response of amorphous metal alloys: Subcascades, thermal spikes and super-quenched zones. *Acta Mater.* **83**, 419–430 (2015).

61. Baumer, R. E. & Demkowicz, M. J. A 'figure of merit' for susceptibility of irradiated amorphous metal alloys to thermal spike-induced plasticity. *Acta Mater.* **102**, 251–262 (2016).

62. Yamamoto, T., Takahashi, T., Kimura, H. & Inoue, A. Effect of ball-milling and shot-peening on Zr55Al10Ni5Cu30 alloys. *J. Alloys Compd.* **430**, 97–101 (2007).

63. Fornell, J. *et al.* Effects of shot peening on the nanoindentation response of Cu 47.5Zr47.5Al5 metallic glass. *J. Alloys Compd.* **586**, S36–S40 (2014).

64. Concustell, A., Méar, F. O., Suriñach, S., Baró, M. D. & Greer, A. L. Structural relaxation and rejuvenation in a metallic glass induced by shot-peening. *Philos. Mag. Lett.* **89**, 831–840 (2009).

65. Méar, F. O., Lenk, B., Zhang, Y. & Greer, A. L. Structural relaxation in a heavily cold-worked metallic glass. *Scr. Mater.* **59**, 1243–1246 (2008).

66. Raghavan, R., Ayer, R., Jin, H. W., Marzinsky, C. N. & Ramamurty, U. Effect of shot peening on the fatigue life of a Zr-based bulk metallic glass. *Scr. Mater.* **59**, 167–170 (2008).

67. Zhang, Y., Wang, W. H. & Greer, A. L. Making metallic glasses plastic by control of residual stress. *Nat. Mater.* **5**, 857–860 (2006).

68. Nishi, Y. & Harano, H. Effects of peening on magnetic-flux density in a metallic glass. *J. Appl. Phys.* **63**, 1141–1143 (1988).

69. Nishi, Y., Harano, H., Fukunaga, T. & Suzuki, K. Effect of peening on structure and volume in a liquid-quenched Pd0.835Si0.165 glass. *Phys. Rev. B* **37**, 2855–2860 (1988).

70. Ketov, S. V. *et al.* Rejuvenation of metallic glasses by non-affine thermal strain. *Nature* **524**, 200–203 (2015).

71. Saida, J., Yamada, R. & Wakeda, M. Recovery of less relaxed state in Zr-Al-Ni-Cu bulk metallic glass annealed above glass transition temperature. *Appl. Phys. Lett.* **103**, 8–12 (2013).

72. Wakeda, M., Saida, J., Li, J. & Ogata, S. Controlled rejuvenation of amorphous metals with thermal processing. *Sci. Rep.* **5**, 1–8 (2015).

73. Shan, Z. W. *et al.* Plastic flow and failure resistance of metallic glass: Insight from in situ compression of nanopillars. *Phys. Rev. B* **77**, 155419 (2008).

74. Volkert, C. A., Donohue, A. & Spaepen, F. Effect of sample size on deformation in amorphous metals. *J. Appl. Phys.* **103**, (2008).

75. Kuzmin, O. V., Pei, Y. T., Chen, C. Q. & De Hosson, J. T. M. Intrinsic and extrinsic size effects in the deformation of metallic glass nanopillars. *Acta Mater.* **60**, 889–898 (2012).

76. Jang, D. & Greer, J. R. Transition from a strong-yet-brittle to a stronger-and-ductile state by size reduction of metallic glasses. *Nat. Mater.* (2010). doi:10.1038/nmat2622

77. Guo, H. *et al.* Tensile ductility and necking of metallic glass. *Nat. Mater.* **6**, 735–739 (2007).

78. Chen, C. Q. *et al.* Intrinsic size effects in the mechanical response of taper-free nanopillars of metallic glass. *Phys. Rev. B - Condens. Matter Mater. Phys.* **83**, 4–7 (2011).

79. Jang, D., Gross, C. T. & Greer, J. R. Effects of size on the strength and deformation mechanism in Zr-based metallic glasses. *Int. J. Plast.* **27**, 858–867 (2011).

80. Triwikantoro, Toma, D., Meuris, M. & Köster, U. Oxidation of Zr-based metallic glasses in air. *J. Non. Cryst. Solids* **250–252**, 719–723 (1999).

81. Jing, Q., Zhang, B., Zhang, J., Ma, M. & Liu, R. Electrochemical corrosion and oxidation resistances of Zr60Ni21Al19 bulk amorphous alloys. *Sci. China Physics, Mech. Astron.* **53**, 2223–2226 (2010).

82. Li, Y. H. *et al.* Formation and mechanical properties of Zr–Ni–Al glassy alloys with high glass-forming ability. *Intermetallics* **18**, 1851–1855 (2010).

83. Sato, S. *et al.* Effect of Al on Local Structures of Z-Ni and Zr-Cu Metallic Glasses. *Mater. Trans.* **46**, 2893–2897 (2005).

84. Agilent Technologies. High and Ultra-High Vacuum for Science Research. *Semin. High Ultra-High Vac. Sci. Res.* 1–132 (2011).

85. Mayer, J., Giannuzzi, L. A., Kamino, T. & Michael, J. TEM sample preparation and FIB-induced damage. *MRS Bull.* **32**, 400–407 (2007).

86. Newbury, D. E. & Ritchie, N. W. M. Is scanning electron microscopy/energy dispersive X-ray spectrometry (SEM/EDS) quantitative? *Scanning* **35**, 141–168 (2013).

87. Marimuthu, K. P., Lee, K., Han, J., Rickhey, F. & Lee, H. Nanoindentation of zirconium based bulk metallic glass and its nanomechanical properties. *J. Mater. Res. Technol.* **9**, 104–114 (2020).

88. Wang, W. H. Dynamic relaxations and relaxation-property relationships in metallic glasses. *Prog. Mater. Sci.* **106**, 100561 (2019).

89. Tong, X. *et al.* Structural evolution and strength change of a metallic glass at different temperatures. *Sci. Rep.* **6**, 1–12 (2016).

90. Liu, C., Pineda, E. & Crespo, D. *Mechanical relaxation of metallic glasses: An overview of experimental*

data and theoretical models. *Metals* **5**, (2015).

91. Wang, J. G. *et al.* Hardening of shear band in metallic glass. *Sci. Rep.* **7**, 2–11 (2017).

92. Yu, H. Bin, Wang, W. H. & Samwer, K. The β relaxation in metallic glasses: An overview. *Mater. Today* **16**, 183–191 (2013).

93. Chen, D. Z. *et al.* Nanometallic glasses: Size reduction brings ductility, surface state drives its extent. *Nano Lett.* **13**, 4462–4468 (2013).

94. Khonik, V. A. Understanding of the structural relaxation of metallic glasses within the framework of the interstitialcy theory. *Metals (Basel).* **5**, 504–529 (2015).

95. Khonik, V. A., Kitagawa, K. & Morii, H. On the determination of the crystallization activation energy of metallic glasses. *J. Appl. Phys.* **87**, 8440–8443 (2000).

96. Adachi, N., Todaka, Y., Yokoyama, Y. & Umemoto, M. Improving the mechanical properties of Zr-based bulk metallic glass by controlling the activation energy for β -relaxation through plastic deformation. *Appl. Phys. Lett.* **105**, 4–9 (2014).

97. Evenson, Z. *et al.* β relaxation and low-temperature aging in a Au-based bulk metallic glass: From elastic properties to atomic-scale structure. *Phys. Rev. B - Condens. Matter Mater. Phys.* **89**, 1–14 (2014).

98. Gallino, I. *et al.* Activation energy spectrum for relaxation and polyamorphism in an ultra-viscous metallic glass former. 1–28 (2017).

99. Yavari, A. R. *et al.* Quenched-in free volume Vf, deformation-induced free volume, the glass transition Tg and thermal expansion in glassy ZrNbCuNiAl measured by time-resolved diffraction in transmission. *Mater. Res. Soc. Symp. - Proc.* **806**, 203–208 (2003).

100. Weaire, D., Ashby, M. F., Logan, J. & Weins, M. J. On the use of pair potentials to calculate the properties of amorphous metals. *Acta Metall.* **19**, 779–788 (1971).

101. Li, F. *et al.* Atomic scale calculation of the free volume in Zr2Ni metallic glass. *Intermetallics* **17**, 98–103 (2009).

102. Kim, Y. C., Kim, W. T. & Kim, D. H. A development of Ti-based bulk metallic glass. *Mater. Sci. Eng. A* **375–377**, 127–135 (2004).

103. Plimpton, S. Fast Parallel Algorithms for Short-Range Molecular Dynamics. *Journal of Computational Physics* **117**, 1–19 (1995).

104. Howard Sheng, School of Physics, Astronomy & Computational Sciences, George Mason University, Fairfax, VA 22030 (Potential provided through private communications)Howard Sheng, School of Physics, Astronomy & Computational Sciences, George Mason University.

105. Stukowski, A. Visualization and analysis of atomistic simulation data with OVITO–the Open Visualization Tool. *Modelling and Simulation in Materials Science and Engineering* **18**, 015012 (2009).

106. Rycroft, C. H. VORO++: A three-dimensional Voronoi cell library in C++. *Chaos An Interdiscip. J. Nonlinear Sci.* **19**, 041111 (2009).

107. Sun, Y. J. *et al.* Zr-Cu-Ni-Al bulk metallic glasses with superhigh glass-forming ability. *Acta Mater.* **57**, 1290–1299 (2009).

108. Louzguine-Luzgin, D. V *et al.* An atomistic study of the structural changes in a Zr–Cu–Ni–Al glass-forming liquid on vitrification monitored in-situ by X-ray diffraction and molecular dynamics simulation. *Intermetallics* **122**, 106795 (2020).

109. Hirata, A. *et al.* Direct observation of local atomic order in a metallic glass. *Nat. Mater.* **10**, 28–

33 (2011).

110. Xi, X. K., Li, L. L., Zhang, B., Wang, W. H. & Wu, Y. Correlation of Atomic Cluster Symmetry and Glass-Forming Ability of Metallic Glass. *Phys. Rev. Lett.* **99**, 095501 (2007).

111. Mattern, N. *et al.* Short-range order of Cu–Zr metallic glasses. *J. Alloys Compd.* **485**, 163–169 (2009).

112. Tang, C. & Wong, C. H. A molecular dynamics simulation study of solid-like and liquid-like networks in Zr46Cu46Al8 metallic glass. *J. Non. Cryst. Solids* **422**, 39–45 (2015).

113. Frank, F. C. & Kasper, J. S. Complex alloy structures regarded as sphere packings. I. Definitions and basic principles. *Acta Crystallogr.* **11**, 184–190 (1958).

114. Ding, J., Cheng, Y.-Q. & Ma, E. Full icosahedra dominate local order in Cu64Zr34 metallic glass and supercooled liquid. *Acta Mater.* **69**, 343–354 (2014).

115. Cheng, Y. Q., Cao, A. J. & Ma, E. Correlation between the elastic modulus and the intrinsic plastic behavior of metallic glasses: The roles of atomic configuration and alloy composition. *Acta Mater.* **57**, 3253–3267 (2009).

116. Duan, G. *et al.* Strong configurational dependence of elastic properties for a binary model metallic glass. *Appl. Phys. Lett.* **89**, 2012–2015 (2006).

117. Mayr, S. G. Relaxation kinetics and mechanical stability of metallic glasses and supercooled melts. *Phys. Rev. B* **79**, 060201 (2009).

118. Hazelton, L. E. & Johnson, W. L. Distribution of activation energies in amorphous Zr2PdHx. *J. Non. Cryst. Solids* **61–62**, 667–672 (1984).

119. Christensen, M. *et al.* H in -Zr and in zirconium hydrides: Solubility, effect on dimensional

changes, and the role of defects. *J. Phys. Condens. Matter* **27**, (2015).

120. Ghosh, S., Hariharan, S. & Tiwari, A. K. Water Adsorption and Dissociation on Copper/Nickel Bimetallic Surface Alloys: Effect of Surface Temperature on Reactivity. *J. Phys. Chem. C* **121**, 16351–16365 (2017).

121. Seenivasan, H., Jackson, B. & Tiwari, A. K. Water dissociation on Ni(100), Ni(110), and Ni(111) surfaces: Reaction path approach to mode selectivity. *J. Chem. Phys.* **146**, (2017).

122. Paillier, J., Rongeat, C., Gutfleisch, O. & Gebert, A. Hydrogen and Zr-based metallic glasses: Gas/solid absorption process and structure evolution. *J. Alloys Compd.* **509**, 1636–1643 (2011).

123. Maeland, A. J., Tanner, L. E. & Libowitz, G. G. Hydrides of Metallic Glass Alloys. *J. less-common Met.* **74**, 279–285 (1980).

124. Ismail, N., Uhlemann, M., Gebert, A., Eckert, J. & Schultz, L. The electrochemical hydrogen sorption behaviour of Zr-Cu-Al-Ni metallic glasses. *Mater. Trans.* **43**, 1133–1137 (2002).

125. Berry, B. S. & Pritchet, W. C. Host and hydrogen diffusion in an NiZr metallic glass. *Mater. Sci. Eng.* **97**, 419–425 (1988).

126. Peng, S. X. *et al.* Anomalous nonlinear damping in metallic glasses: Signature of elasticity breakdown. *J. Chem. Phys.* **150**, (2019).

127. Leich, D. A. & Tombrello, T. A. A technique for measuring hydrogen concentration versus depth in solid samples. *Nucl. Inst. Methods Phys. Res. B* **108**, 67–71 (1973).

128. Fulin Xiong *et al.* Hydrogen depth profiling in solids: A comparison of several resonant nuclear reaction techniques. *Nucl. Inst. Methods Phys. Res. B* **27**, 432–441 (1987).

129. Pan, D., Guo, H., Zhang, W., Inoue, A. & Chen, M. W. Temperature-induced anomalous brittle-to-ductile transition of bulk metallic glasses. *Appl. Phys. Lett.* **99**, 5–9 (2011).

130. Jiang, F. *et al.* Shear transformation zone volume determining ductile-brittle transition of bulk metallic glasses. *Acta Mater.* **59**, 2057–2068 (2011).

131. Klaumünzer, D., Maa, R., Torre, F. H. D. & Löffler, J. F. Temperature-dependent shear band dynamics in a Zr-based bulk metallic glass. *Appl. Phys. Lett.* **96**, 22–25 (2010).

132. Yoon, K. S., Lee, M., Fleury, E. & Lee, J. C. Cryogenic temperature plasticity of a bulk amorphous alloy. *Acta Mater.* **58**, 5295–5304 (2010).

133. Qiao, J. W., Jia, H. L., Zhang, Y., Liaw, P. K. & Li, L. F. Multi-step shear banding for bulk metallic glasses at ambient and cryogenic temperatures. *Mater. Chem. Phys.* **136**, 75–79 (2012).

134. Li, H., Fan, C., Tao, K., Choo, H. & Liaw, P. K. Compressive behavior of a Zr-based metallic glass at cryogenic temperatures. *Adv. Mater.* **18**, 752–754 (2006).

135. Bian, X. L. *et al.* Atomic origin for rejuvenation of a Zr-based metallic glass at cryogenic temperature. *J. Alloys Compd.* **718**, 254–259 (2017).

136. Varshni, Y. P. Temperature dependence of the elastic constants. *Phys. Rev. B* **2**, 3952–3958 (1970).

137. Leamy, H. J., Wang, T. T. & Chen, H. S. Plastic flow and fracture of metallic glass. *Metall. Trans.* **3**, 699–708 (1972).

138. Grell, D., Dabrock, F. & Kerscher, E. Cyclic cryogenic pretreatments influencing the mechanical properties of a bulk glassy Zr-based alloy. *Fatigue Fract. Eng. Mater. Struct.* **41**, 1330–1343 (2018).

139. Lei, T. J. *et al.* Microscopic characterization of structural relaxation and cryogenic rejuvenation in metallic glasses. *Acta Mater.* **164**, 165–170 (2019).

140. Sun, X., Schneider, S., Geyer, U., Johnson, W. L. & Nicolet, M. A. Oxidation and crystallization of an amorphous Zr60Al15Ni25 alloy. *J. Mater. Res.* **11**, 2738–2743 (1996).

141. Jing, Q., Zhang, B., Zhang, J., Ma, M. & Liu, R. Electrochemical corrosion and oxidation resistances of Zr 60Ni21Al19 bulk amorphous alloys. *Sci. China Physics, Mech. Astron.* **53**, 2223–2226 (2010).